Numerical Simulation of the Long-term Balance of Salinity in the Persian Gulf

By

Xiaohui Yan

A thesis submitted under supervision of
Dr. Majid Mohammadian
in partial fulfillment of the requirements for the degree of

Masters of Applied Science in Civil Engineering

Department of Civil Engineering
University of Ottawa
Ottawa, Canada
April 2015

The M.A.S.c in Civil Engineering is a joint program
with Carleton University administrated
by Ottawa-Carleton Institute for Civil Engineering

Abstract

The salinity distribution in an inverse estuary (where the sea water is concentrated by the estuary water) possesses its own uniqueness due to excessive net freshwater loss and restricted circulation. The study of long-term balance of salinity can contribute to a better understanding of the mixing and transport properties in such a distinct type of water body (i.e., inverse estuary water), and can provide valuable information for sound water management and environmental assessment. The Persian Gulf is chosen to be the study region, as it is a typical large-scale inverse estuary with severe shortages of freshwater resources and has been of significant research interest during the past several decades.

For basin-wide examinations of a large-scale inverse estuary, analytical solutions are typically unavailable and field measurements are expensive, so numerical modeling as well as validation with available data is the main focus in this thesis. Firstly, the salinity distribution in the Persian Gulf is simulated with 8 different schemes, and the obtained results are compared with the World Ocean Atlas 2013 (WOA13) data. The comparisons can validate the utilization of the numerical model in predicting the salinity distribution in a large-scale inverse estuary. Given that results are affected by the choice of the numerical scheme, a performance analysis of candidate schemes is performed. The most appropriate scheme for the Persian Gulf is figured out in this stage. Secondly, the validated scheme is used for the prediction with respect to the long-term salinity response of the Persian Gulf to the climate change and anthropogenic activities. The results show that without mitigation measures taken, the salinity in the Persian Gulf will continually increase with time.

The long-term and basin-wide simulations that will be presented in this thesis are expected to be more useful than previous studies (which were generally limited in time from hours to a few months) in terms of inspecting long-term characteristics. The performance of various numerical schemes has been assessed for the first time through a practical case study, which can contribute to a better understanding of the applications and characteristics of these schemes. Besides, the long-term salinity variations in the Persian Gulf are predicted for the next half-century, and this is the first numerical prediction of the long-term salinity response of the Persian Gulf to climate changes and anthropogenic activities.

Acknowledgements

Deepest appreciation goes to my supervisor Dr. Majid Mohammadian, without whom I would not possibly have embarked upon this study. Your all-sided supervision and unwavering support means a lot to me.

Thanks also to Dr. Nistor, Dr. Seidou, and Dr. Dragomirescu, whose suggestions, intelligence and resourcefulness make a real difference in this project.

Besides, I would also like to thank Dr. Hazim Mohammeed Qiblawey, a professor at Qatar University, who has helped me a great deal in during the course of my research.

Finally, I would like to thank my family and friends for providing support and friendship that I needed.

Table of Contents

List of Figures

List of Tables

List of Symbols

a_C = acceleration (m^2/s);

a_j = coefficients;

$A(x)$ = cross-sectional area (m^2);

c = constant speed of a flow (m/s);

C_{Drag} = drag coefficient;

D = coefficient of diffusion;

D / Dt = total derivative;

e = the internal energy per unit mass (J/kg);

E = evaporation (mm/d);

f = body force per unit mass ($N/(m^2.kg)$);

F = forcing and dissipation;

j = spatial index;

J_d = diffusive mass flux;

h_0 = water depth (m);

k = wave number;

k_t = thermal conductivity (W/(m.K))

$\hat{k}$ = unit vector in the vertical direction;

K_H = effective dispersion coefficient;

L = Location;

L_{a^*} = weighted value for the convergence length over the length (m);

$L_{e,0}$ = tidal excursion length (m);

L_s = length of salt intrusion (m);

LT = Latitude (°);

n = temporal index;

N = order;

$N_{R,0}$ = estuarine Richardson number;

p = pressure (N/m^2);

P = precipitation (mm/d);

P_1, P_2 = polynomial;

$\dot{q}$ = rate of volumetric heat addition per unit mass (Btu/lb);

Q = discharge (m^3/s);

r_{dist} = distance from the axis (m);

R = runoff (mm);

R_{moving} = ocean surface;

R_0 = surface in the resting fluid;

S = salinity (psu);

$S_{1,2,3\cdots}$ = scheme;

t = time (s);

T = period (s);

u_0 = maximum tidal velocity (m/s);

$u, v, \dot{r}$ = velocity (m/s);

$\mathbf{U}$ = vertically integrated horizontal velocity (m/s);

U_{wind} = wind velocity (m/s);

$v_{\tan}$ = tangential speed (m/s);

$V^2 / 2$ = kinetic energy per unit mass (J/kg);

W = WOA13;

z = vertical coordinate;

Δt = time step (s);

ΔS_C = distance (m);

η = surface elevation (m);

φ = latitude (°);

ϕ = geo-potential (m^2/s^2);

∇ = gradient operator;

λ = decay rate;

Ω = Earth's rotation (rps);

ω_{ang} = angular speed (rps);

ρ = density (g/cm^3);

τ = stress (N/m^2);

τ_{wind} = wind stress (N/m^2);;

θ = potential temperature (°C);

K = secant bulk modulus (pa).

Chapter 1 Introduction

Abstract This chapter will introduce the background knowledge of salinity in water bodies, definition and classification of estuaries, and salinity distribution in estuaries. In fact, these are also the keywords of this thesis. The primary objectives of the present study will be described, which can serve as a general explanation of the current research. Furthermore, in Section 1.4, the novelty and significance of the current study will be discussed. Finally, the outline of this thesis will be presented.

1.1 Background and Fundamentals of Salinity

Salinity is the saltiness or the quantity of dissolved salt content of a body of water, and it is a factor that can be used for understanding the environmental conditions and organisms in the water. The main components of the salt in the ocean are Sodium (Na) and Chlorine (Cl), while other major elements are Magnesium (Mg), Calcium (Ca), Potassium (K) and Sulfate (SO_4), together they account for 99.4 % of the dissolved salt (USEPA, 2015, Figure 1-1; CATDS, 2015, Figure 1-2).

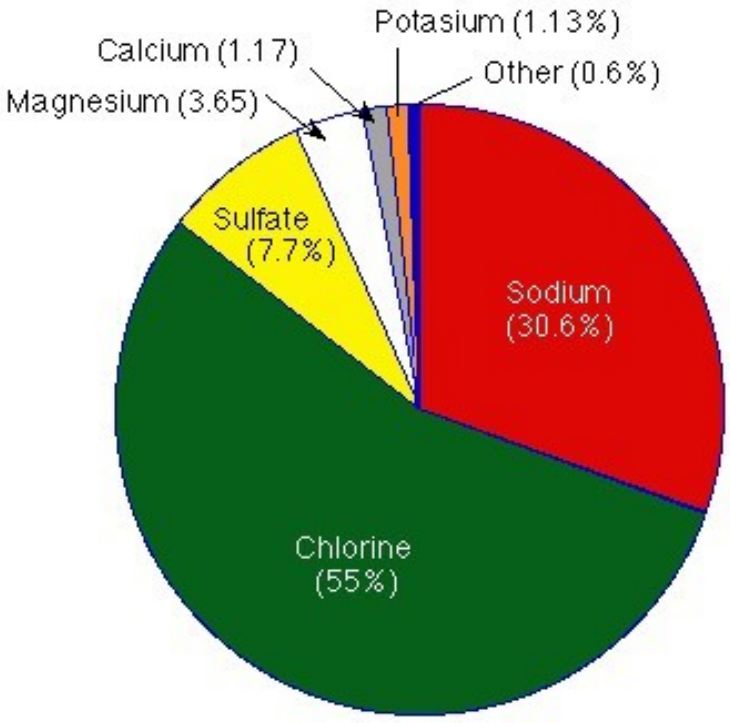

Figure 1-1. Salts in Seawater (US EPA, 2015)

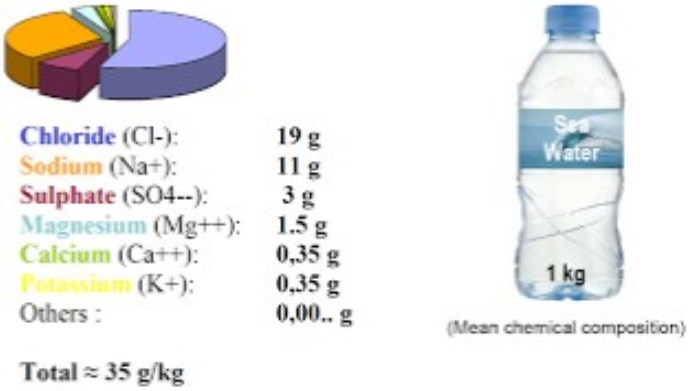

Figure 1-2. Mean Chemical Composition of a Sample of Seawater (CATDS, 2015)

Salinity is generally measured in Practical Salinity Units (psu), which is a unit based on the properties of seawater conductivity and is equivalent to unit per thousand or to g/kg; for example, 35 psu = 1 g dissolved salt / 1 kg sea water = 35 ppt = 3.5% = 35,000 ppm . The ocean typically has a salinity of about 35 psu (WOA, 2009, Figure 1-3); the salinity in estuaries is typically lower; the salinity in rivers and lakes varies from less than 0.01 psu to a few psu; and the salinity in the Dead Sea is more than 40 psu. Different classifications of water based on salinity are summarized in Table 1-1 (TET, 2015).

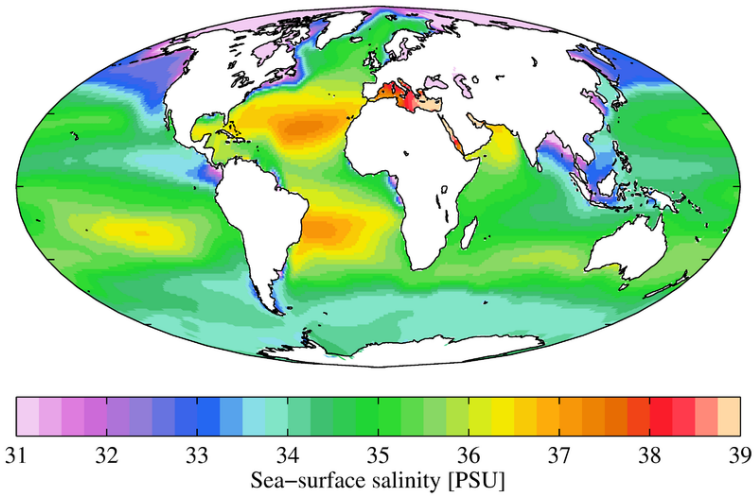

Figure 1-3. Annual Mean Sea Surface Salinity for the World's Oceans (WOA, 2009)

Table 1-1. Classifications of Water Based on Salinity (TET, 2015)

Category	Salinity
Fresh water	less than 0.1 psu
Mildly brackish water	from 1 to 5 psu
Moderately brackish water	from 5 to 15 psu
Heavily brackish water	from 15 to 35 psu
Seawater	from 30 to 50 psu
Briny water	more than 50 psu

Salinity in water can have significant impacts in various ways. The quality of water for drinking and irrigation can deteriorate because of salinization of previously fresh rivers. Salinity changes can lead to density changes in oceans, which can influence the world's ocean circulation. The salt can also destroy some natural habitats, which can significantly impact natural vegetation and terrestrial biodiversity. Agricultural production can be reduced if the salinity of the water in the soil is too high, since high salinity in soil water will pull water out from the plant roots. Salinity in water can also influence the ecological health of streams (QG, 2015).

1.2 Estuaries and Salinity Distribution

An estuary is a semi-enclosed body of water connected to the open ocean that receives fresh water from rivers, runoff and seepage (Elliott & McLusky, 2002). Estuaries are closely linked to humans, as they are highly populated, and the resources in these areas are being increasingly exploited; they also play a critical role in a wide range of oceanic processes such as oceanic biogeochemical cycling (Howarth *et al.*, 2011). An estuary can be categorized either as classical or inverse. A classical estuary, as defined by Pritchard (1952), is an estuary in which the seawater is measurably diluted by freshwater. An inverse estuary, in contrast, is one in which the seawater is concentrated primarily because of net freshwater loss.

Inverse estuaries are significantly influenced by anthropogenic activities and climate because they are generally shallow marginal seas and have restricted circulation. These estuaries are predominately located in regions with hot, arid, or semi-arid climates, where evaporation considerably surpasses the freshwater supply. A few inverse estuaries can also be found at high latitudes, where freshwater loss is mainly achieved by sea-ice formation (Nunes-Vaz, 2012). Examples of large-scale inverse estuaries include the Mediterranean Sea, the Red Sea, the Persian Gulf, the Gulf of California, and the Adriatic Sea.

In a classical estuary, the inflow from the adjacent open ocean is typically of higher salinity than the outflow, so that the inflow is beneath the seaward flow. In an inverse estuary, it is just the opposite: the landward inflow is above the outflow, since the outflow is hyper-saline. In addition to the circulation pattern, the salinity distribution in an inverse estuary can also have a great number of other impacts: it can influence the structure of the local food web for aquatic species like the Flagfin Mojarra (Gning *et al.*, 2010), can control the flushing time of the waters in inverse estuaries (Kampf & Ellis, 2014), and so on.

The salinity distribution in estuaries has been a topic of significant research interest during the past decade. It has been investigated by observational and analytical methods in earlier works and primarily by numerical methods in recent works. A limited number of observational works have involved field observations (Liu & Bao, 2011) and remote sensing techniques (Wang & Xu, 2008). The well-known disadvantage of field observations is that they are extremely time-consuming and expensive, and remote sensing techniques can only provide satisfactory data at the surface. Analytical analysis has mainly involved the prediction of salinity distribution in prismatic and convergent estuaries (Kuijper & Van Rijn, 2011) and analytical solutions for salinity distribution in a large estuary with complex topography and multiple channels (Zhang *et al.*, 2011). It is commonly accepted that despite their usefulness in predicting estuarine flows, analytical models are not able to adequately capture some observed flow properties, especially in large-scale estuaries with realistic topography and complex climate conditions. Hence, the numerical modeling method will be the central focus in this thesis.

Numerical simulations of salinity distribution in estuaries have been widely performed, particularly since the recent advances in computational techniques and resources. The salinity

in the Mediterranean Sea was studied by Fernández *et al.* (2005) in a 1/8° horizontal resolution numerical simulation using the Dietrich Center for Air-Sea Technology (DieCAST), a primitive equation, z-level vertical coordinate, rigid-lid, finite difference ocean model. Liu *et al.* (2007) developed a branched, laterally integrated, 2D, real-time model to study the effect of channel connection on the flow and salinity distribution of the Danshuei River estuary. The Hybrid Coordinate Ocean Model (HYCOM) was employed by Chang *et al.* (2008) to study the outflow of warm, salty, dense water from the Red Sea into the western Gulf of Aden. Georgiou *et al.* (2009) conducted a set of numerical experiments using the finite volume coastal ocean model FVCOM, a prognostic, unstructured-grid, finite-volume, free-surface, 3D primitive equation coastal ocean circulation model, to study the impact of multiple freshwater diversions on the salinity distribution in the Pontchartrain estuary (which is in the United States). The Adriatic Sea surface salinity was checked by the Regional Ocean Modeling System (ROMS), which is a finite difference, free surface model with curvilinear grids (Janekovic, 2010).

1.3 Objectives of the Study

The previous section briefly summarized some important previous studies of salinity in inverse estuaries through numerical modeling. However, the majority of the previous simulations were limited in time from hours to a few months, which might not be long enough to validate the employed models and inspections for long-term characteristics. Additionally, to the authors' knowledge, detailed assessments of the performance of various relevant approaches or algorithms have not been reported in the literature, while the selection of appropriate schemes can have a great influence on the simulated results. Besides, the long-term balance of salinity in the Persian Gulf has not been numerically inspected. The Persian Gulf is chosen to be the study domain mainly for the following three reasons: it is a typical inverse estuary undergoing serious salinity problems; the shortage of freshwater in this area requires better understandings of the Gulf water; and this is a region with abundant natural resources (e.g., oil and natural gases), which means that this area is especially important.

Based on these considerations, the main objectives of the current project are:

- To examine the salinity distribution in a large-scale inverse estuary by using a general circulation model. The Persian Gulf (Figure 1-4) is chosen to be the study domain, since

it is a typical large-scale inverse estuary and has been of significant research interest during the past several decades.

- To conduct long-term and basin-wide simulations of the salinity distribution in the Persian Gulf by utilizing 8 different combinations of equations of state, methods for dealing with the free surface in the momentum equations and advection algorithms for the tracer equations.

- To compare the simulated results with the available data. The comparisons are used to validate the numerical model and provide insight into the performance of the numerical schemes.

- To determine the most appropriate scheme for this case (the salinity distribution in the Persian Gulf) and employ it to predict the long-term salinity response of the Persian Gulf to the climate change and anthropogenic activities.

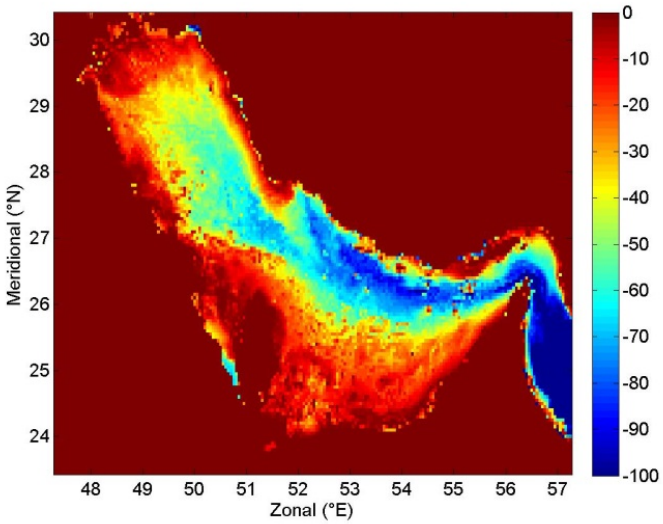

Figure 1-4. Study Domain (the Persian Gulf) and its Bathymetry

1.4 Significance and Novelty of the Study

Basin-wide simulations of salinity in the Persian Gulf are performed for the period 2005-2060, and these long-term and basin-wide simulations are expected to be more capable than previous studies in validating the models and inspecting long-term characteristics (because previous studies were limited in time from hours to a few months).

The performance of various numerical schemes is assessed for the first time for this case (the salinity distribution in the Persian Gulf), which can contribute to a better understanding of the applications and characteristics of these schemes.

Different combinations of equations of state, methods for dealing with the free surface in the momentum equations, and advection algorithms for tracer equations are examined. This is the first time that the interactional effects of these approaches or algorithms are considered.

The long-term variations of salinity in the Persian Gulf are predicted for the next half-century, and this is the first numerical prediction of the long-term (both temporal and spatial) salinity response of the Persian Gulf to the climate change and anthropogenic activities.

1.5 Thesis Outline

This thesis is organized as follows:

- The current chapter is an introduction to the present project.
- The next chapter provides an overview of the study region (the Persian Gulf) with respect to the geography, temperature, wind, river discharge, evaporation, desalination capacities, heat budget, and hydrodynamics.
- Chapter 3 reviews the relevant literature, including the theoretical background, and a review of some previous studies.
- The methodology is described in Chapter 4, including summaries of the governing equations, the discretization methods, the methods for preparing the data, boundary conditions, and the model setup.
- In Chapter 5, the study of numerical modeling of salinity distribution in a large-scale inverse estuary is presented.
- Chapter 6 describes the study about the long-term salinity response of the Persian Gulf to the climate change and anthropogenic activities
- Finally, in Chapter 7, the present study is summarized and some conclusions are drawn.

Chapter 2 Description of the Study Domain

Abstract This chapter will provide an overview of the study domain (the Persian Gulf) with respect to the geography, temperature, wind, river discharge, evaporation, desalination capacities, heat budget, and hydrodynamics. This chapter is supposed to serve as not just a general description of the Persian Gulf but also a summary of the sources for some data that are employed in the present study.

2.1 Introduction

The Persian Gulf (also called the "Arabian Gulf" or "the Gulf") is a marginal sea partially enclosed by the continental landmasses of the "Gulf countries" (Bahrain, Iran, Iraq, Kuwait, Qatar, Saudi Arabia, and United Arab Emirates) and connected to the Indian Ocean. It plays a prominent role with respect to transportation, fishing, and water resources (Elshorbagy *et al.*, 2006) and is a region of important military, economic and political significance (Sadrinasab & Kämpf,, 2004). The evaporation in the Persian Gulf is very strong, whereas precipitation and runoff are very limited. Consequently, the Persian Gulf is an inverse estuary governed by the inflow of low-salinity surface water along the Iranian coast and the export of saline bottom water through the Strait of Hormuz (Cavalcante *et al.*, 2011).

2.2 Geography

The Persian Gulf has a surface area of 241,000 km^2, with a maximum length of about 990 km along its axis. The maximum width is about 340 km (between the coasts of the United Arab Emirates and Iran), while the minimum width is 55 m (across the Strait of Hormuz). The Persian Gulf is shallow, usually less than 90 m deep, with a mean depth of about 35 m; therefore, it meets the definition of "shallow water' (Badri *et al.*, 2010). It is connected to the Gulf of Oman through the Strait of Hormuz by a steep continental slope, and the bathymetry is relatively deeper close to the Iranian coast and relatively shallower off the coast of the United Arab Emirates. The peninsula of Qatar is located in the central Gulf, which separates the Persian Gulf into southern and northern parts (Elshorbagy *et al.*, 2006).

2.3 Temperature

Emery (1956) concluded that the surface temperatures throughout the Persian Gulf were almost uniform and about 32.2° in summer, decreasing to around 23.9° in winter. Reynolds (1993)

conducted a set of physical oceanographic measurements which provided a complete dataset that covers the important seasonal transition from mid-winter to early summer. The results showed that the northern part of the Persian Gulf was relatively colder during both summer and winter. Yao and Johns (2010) noticed a meandering front between the Iranian coastal water, which is warm, and the north-western Gulf water, which is cold (Figure 2-1).

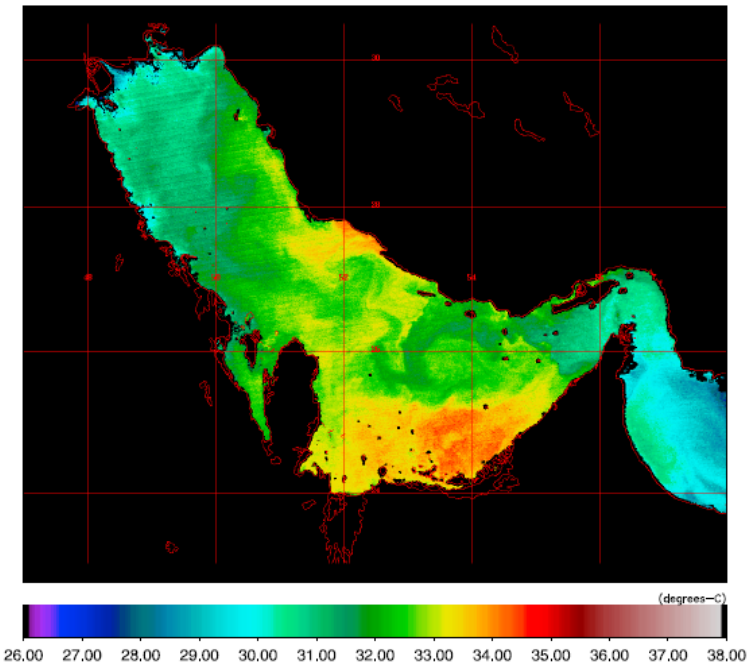

Figure 2-1. Moderate-Resolution Imaging Spectroradiometer sea surface temperature image of the Persian Gulf (11 September 2003) (Yao & Johns, 2010)

2.4 Wind

The year-round northwest wind, the Shamal, is the main wind blowing over the Persian Gulf (Perrone, 1979). However, there are also episodes of southerly winds called Suhaili and a short-term (three to five days) north-easterly wind called Nashi during winter. The winds closer to the Strait of Hormuz are more sensitive to the monsoon cycle (Pous *et al.*, 2013). Moreover, Elshorbagy *et al.* (2006) averaged and combined the Hellerman wind data and the United Arab Emirates Meteorology Department wind data to provide a representation of typical wind fields for the summer and winter seasons.

2.5 River discharge

The total river runoff of the Persian Gulf, as estimated by Reynolds *et al.* (2003), is about 46 cm/yr vertically. The Shatt Al-Arab, also called the "Arvand Round", is a nexus of three major rivers located at the north-western end of the Gulf, with a total runoff of 1456 km^3/yr; the discharges of other major rivers (Hendijan, Hilleh and Mand) are 203 m^3/s, 444 m^3/s, and 1387 m^3/s, respectively. The rivers can supply only a small amount of external water to the Persian Gulf, and hence the inflow through the Strait of Hormuz is the main water source compensating for some of the water lost by evaporation (Elshorbagy *et al.*, 2006). In addition, the river discharges are substantially decreasing due to the development of industry and agriculture (Reynolds, 2003) as well as the establishment of reservoirs and dams (Chao *et al.*, 1992).

2.6 Evaporation

The evaporation in the Persian Gulf is very strong, as it is located in an arid sub-tropical region. The mean evaporation rate, as estimated by Privett (1959), is 1.44 m/year, and the evaporation is relatively stronger during December and weaker in May. According to Elshorbagy (2006), similar features can be observed in an evaporation atlas of the Indian Ocean. Johns *et al.* (2003) also summarized that the evaporation was strongest in winter, and the factor of the variation between winter and summer was about 2. Ross and Stoffers (1978) determined the mean evaporation rate to be 5 m/year, which is much higher than other estimations. Meshal and Hassan (1986) estimated a mean evaporation rate of 2 m/year, and Reynolds *et al.* (2003) confirmed it.

2.7 Desalination capacities

Due to the scarcity of freshwater resources in this area, a large number of desalination plants have been established. According to Dawoud (2012), there are about 200 plants at present and another 38 plants are planned to be built. The total desalination capacity in this area, about 5 billion m^3 per year, is about 45% of worldwide production. A map has been published by Elhakeen and Elshorbagy (2013) showing the cumulative desalination capacities in m^3/day by site location and by country (Figure 2-2). In addition, the total capacity was estimated to rise to 9 billion m^3/yr in 2030, as shown in Figure 2-3.

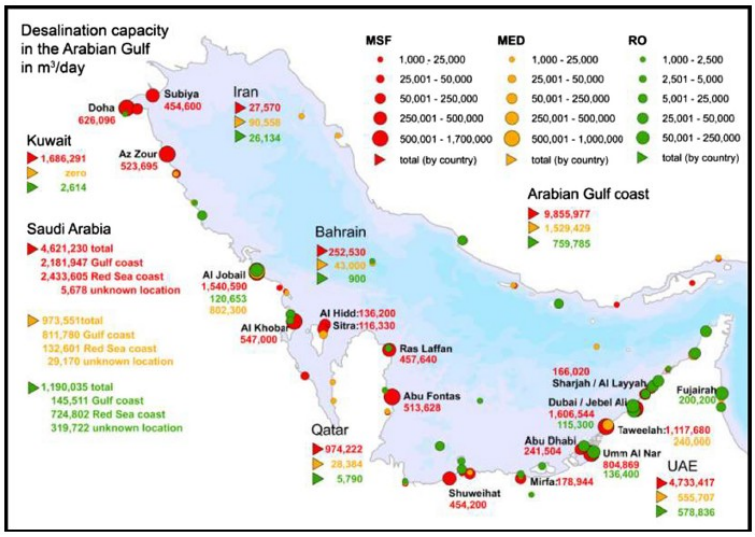

Figure 2-2. Cumulative desalination capacities in m^3/day in the Persian Gulf (Elhakeem & Elshorbagy, 2013)

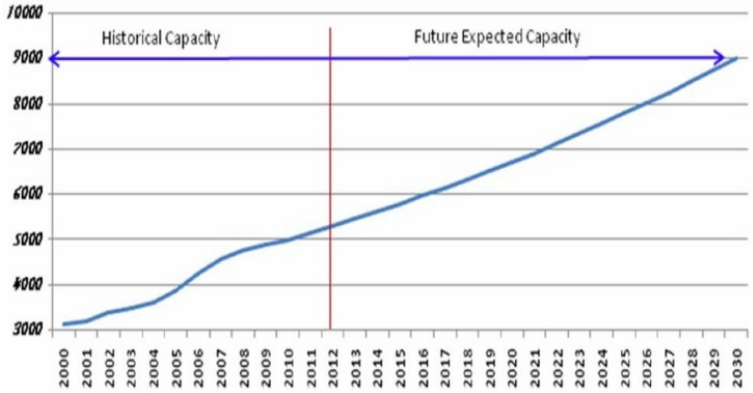

Figure 2-3. Historical and future increases in desalination capacity (in million m^3/yr) in Gulf Cooperation Council countries (Dawoud, 2012)

2.8 Heat budget

Chao *et al.* (1992) summarized the monthly averaged heat budget for the Persian Gulf. The annual mean heat loss in the Gulf, as estimated by Johns *et al.* (2003), was -7.2 ± 4.4 W/m^2, where the negative sign denotes heat loss from the water body to the atmosphere. In the study by Elshorbagey *et al.* (2006), the heat fluxes were neglected, as they were presumed to be small, so the heat budget was only calculated by the summation of net radiation and heat loss by evaporation. Yao and Johns (2010) found that the heat loss was relatively higher during November, December, and January because the evaporation in these months is stronger.

2.9 Hydrodynamics

The main tidal constituents in the Persian Gulf are the principal semi-diurnal lunar and solar tides M_2 and S_2, and the principal diurnal tides K_1 and O_1 (Badri & Wilders, 2010); the periods and wave numbers of the main constituents are summarized in Table 2-1.

Table 2-1. Specifying the periods and wave numbers of the main tidal constituents (Badri & Wilders, 2010)

	M_2	S_2	K_1	O_1
T (hr)	12.42	12.00	23.93	25.85
$k \times 10^6$ (m^{-1})	7.58	7.85	3.94	3.64

Chu *et al.* (1988) simulated the tidal transport in the Gulf using a 2D depth-averaged hydrodynamics and Eulerian-Lagrangian transport model; their results showed that the transport was comparatively stronger along the Iranian shore while it was weaker and slower along the Arabian shore, the shallower part of the Persian Gulf. Johns *et al.* (2003) investigated the exchange between the Gulf and the Indian Ocean using hydrographical and moored ADCP data from the Strait of Hormuz. Their records revealed that the magnitude of the speed of the deep outflow from the Persian Gulf through the Strait of Hormuz was about 20 cm/s. Sadrinasab and Kämpf (2004) conducted a study on the flushing times of the Persian Gulf using a 3D hydrodynamic model, and their results exhibited that the circulation broke up into mesoscale eddies in autumn and winter. In general, the flushing times of surface waters along the Iranian coast were 1-3 years, while those along the coasts of Kuwait and Saudi Arabia were more than 5 years. Elshorbagy *et al.* (2006) simulated the hydrodynamics of the Persian Gulf using a 3D rectilinear-grid coastal flow model in an effort to comprehensively characterize the water dynamics of the Persian Gulf. Their results, verified by field measurements conducted in Dubai, Abu Dhabi and Ruwais, revealed that the flow field tended to move southward in the Persian Gulf during summer; parallel flows occurred along the Saudi Arabian coast, and stronger flows were exhibited at the tip of the Qatar Peninsula. They predicted a mean outflow of 0.07 S_v with a residence time of about 3.9 years near the Strait of Hormuz, the volume of which was nearly 8,630 km^3.

2.10 Summary

This chapter demonstrated that the problem about salinity in the region of the Persian Gulf can be very serious. In the first place, the evaporation is much stronger than the sum of the precipitation and river discharges; in other words, the Persian Gulf is an inverse estuary. Secondly, the communication between the Gulf water and the Indian Ocean water is restricted because of the existence of the Strait of Hormuz. In addition, there is a high demand of desalination plants in this region, while desalination is among the most important human activities that can influence the salinity in water bodies.

As introduced in Chapter 1, the objective of this thesis is to conduct a study of numerical modeling of salinity distribution in a large-scale inverse estuary, and make a numerical prediction of the long-term variations of salinity in the Persian Gulf. Therefore, in the next chapter, we will review the literature related to these objectives.

Chapter 3 Literature Review

Abstract This chapter will begin by introducing the theoretical background associated with the current thesis. Then, some previous studies on the topic of salinity distribution in estuaries will be categorized (observational methods, analytical methods and numerical methods) and reviewed. The applicability of these methods or models will be discussed. And finally, this chapter will be summarized and some useful conclusions will be drawn.

3.1 Theoretical Background

3.1.1 Governing Equations of Flow Motions

The continuity, momentum and energy equations are the fundamental governing equations of fluid motions. The continuity equation states the conservation of mass; the momentum equation is derived according to the Newton's second law; and the energy equation (also called Bernoulli equation) is based on the conservation of energy (Prasuhn, 1992).

Various methods for describing a fluid have been developed, and a comprehensive review of these methods can be found in Shaughnessy, *et al*. (2010). The Lagrangian and Eulerian descriptions are the most widely used methods. A particle of fluid is the fundamental entity in the Lagrangian description. The fluid is assumed to be composed of discrete particles of fluid, each of which carries its own properties, and Lagrangian description tracks the complete histories of each individual fluid particle to describe the entire fluid behaviour. In the Eulerian description, the coordinate system serves as a backdrop for fluid motion, which means that this method records the changes of the flow properties with time at fixed points in space.

The Lagrangian description is easier to understand; however, its computational cost is high; therefore, normally it is applied only for relatively specified applications. The Eulerian is more theoretically complicated; however, it is mathematically simple. The governing equations of fluid motions are comprehensively summarized by Anderson and Wendt (1995). The governing equations in Eulerian form are summarized below, and those in Lagrangian form are summarized in Appendix 2.

Continuity equation:

$$\frac{\partial \rho}{\partial t} + \nabla \cdot (\rho \vec{v}) = 0 \tag{1}$$

where ρ denotes the density; $\vec{v} = (u, v, w)$ represents the velocity; ∇ is the divergence.

Momentum equations (x, y, z components):

$$\frac{\partial (\rho u)}{\partial t} + \nabla \cdot (\rho u \vec{v}) = -\frac{\partial p}{\partial x} + \frac{\partial \tau_{xx}}{\partial x} + \frac{\partial \tau_{yx}}{\partial y} + \frac{\partial \tau_{zx}}{\partial z} + \rho f_x \tag{2}$$

$$\frac{\partial (\rho v)}{\partial t} + \nabla \cdot (\rho v \vec{v}) = -\frac{\partial p}{\partial y} + \frac{\partial \tau_{xy}}{\partial x} + \frac{\partial \tau_{yy}}{\partial y} + \frac{\partial \tau_{zy}}{\partial z} + \rho f_y \tag{3}$$

$$\frac{\partial (\rho w)}{\partial t} + \nabla \cdot (\rho w \vec{v}) = -\frac{\partial p}{\partial z} + \frac{\partial \tau_{xz}}{\partial x} + \frac{\partial \tau_{yz}}{\partial y} + \frac{\partial \tau_{zz}}{\partial z} + \rho f_z \tag{4}$$

where p is the pressure; τ_{ij} denotes a stress in the j direction exerted on a plan perpendicular to the i axis; $\vec{f} = (f_x, f_y, f_z)$ denotes the body force per unit mass acting on the fluid element.

Energy equation:

$$\begin{aligned} \frac{\partial}{\partial t}\left[\rho(e + \frac{V^2}{2})\right] + \nabla \cdot \left[\rho(e + \frac{V^2}{2})\vec{v}\right] &= \rho \dot{q} + \frac{\partial}{\partial x}(k_T \frac{\partial T}{\partial x}) + \frac{\partial}{\partial y}(k_T \frac{\partial T}{\partial y}) + \frac{\partial}{\partial z}(k_T \frac{\partial T}{\partial z}) \\ &- \frac{\partial (up)}{\partial x} - \frac{\partial (vp)}{\partial y} - \frac{\partial (wp)}{\partial z} + \frac{\partial (u\tau_{xx})}{\partial x} \\ &+ \frac{\partial (u\tau_{yx})}{\partial y} + \frac{\partial (u\tau_{zx})}{\partial z} + \frac{\partial (v\tau_{xy})}{\partial x} + \frac{\partial (v\tau_{yy})}{\partial y} \\ &+ \frac{\partial (v\tau_{zy})}{\partial z} + \frac{\partial (w\tau_{xz})}{\partial x} + \frac{\partial (w\tau_{yz})}{\partial y} + \frac{\partial (w\tau_{zz})}{\partial z} + \rho \vec{f} \cdot \vec{v} \end{aligned} \tag{5}$$

where e is the internal energy per unit mass; $V^2 / 2$ represents the kinetic energy per unit mass; $\dot{q}$ refers to the rate of volumetric heat addition per unit mass; k_T is the thermal conductivity.

3.1.2 Governing Equations of Flow Motions with Coriolis Term

When the motion is described relative to a rotating reference frame, such as the Earth, there will be a deflection of the moving objects, and this effect is called Coriolis Effect, which is named after Gaspard-Gustave Coriolis.

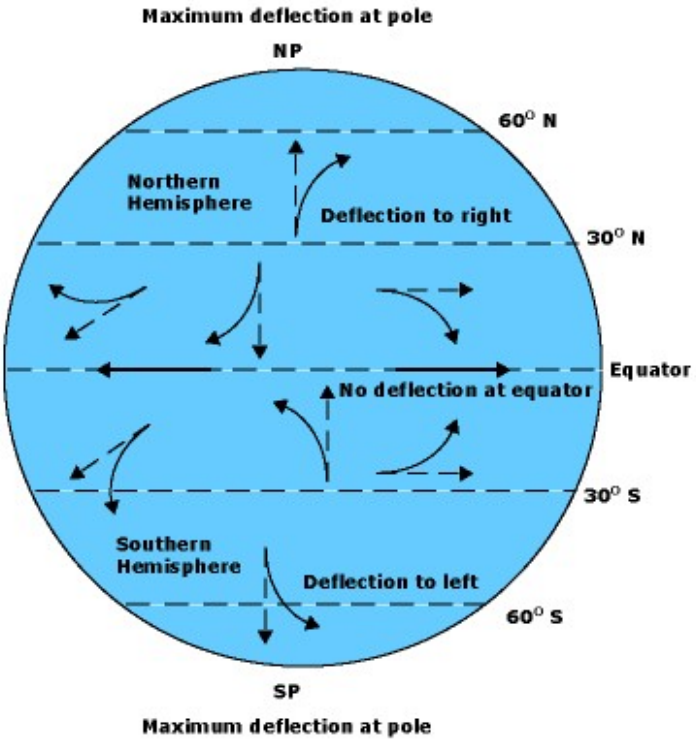

Figure 3-1. The Coriolis Effect (TOH, 2015)

The Coriolis term leads to the effect that everything that moves over the surface of earth tends to slide to the right of the motion in the Northern Hemisphere and to the left of the motion in the Southern Hemisphere (TOH, 2015; Figure 3-1).

For small-scale water bodies, the Coriolis Effect is negligible, but for large-scale objects, it should not be neglected any more. Besides, because of the constraint of the surface of the earth, the vertical component of the Coriolis force is more negligible than the horizontal components (McDonald, 1952).

As the Earth can be regarded as a rotating reference frame, so it is generally necessary to transform the governing equations of fluid motions from inertial frame of reference to the rotating coordinates. This can be simply achieved by incorporating the Coriolis term (a derivation can be found in Appendix 2) into the governing equations of fluid dynamics. Marshall and Plumb (1995) have written the rotating equations of motion in the succinct form:

$$\frac{D\vec{v}}{Dt}+\frac{1}{\rho}\nabla p+\nabla\phi=-2\vec{\Omega}\times\vec{v}+F \qquad (6)$$

where ϕ represents geo-potential, and F is the forcing and dissipation.

3.1.3 Fundamental Knowledge of Estuaries

The governing equations described in the previous have given some clues about the dynamics of flow, and this section will mainly focus on estuaries.

An estuary can have different terminologies, and most of the time, they can be used interchangeably. For example, besides “Estuary”, it can also be referred to as “River-Sea Mixing Zone” (Peterson *et al.*, 2008), “bay” (Austin, 2004), and “River Mouth”.

The definition given by Pritchard (1967) is usually employed for an estuary: a semi-closed coastal water body which has free water exchange with the sea and where seawater is diluted by freshwater running from the land. There is also a more general definition: an estuary is a semi-enclosed body of water connected to the open ocean and receiving freshwater from rivers, runoff and seepage (Elliott & McLusky, 2002). The first definition of an estuary will not be used in the present thesis since it only refers to classical estuaries, whereas the Persian Gulf is an inverse estuary, within which the seawater is concentrated by the Gulf water (primarily because of the net freshwater loss).

Estuaries are closely linked to humans, as they are highly populated and the resources in these areas are being increasingly exploited. They also play a critical role in a wide range of oceanic processes like the oceanic biogeochemical cycling (Howarth *et al.*, 2011). Additionally, estuaries can be significantly influenced by anthropogenic activities and climate.

An estuary can be defined as a classical estuary or an inverse estuary, according to whether the seawater it is diluted or concentrated. An estuary can also be classified based on various other criteria, such as the geomorphology, fluid dynamics, and tidal influence as well as river mouth areas (see Table 3-1). Most frequently, an estuary is categorized according to the distribution of the salinity (Savenije, 2012), as expressed in Figure 3-2: stratified, partially mixed, and well mixed.

Table 3-1. Types of estuaries classified by various criteria

Criteria	Reference	Types
Geomorphology	Pritchard, D., 1967	Drowned River Valleys, Fjord Type, Lagoon Type, and Produced by Tectonic Processes
Fluid Dynamics	Dolgopolova & Isupova, 2010	Salt Wedge, Highly Stratified, and Weakly Stratified.
Tidal Influence	Savenije, 2012	Ideal Type, Amplified Type, and Damped Type.
River mouth area	Mikhailov & Gorin, 2012	Liman Type, Channel Type, Lagoon Type, Marine Type.

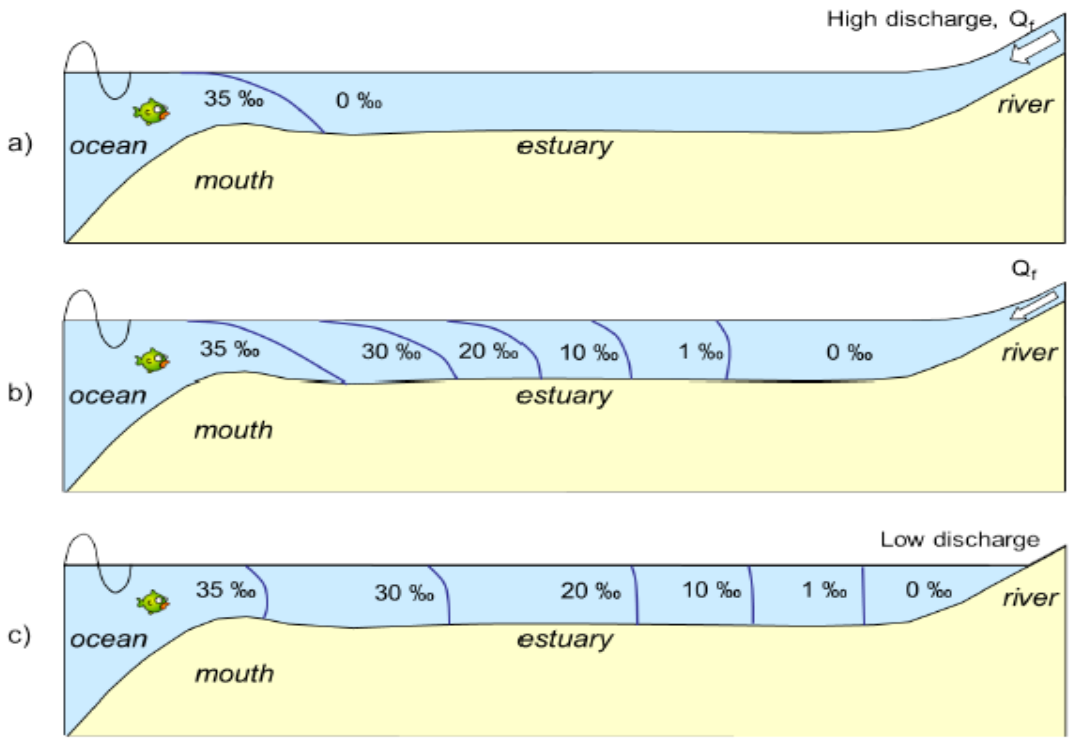

Figure 3-2. Longitudinal distribution of the salinity: (a) Stratified, (b) Partially Mixed, (c) Well Mixed (Savenije, 2012)

3.2 Previous Studies on Salinity Distribution in Estuaries

Salinity distribution in estuaries has been a topic of significant research interest, and related studies can be classified into three categories: observational methods, analytical methods, and numerical methods.

3.2.1 Observational Methods

Observational studies of salinity distribution in estuaries can basically be conducted in two ways: field work or remote sensing analysis.

Liu and Bao (2011) studied the spatial distribution of salinity and analyzed the mechanism of saltwater intrusion in the Modaomen Water channel of Peer River estuary using an observational method. They conducted field observations of velocity and salinity of upper, middle and lower water layers at the hydrological stations along the Modaomen estuary. They plotted and analyzed the hydrographs of velocity and salinity in the channel according to their measurements. The results show the unique characteristics of the transport of salinity in Modaomen channel: the salinity in the Modaomen channel decreases when the tidal range increases from neap to spring tide.

Wang and Xu (2008) stated that it is very costly and time-consuming to monitor the spatial and temporal variability of salinity for a large estuary, so they applied remote sensing techniques for their study of the salinity in Lake Pontchartrain, a large estuarine lake in the Northern Gulf of Mexico. Using banding noise reduction and radio-metrical correction approaches, they extracted remote sensing data from Landsat Thematic Mapper (TM) images. By using ordinary least square and ridge regression methods for the Landsat TM imagery and field measurements of the salinity, they developed a model for the salinity distribution for the study domain. The results show that the model performs well in predicting the lake salinity. They also examined the relationships between the magnitudes of salinity with water-leaving reflectance from the remote sensing technique, and analyzed the influence of storm surges on the variation of salinity in the study domain. This study demonstrated the utilization of remote sensing techniques for salinity distribution in large estuaries, and pointed out the importance of freshwater discharge on the salinity distribution.

3.2.2 Analytical Methods

Analytical methods are mainly based on diffusion equations:

$$\frac{\partial C}{\partial t} = D\frac{\partial^2 C}{\partial x^2} \tag{7}$$

This one form of Fick's second law is governing one-dimensional transient diffusion of particles in estuaries, where C is the concentration of the particle; t denotes time; x is the direction of transport; and D is the coefficient of diffusion for the particles in an estuary.

If the chemical species is radioactive and undergoes first-order decay, then this equation must be modified to take into account the effect of this decay on the temporal distribution of the particles, as follows:

$$\frac{\partial C}{\partial t} = D\frac{\partial^2 C}{\partial x^2} - \lambda C \tag{8}$$

where λ is the decay rate.

The Fickian coefficient D can be regarded as the dispersion coefficient, the estimation of which is one of the most crucial parts in analytical studies of salinity distributions in estuaries. Two assumptions are commonly utilized in analytical studies of salinity distributions in estuaries: the steady-state assumption, or salt-balance assumption; and, one-dimensional assumption, or well-mixed assumption.

3.2.3 Numerical Methods

For analyzing the salinity distribution in an estuary, numerical simulations can be conducted. Two numerical works closely related to this thesis are reviewed in this section. The first study used the MITgcm model, which is the primary numerical model in the present project. The second study checked the salinity distribution in an inverse estuary, which is similar to the case of the Persian Gulf.

In order to study intertidal and along channel variability in stratification and mixing in the Hudson River estuary, Stenstrom (2004) performed a three-dimensional numerical modeling, using the MITgcm model.

The modeled fields show good agreement with observations, both qualitatively and quantitatively. The author stated that the model was in fact able to reproduce observational results, including microstructure data, and that numerical modeling can be a useful complement to observations in similar studies. In these simulations, the grid resolution was high, and the results agreed well even quantitatively with observations, in spite of the fact that a rather simplistic turbulence closure scheme was used. It should be useful though in future studies to further develop and evaluate the closure scheme, particularly for studies where a coarser grid resolution has to be used for computational feasibility.

The Hybrid Coordinate Ocean Model (HYCOM) was employed by Chang *et al.* (2008) to study the outflow of warm, salty, dense water from the Red Sea into the western Gulf of Aden. The model allows smoothly varying combination of depth, density and terrain-following coordinate. The model topography was based on multi-beam echo soundings, and these data had a horizontal resolution about 200 m and covered the whole domain that was interested by the authors. Remote areas and gaps were filled with gridded seafloor data. The authors have conducted several sensitivity studies of the results to the horizontal grid spacing, two entrainment parameterizations (TPX and K-profile parameterization), and forcing at the source location. They also examined the role of the horizontal resolution on the results by changing the grid size from 5 km to 0.5 km, which are typical size for coastal modeling applications; and vertically, they used 16 layers for all numerical experiments.

The modeled salinity was compared to the observed values during the 2001 Red Sea Outflow Experiment. The observed and modeled distributions of temperature and salinity profiles are compared at eight locations, and the agreement between the modeled results and the observed salinity profiles along the channels is satisfactory.

These two models and some other frequently used models are summarized below:

MITgcm

MITgcm (MIT General Circulation Model) is a numerical model designed for the study of the atmosphere, ocean and climate; it can cover a very wide range of phenomena because of its non-hydrostatic formulation, from the advection of flow on a small scale to a global-scale case (Adcroft *et al.*, 2004, Figure 3-3).

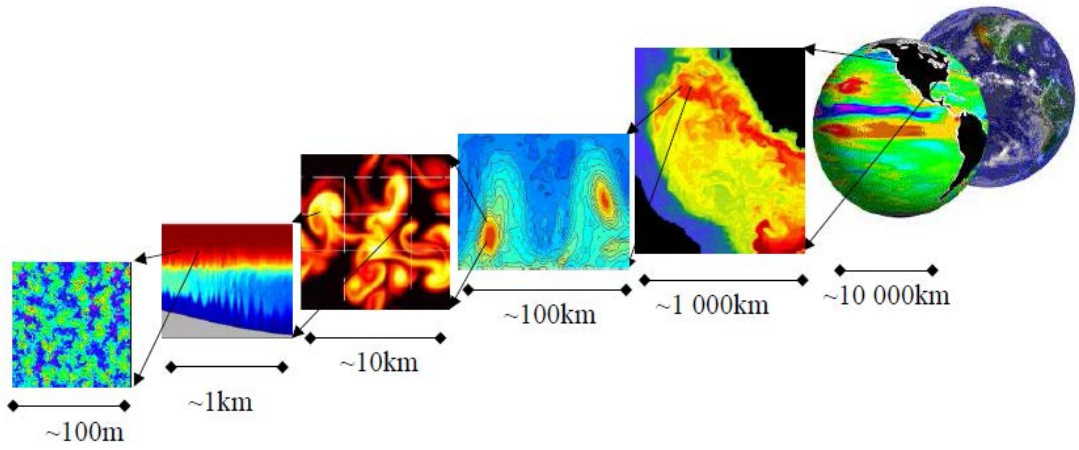

Figure 3-3. The range of phenomena that can be studied by the MITgcm (Adcroft et al., 2004).

Applications of MITgcm includes studies of hydraulics and mixing in the Hudson River estuary (Stenström, 2004), a regional ocean climate model for the Mediterranean Sea with a two-way grid refinement at the Strait of Gibraltar (Artale, 2007), and the role of wind on the detachment of low salinity water in the Changjiang Estuary in summer (Xuan, 2012).

HYCOM

The Hybrid Coordinate Ocean Model (HYCOM) is a data-assimilative hybrid isopycnal-sigma-pressure coordinated ocean model. It allows smoothly varying combination of depth, density and terrain-following coordinate. Chang *et al.* (2008) used it to study the outflow of warm, salty, dense water from the Red Sea into the western Gulf of Aden.

DieCAST

Dietrich Center for Air-Sea Technology (DieCAST) is a primitive equation, z-level vertical coordinate, rigid-lid, finite difference ocean model. This model uses accurate control volume fourth order numerical methods, and is figured with reduced numerical dispersion. An example of the application of this model is the investigation of the salinity in the Mediterranean Sea (Fernández *et al.*, 2005).

Delft3D

Delft3D is an open source, flexible integrated modeling suite. It is primarily used in the free surface water environment and it can simulate two-dimensional and three-dimensional flow, sediment transport and water quality and so on. Kuijper and Van Rijn (2011) used Delft 3D for their study of salinity distribution in prismatic and convergent tidal channels.

ROMS

Regional Ocean Modeling System (ROMS) is a finite difference, free-surface, terrain-following, primitive equations ocean model. This model solves the governing equations of flow dynamics in curvilinear grids; besides, the Boussinesq and hydrostatic approximations are applied. It is widely used by the scientific community for a diverse range of applications; for examples, Di Lorio and Castelao (2013) employed it to investigate the spatial and temporal patterns of salinity distribution across three adjacent estuaries in the Georgia Coastal Ecosystems Long Term Ecological Research domain; Janekovic (2010) checked the Adriatic Sea surface salinity by using this model.

FVCOM

Finite Volume Community Ocean Model (FVCOM) is a prognostic, unstructured-grid, finite-volume, free-surface, 3D primitive equation coastal ocean circulation model. The model contains momentum, continuity, temperature, salinity and density equations, and it is closed physically and mathematically using turbulence closure sub-models. Georgiou *et al.* (2009) conducted a set of numerical experiments using this model to study the impact of multiple freshwater diversions on the salinity distribution in the Pontchartrain estuary.

Branched Model Proposed by Liu et al., (2007)

Liu *et al.* (2007) developed a branched, laterally integrated, 2D, real-time model. The models uses a z coordinate in the vertical direction and two-time level, finite difference numerical method. The model is capable of modeling river loop. This model has been used for the study of the effect of channel connection on flow and salinity distribution of the Danshuei River estuary.

3.3 Discussion

3.3.1 Application of Observational Methods in the Present Thesis

Observational methods can be used for the present project in obtaining basic data, calibration and validation of the numerical model. Field observations can provide accurate data, but they are extremely time-consuming and expensive, especially for large-scale and long-term cases such as the case in this thesis. The remote sensing techniques are pretty promising but they can only produce satisfactory data at the water surface, and are susceptible to cloud. In addition, these two observational methods are not able to predict the future situation. According to these considerations, the data based on observational methods are employed in this thesis mainly for obtaining necessary input of the model (e.g. bathymetry, initial condition of the salinity, etc.), calibration and validation of the numerical models (by comparing the measured and modeled salinity). Appendix 3 introduces some of the relevant instrument.

3.3.2 Application of Analytical Methods in the Present Thesis

It is commonly considered that despite their usefulness in predicting estuarine flows, analytical models involve a lot of simplifying assumptions and thus are not able to adequately capture some observed flow properties, especially in large-scale estuaries with realistic topography and complex climate conditions. Therefore, analytical methods will not be exploited in the current thesis. A more detailed discussion has been presented in Appendix 3.

3.3.3 Application of Numerical Method in the Present Thesis

Numerical modeling method will be the central focus in this thesis. Numerical simulations of salinity distribution in estuaries have been widely performed, particularly with the recent advances in computational techniques and resources, which means that numerical modeling methods are more feasible. Numerical methods are cost-effective and less time-consuming compared to observational methods; and are more applicable and reasonable than analytical method.

The majority of previous simulations were limited in time from a few hours to a few months, which might not be sufficient enough for validation of the employed models and inspections of

long-term characteristics. Therefore, the present project will conduct simulations for a basin-wide and long-term case.

Detailed assessments of the performance of various approaches or algorithms have not been reported in the literature related to numerical simulations of salinity distributions in inverse estuaries, to the best of the author's knowledge. Therefore, this thesis will evaluate the approaches and algorithms before using the numerical model to predict the future situation.

MIT general circulation model (MITgcm) will be used as the main model in this thesis. Firstly, it can examine a wide range of phenomena. Secondly, MITgcm is open source, so it is easier to use it to understand the numerical mechanisms and to evaluate various numerical approaches or algorithms. Finally, it can be integrated with other models easily, which enables it to be used for further or other studies, such as the water quality, biological and ecological issues in water bodies.

3.4 Summary and Conclusions

This chapter reviewed the literature associated with this thesis; it has introduced the theoretical background, summarized some widely used models, and presented some important previous studies.

Numerical method will be the main tool for the current study, as it is less time-consuming and much cheaper than observational method; and it is more applicable for large-scale complex cases. Besides that, the MIT general circulation model will be utilized to simulate the phenomenon that will be examined.

In the next chapter, we will illustrate the methodologies that are employed in this thesis.

Chapter 4 Methodology

Abstract This chapter will introduce the numerical model (MITgcm) and the governing equations employed in this thesis. Then it will summarize the discretization methods, and explain several numerical algorithms that will be investigated. In addition, the methods for preparing the data and dealing with the boundary conditions will also be presented. Finally, in the end of this chapter, the model setup will be described.

4.1 Numerical Model

MITgcm (MIT General Circulation Model), developed at the Massachusetts Institute of Technology, has been chosen to be the primary model for this study. It is a numerical model designed for the study of the atmosphere, ocean and climate, and it can cover a very wide range of phenomena because of its non-hydrostatic formulation, from the advection of flow on a small scale to a global-scale case, as stated in Chapter 3.

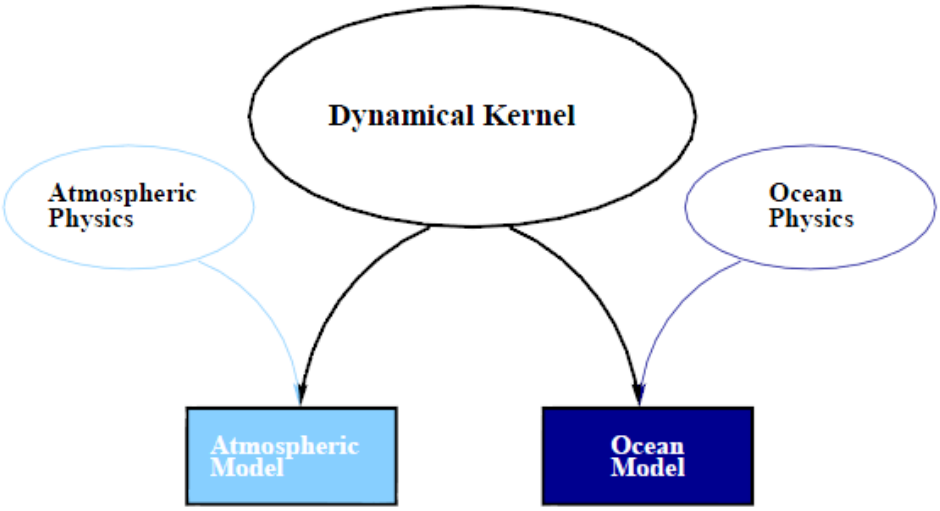

Figure 4-1. MITgcm has a single dynamical kernel that can drive forward either oceanic or atmospheric simulation (Adcroft et al., 2004).

A distinct feature of MITgcm is that it can be used to study both atmospheric and oceanic phenomenon with one hydro-dynamical kernel (Adcroft *et al.*, 2004; Figure 4-1); therefore it is an extremely powerful tool, particularly when both atmospheric and oceanic problems are under inspections.

4.2 Governing Equations

The horizontal momentum equation, the vertical momentum equation, and the continuity equation utilized in the present study can be expressed, respectively, as (Adcroft *et al.*, 2008):

$$\frac{D\vec{v}_h}{Dt} + (2\vec{\Omega} \times \vec{v})_h + \nabla_h \phi = F_{\vec{v}_h} \tag{9}$$

$$\nabla_h \cdot \vec{v}_h + \frac{\partial \dot{r}}{\partial r} = 0 \tag{10}$$

and

$$\frac{D\dot{r}}{Dt} + \hat{k} \cdot (2\vec{\Omega} \times \vec{v}) + \frac{\partial \phi}{\partial r} + b = F_{\dot{r}} \tag{11}$$

where

D / Dt = total derivative (also called variously the "Lagrangian derivative", the "substantial derivative", or the "material derivative");

$\vec{v} = (u, v, \dot{r})$ = the velocity;

Ω = the Earth's rotation;

ϕ = the geo-potential;

$\hat{k}$ = a unit vector in the vertical direction;

F_v = forcing and dissipation of $\vec{v}$.

The equation for potential temperature and equation for salinity can be expressed as (Adcroft *et al.*, 2008):

$$\frac{D\theta}{Dt} = F_\theta \tag{12}$$

and

$$\frac{DS}{Dt} = F_S \ , \tag{13}$$

where

θ = potential temperature;

S = the salinity;

F_θ = the forcing and dissipation of θ;

F_S = the forcing and dissipation of S.

4.3 Discretization Methods

In order to solve the governing equations described in previous section, discretization method is used to transfer the differential equations into discrete counterparts. In this thesis, the finite volume method is employed, after a comparison of advantages and disadvantages of the three most widely used discretization methods: finite difference method (FDM), finite volume method (FVM) and finite element method (FEM) (Ferziger & Perić, 2002).

- **Finite Difference Method.** Finite difference method (FDM) is one of the oldest methods for partial differential equations' numerical solutions. In this method, the domain is treated as a grid of discrete points, and at each point, the partial derivative is substituted by the finite-difference approximation with respect to the nodal value of the function. In this way, the partial differential equation is converted into an algebraic equation. Finite difference method is very simple and straightforward for structured grids; however, on irregularly shaped boundaries or unusual geometries, the restriction to regular geometries is a significant disadvantage of it. More specifically, for the case of the Persian Gulf, finite difference method is less likely to be applicable since the boundaries and geometries are not regular.

- **Finite Volume Method.** Finite volume method (FVM) offers an alternative to find numerical solutions of partial differential equations. In this method, the partial differential equations are substituted by approximations in terms of a control volume surrounding a point, instead of replacing the partial differential equations with

approximations at the point. Finite volume method can be applied for any type of grid, even for irregular geometries. This method is very easy to understand, and is relatively simple for calculations on computers. A disadvantage of finite volume method is that it is difficult to be used in three-dimensional problems when the order is higher than second, due to the fact that three levels of approximation (interpolation, differentiation, and integration) are performed in this method. In this thesis, the hydrostatic approximation is made and the second order numerical method is used, so the drawbacks of finite volume method have been avoided .Therefore, this method is quite suitable for the current project.

- **Finite Element Method.** Finite element method (FVM) provides another way to approximate the partial differential equations. In finite element method, the domain is divided into neither discrete points nor volumes; instead, the domain is divided into simply shaped regions, or elements. These elements are typically unstructured, such as triangles in two-dimensional simulations and tetrahedral in two-dimensional analyzes. Approximations are calculated for each of these elements and then all of these approximate solutions are assembled together to obtain the overall solution. Finite element method is very advantageous for irregular grids or boundaries; in fact, it is able to deal with arbitrary geometries or boundaries, and the grids can be easily refined. The main disadvantage of it is that when unstructured grids are used, the matrices of the linearized equations become more complex.

4.4 Numerical Algorithms

Previous studies used various numerical algorithms with little emphasis on why they chose their algorithms. This thesis will examine the performance of several widely used numerical algorithms and find out the optimal combination of them. This section lays out the methods for dealing with free surface in the momentum equations first; and afterwards, the advection algorithms for tracer equations will be described.

4.4.1 Methods for dealing with free surface in the momentum equations

The free surface in momentum equations is usually modeled by two approaches (hereinafter referred to as momentum methods); one is the rigid lid method and the other is the free surface

method. These two methods differ in the upper boundary conditions: the rigid lid method does not allow vertical displacements of the water surface, while the free surface method uses a freely evolving surface.

Rigid Lid Method

Bryan (1969) proposed the well-known "rigid-lid" approximation, which sets the vertical velocity to zero at the surface by fixing the water surface to be flat. The pressure variations at the upper surface are maintained by assuming there is a force that would be exerted by a rigid lid. It is computationally efficient since it excludes the kinematic effects of small displacements of the upper surface and filters out the high-frequency surface gravity waves. This most widely-used assumption can be expressed as:

$$\dot{r}(0) = 0 \tag{14}$$

Smith *et al.* (1992) implemented a numerical formulation of the barotropic equations to solve for the surface-pressure field. This method is referred to as the "rigid lid surface pressure" method, and has many advantages over the so-called "rigid lid stream-function" method (Bryan, 1969) when the volume transport stream-function is solved: it can facilitate the computation; it can include any number of islands at no extra cost; and it can handle steep gradients in the bottom topography.

Free Surface Method

Integration of the continuity equation gives:

$$\partial_t \eta + \nabla \cdot \mathbf{U} = P - E + R \tag{15}$$

where

η = the surface elevation measured from the resting position at $z = 0$;

∇ = the horizontal gradient operator;

$\mathbf{U}$ = the vertically integrated horizontal velocity;

P = precipitation;

E = evaporation;

R = runoff.

The rigid-lid mode sets $\partial_t \eta = 0$, but this approximation can be eliminated (see e.g. Dukowicz & Simith, 1994) to allow for a free surface and the introduction of fresh water, allowing better accuracy than the rigid-lid approach. In order to overcome the time step restriction imposed by the high-frequency waves, an implicit time-stepping scheme for the barotropic equations is used. This method is known as the "implicit free surface" method, and it has many advantages: it has a high computational efficiency; it can compute the surface height directly; and it can simulate the barotropic Rossby and planetary waves accurately. The free surface method developed by Killworth *et al.* (1991) used an explicit time-stepping scheme, which can be called the "explicit free surface" method. This method has been improved by Griffies *et al.* (2001), and is advantageous with respect to stability properties and conservation of tracers.

4.4.2 Advection algorithm for tracing equations

There are various advection algorithms for the advection-diffusion part of the tracer equations (Adcroft, 2008; Figure 4-2). Two algorithms, the Adams-Bashforth method and the Lax-Wendroff method, are of interest in the present study because of their widespread use.

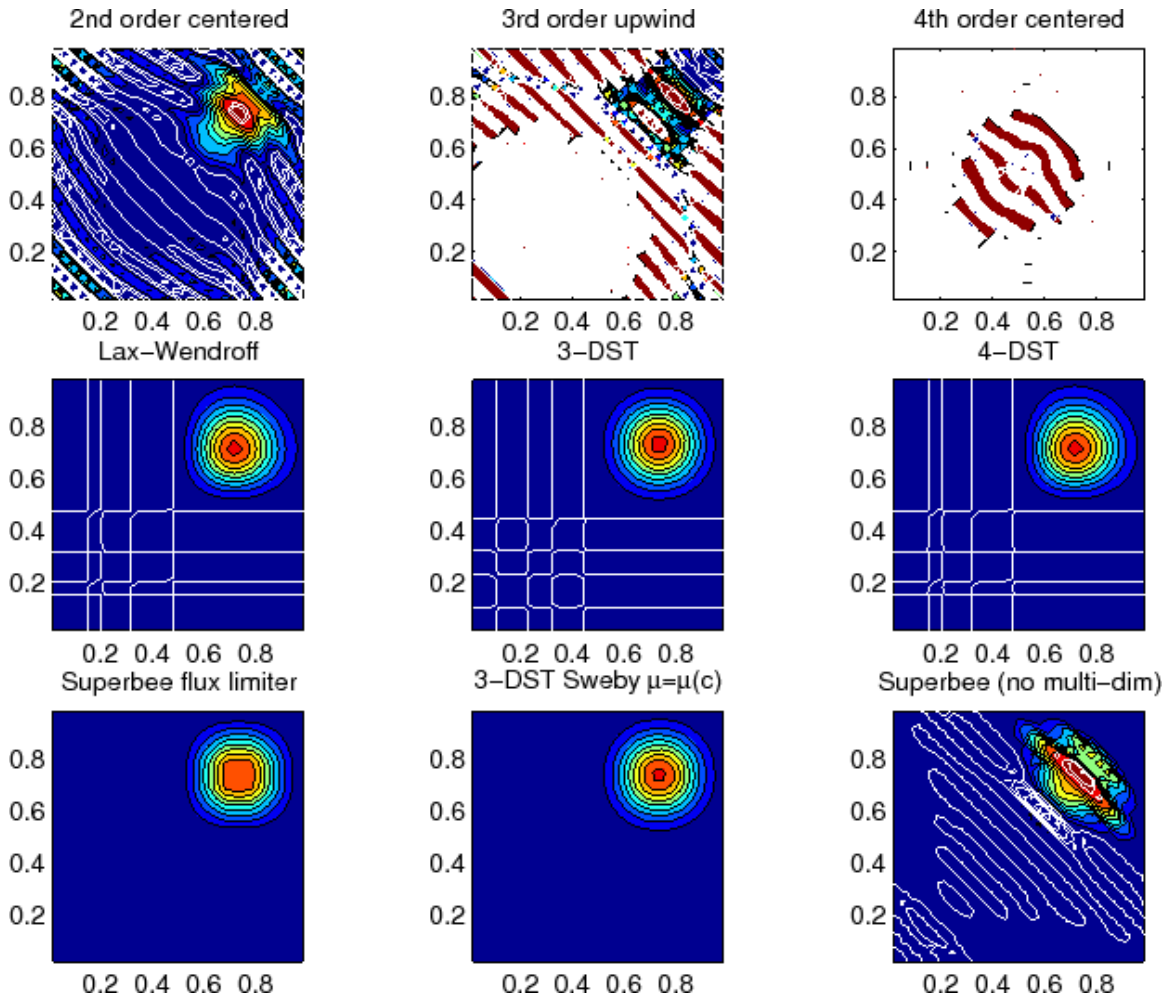

Figure 4-2. Results produced by various advection schemes (Adcroft, 2008)

Adams-Bashforth Approach

Consider the first-order ordinary differential equation:

$$\frac{du}{dt} = f(\mathrm{u}), \tag{16}$$

We can write:

$$u^{n+1} = u^n + \int_{n\Delta t}^{(n+1)\Delta t} \frac{du}{dt} dt = u^n + \int_{n\Delta t}^{(n+1)\Delta t} f(\mathrm{u}) dt \tag{17}$$

where

u^n = the numerical approximation to $u(n\Delta t)$;

n = 0, 1, 2, 3,…;

Δt = the time step.

Based on the idea of using an $(N-1)$ th-order polynomial to approximate the integrand, we can get the N th-order Adams-Bashforth approximation, the general form of which is (Durran, 1991):

$$u^{n+1} = u^n + \Delta t \sum_{j=0}^{N-1} a_j f(\mathrm{u}^{n-j}) \tag{18}$$

where

N = the order;

a_j = coefficients.

The first-order Adams-Bashforth method is simply the forward Euler Method. The second-order Adams-Bashforth method is very popular, and it reads as (Zhao and Zhang, 2011):

$$u^{n+1} = u^n + \Delta t f(\mathrm{u}^{n+1/2}) \tag{19}$$

where

$$f(\mathrm{u}^{n+1/2}) = \frac{3}{2} f(\mathrm{u}^n) - \frac{1}{2} f(\mathrm{u}^{n-1}) \tag{20}$$

It is known as an explicit two-step method (Singh *et al.*, 2013), as it contains two previously computed solutions u^{n-1} and u^n.

Lax- Wendroff Approach

The Lax-Wendroff algorithm, based on the finite difference technique, was developed by Lax and Wendroff (1960) to solve hyperbolic partial differential equations numerically. The Lax-

Wendroff method is described here, with the one-dimensional advection equation written below as an example:

$$\frac{\partial u}{\partial t} = -c\frac{\partial u}{\partial x} \tag{21}$$

where

$u(\mathrm{x},\mathrm{t})$ = a scalar field

c = the constant speed of a flow.

The Lax-Wendroff method consists of two stages. The first stage computes the scalar field for half of a time step on a half-step grid:

$$u_{j+1/2}^{n+1/2} = \frac{1}{2}(u_j^n + u_{j+1}^n) - \frac{v\Delta t}{2\Delta x}(u_{j+1}^n - u_j^n) \tag{22}$$

$$u_{j-1/2}^{n+1/2} = \frac{1}{2}(u_j^n + u_{j-1}^n) + \frac{v\Delta t}{2\Delta x}(u_{j-1}^n - u_j^n) \tag{23}$$

where

n = the temporal index

j = the spatial index.

The solution at the new time level is calculated in the second stage:

$$u_j^{n+1} = u_j^n - \frac{v\Delta t}{\Delta x}(u_{j+1/2}^{n+1/2} - u_{j-1/2}^{n+1/2}) \tag{24}$$

Combine the above equations, we get:

$$u_j^{n+1} = u_j^n - \frac{v\Delta t}{2\Delta x}(u_{j+1}^n - u_{j-1}^n) + \frac{1}{2}(\frac{\Delta t}{\Delta x})^2(u_{j+1}^n - 2u_j^n + u_{j-1}^n) \tag{25}$$

The Lax-Wendroff method is also known as an explicit two-step method and is second-order accurate in space and time (Machalinska-Murawska and Szydlowski, 2014).

4.5 Mixing Parameterization

There are various methods for setting the vertical viscous and diffusive coefficients. The vertical mixing parameterization proposed by Large *et al.* (1994) is used in the present thesis, since it has been widely used in open ocean settings. This parameterization is called nonlocal K-Profile parameterization. This method matches separate parameterizations for vertical mixing of the surface boundary layer and the ocean interior.

Viscosity and diffusivities for the water column above a calculated boundary layer depth can be expressed as

$$\nu_{surface} = d_{sufacelayer} \nu_{turbulent}(\delta) s_{shape}(\delta) \tag{26}$$

where

$\nu_{surface}$ = the viscosity and diffusivities for the water column above a calculated boundary layer depth;

$\nu_{surface}$ = the length scale of the calculated surface boundary layer depth;

$v_{turbulent}$ = the turbulent velocity scale for one of momentum, temperature and salinity;

δ = a non-dimensional coordinate ranging from zero to one, which is used for representing depth within the surface boundary layer;

s_{shape} = a non-dimensional shape function.

The surface boundary layer depth $d_{sufacelayer}$ is determined as the minimum of the Ekman depth. The velocity scale $v_{turbulent}$ is estimated as:

$$v_{turbulent} = \frac{\kappa u_{friction}}{\phi_{fluxprofile}(\varsigma_{stability})} \tag{27}$$

where

κ = von Karman's constant, which is equal to 4;

$u_{friction}$ = the friction velocity;

$\phi_{fluxprofile}$ = a non-dimensional flux profile based on the stability of the boundary layer forcing;

$\varsigma_{stability}$ = the stability parameter.

The non-dimensional shape function $s_{shape}(\delta)$ is defined as a third order polynomial

$$s_{shape}(\delta) = c_{coefficient0} + c_{coefficient1}\delta + c_{coefficient2}\delta^2 + c_{coefficient3}\delta^3 \quad (28)$$

where

$c_{coefficient0}$ = 0

$c_{coefficient1}$ = 1

$c_{coefficient2}$ = associated with the viscosity calculated by the interior parameterization ν_{interior} at the boundary layer depth;

$c_{coefficient3}$ = associated with the viscosity calculated by the interior parameterization ν_{interior} at the boundary layer depth

The interior scheme estimates the viscosity coefficient by shear mixing, double-diffusive mixing and internal wave mixing:

$$\nu_{\text{interior}} = \nu_{\text{interior}}^{\text{shear}} + \nu_{\text{interior}}^{\text{double}} + \nu_{\text{interior}}^{\text{wave}} \quad (29)$$

where

$\nu_{\text{interior}}^{\text{shear}}$ = the shear generated mixing;

$\nu_{\text{interior}}^{\text{double}}$ = double diffusive mixing;

$\nu_{\text{interior}}^{\text{wave}}$ = internal wave generated mixing.

The shear generated mixing can be calculated using a gradient Richardson number formulation; the double diffusive mixing are estimated by laboratory and field data.
The internal wave generated mixing, are constants based on experimental data; for example:

For momentum: $\nu_{\text{interior}}^{\text{wave}} = 1.0\times10^{-4} m^2 s^{-1}$

For salinity: $\nu_{\text{interior}}^{\text{wave}} = 1.0\times10^{-5} m^2 s^{-1}$

4.6 Data Collection

In the present project, the basic data include the bathymetry, temperature, wind stress, initial condition of salinity, river discharges, precipitation, heat flux, and desalination capacity. In

order to use MIT general circulation model, all of these data have to be processed and transformed into binary data format. The main objective of this section is to summarize the basic data, their sources and how they are prepared.

4.6.1 Bathymetry

The domain in the simulations is in the Zonal direction and in the Meridional direction. The bathymetry data were drawn from the Scripps Institution of Oceanography, University of California San Diego (Becker *et al.*, 2009). A MATLAB code written for processing the bathymetry data can be found in Appendix 4.

4.6.2 Temperature

Table 4-1. Monthly Averaged Temperature for the period 2005-2060

Month	Temperature (°C)
January	18.6
February	20.3
March	22.7
April	27.4
May	33.4
June	36.5
July	37.5
August	37.2
September	34.7
October	31.2
November	25.6
December	21.1

The data or projection on temperature in the Persian Gulf are obtained using downscaling methods, which are methods to obtain local-scale climate projections from the outputs provided by Global Climate Models (GCMs). Table 4-1 summarized the monthly averaged temperature in the Persian Gulf for the period 2005-2060 obtained by downscaling method (Shirkhani, *et al.*, 2015).

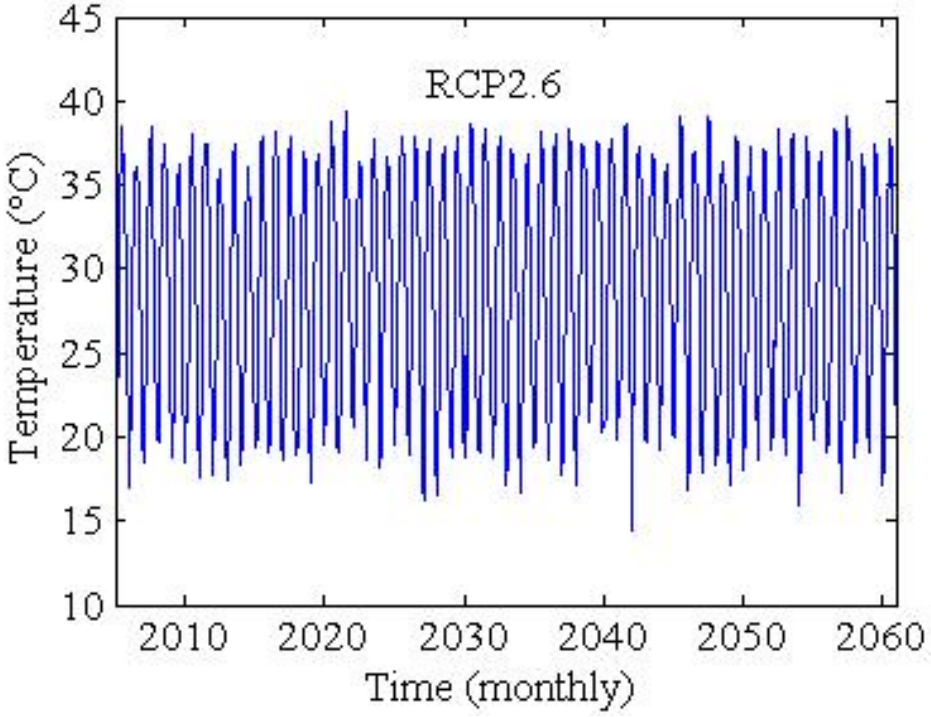

Figure 4-3 (a). Time series of the projections of the temperature in the Persian Gulf corresponding to RCP2.6

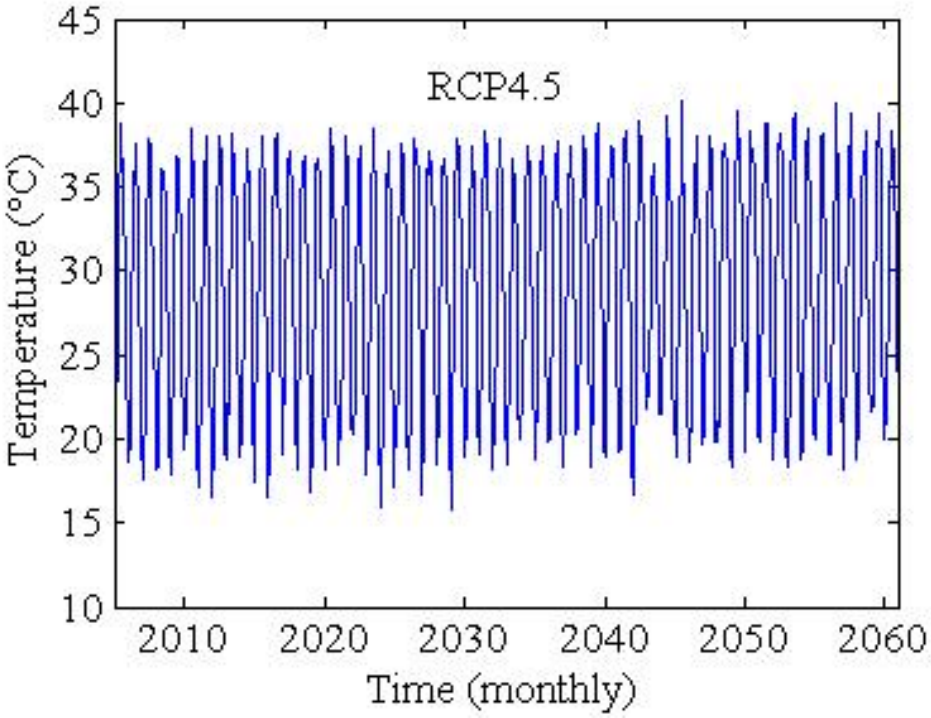

Figure 4-3 (b) Time series of the projections of the temperature in the Persian Gulf corresponding to RCP4.5

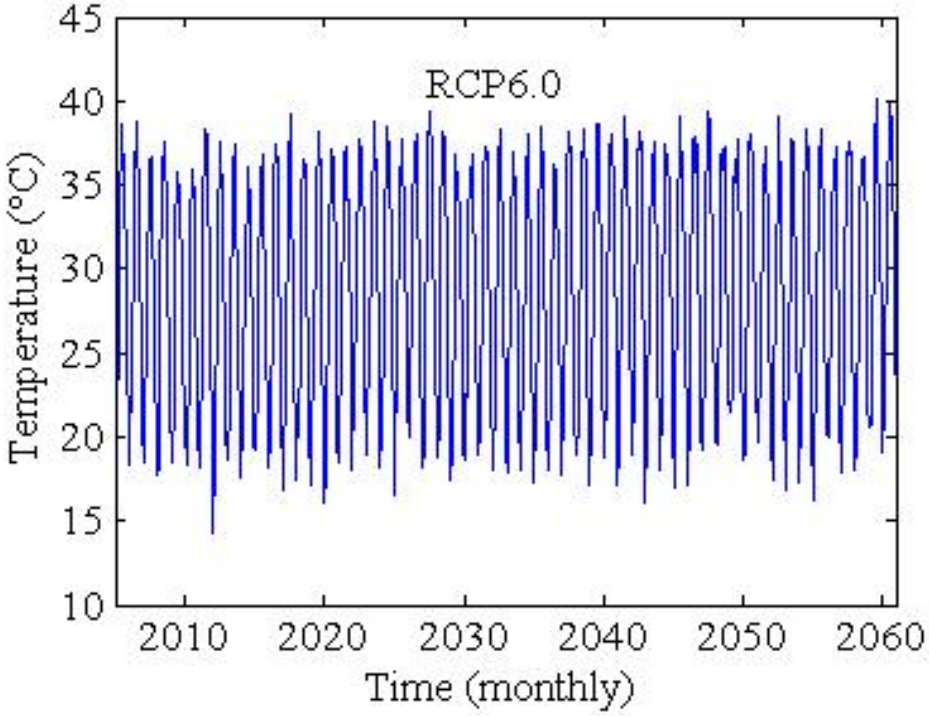

Figure 4-3 (c) Time series of the projections of the temperature in the Persian Gulf corresponding to RCP6.0

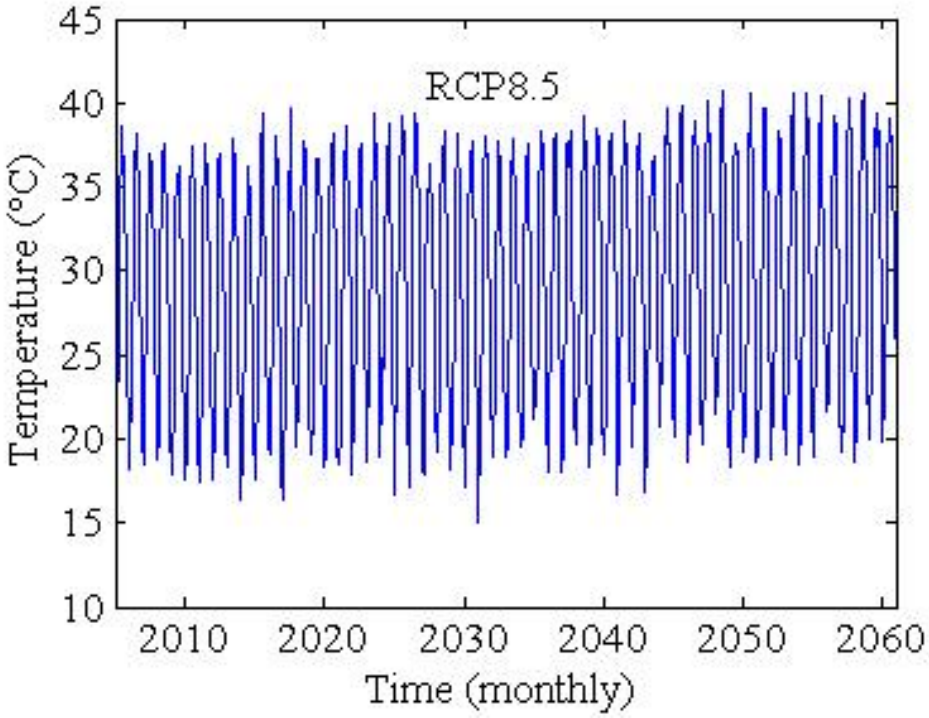

Figure 4-3 (d) Time series of the projections of the temperature in the Persian Gulf corresponding to RCP8.5

Figure 4.3 (a) ~ Figure 4.3 (f) show the time series of the projections of the temperature in the Persian Gulf corresponding to the four Representative Concentration Pathways (PCPs). In the present project, the averaged values of these four sets of data are used. Also, they are transformed into binary data format, like the bathymetry data. The Representative Concentration Pathways and downscaling methods are introduced in details in Appendix 3.

4.6.3 Wind

The data or projection on wind speed in the Persian Gulf are obtained using downscaling methods as well. Table 4-2 summarizes the monthly averaged wind speed in the Persian Gulf for the period 2005-2060 obtained by downscaling method. The averaged values of the obtained data corresponding to four Representative Concentration Pathways (RCPs) are used for the current project.

Table 4-2. Monthly averaged wind speed in the Persian Gulf for the period 2005-2060

Month	Wind Speed (m/s)
January	3.85
February	4.63
March	4.58
April	4.41
May	4.34
June	5.01
July	4.41
August	3.77
September	3.16
October	3.22
November	3.75
December	3.73

A Matlab code was developed for calculating and processing the wind data (Appendix 4). In fact, the wind stress is calculated from the wind speed according to the method proposed by Yelland and Taylor (1996):

$$\tau_{wind} = \rho C_{Drag} U_{wind}^2 \tag{30}$$

$$1000 C_{Drag} = 0.29 + 3.1/U_{wind} + 7.7/\mathrm{U}_{wind}^2 \quad (3 \le U_{wind} \le 6\ m/s) \tag{31}$$

$$1000C_{Drag} = 0.60 + 0.070 * U_{wind} \quad (6 \le U_{wind} \le 26\ m/s) \tag{32}$$

where

τ_{wind} = wind stress;

C_{Drag} = drag Coefficient;

U_{wind} = wind velocity.

4.6.4 Initial Condition of Salinity

Three different studies (Allsop & Yao, 2010; Yao & Johns, 2010; Levitus *et al.*, 2013) are referenced for the initial condition of salinity. The former two studies provide data with high resolution; however, they are not absolutely observational data and the point of time in these two studies does not match the current study perfectly. The latter one provides observational data but the resolution is not high enough. Therefore, in order to obtain an initial condition of salinity with high resolution and reliability, a linear combination of the data in the former two studies is utilized:

$$S_i = \alpha_1 S_A + \alpha_2 S_Y \tag{33}$$

where

S_i = initial condition of salinity;

α_1, α_2 = coefficients;

S_A = salinity by (Allsop & Yao, 2010);

S_Y = salinity by (Levitus *et al.*, 2013).

The initial values of α_1 and α_2 were both set to be 0.5; and they have been calibrated according to the data by (Levitus *et al.*, 2013).

4.6.5 Freshwater Flux, Heat Budget and Desalination Capacity

The study conducted by Privett (1959) is referred for the initial evaporation, and the results from Kappus *et al.* (1978) are used for the precipitation. The main river discharges into the Persian Gulf are obtained from Sadrinasab and Poorkiani (2011). The heat budget is determined according to Chao *et al.* (1992). Data on the capacities of desalination plants are found in Elhakeen and Elshorbagy (2013). Most of these data have already been introduced or shown at length in Chapter 2, so they are not repeated in this section.

4.7 Boundary Conditions

In this section, the kinematic boundary conditions will be introduced first, and then the tidal boundary forcing will be explained.

4.7.1 Kinematic Boundary Conditions

Kinematic boundary conditions consist of vertical condition and horizontal condition (Adcroft *et al.*, 2008):

Vertical kinematic boundary condition:

$$w = 0 \text{ at ocean bottom} \tag{34}$$

$$w = \frac{Dz}{Dt} \quad \text{at } z = R_{moving} \tag{35}$$

$$R_{moving} = R_0 + \eta \tag{36}$$

where

w = vertical velocity;

z = vertical coordinate;

R_{moving} = ocean surface;

R_0 = surface in the resting fluid;

η = departure from R_0 in the presence of motion.

Horizontal kinematic boundary condition:

$$\vec{v} \cdot \vec{n} = 0 \tag{37}$$

where

$\vec{v}$ = velocity;

$\vec{n}$ = the normal to a solid boundary.

4.7.2 Tidal Boundary Forcing

Tidal boundary forcing is considered using the four major tidal constituents M_2, S_2, O_1, and K_1 (Badri & Wilders, 2010). The periods and wave numbers of the main constituents have already been listed in Table 2-1.

4.8 Model Setup

In the present study, the spherical polar coordinate system is employed since it is more natural for describing positions on a sphere than other coordinate systems (described with more details in Appendix 3). There is no universally accepted standard for the selection of the grid size in MITgcm modeling, as the model can be applied to a wide range of phenomena. The simulation was first constructed using $0.01° \times 0.01°$ grids, and then coarser grid sizes were tested. Finally, a grid resolution of $0.05° \times 0.05°$ is selected in the present case, and the Kriging interpolation approach is utilized to obtain detailed predictions. This configuration can produce almost the same results but requires less than 10% of the computational cost as the configuration with $0.01° \times 0.01°$ grids.

The time step is selected to be 180 s, predominantly based on the Courant stability condition and the requirements of our analysis. The case was once simulated with a time step of 90 s, and it was observed that the decrease in time step does not have an evident effect on the predicted salinity distribution.

The hydrostatic assumption is adopted in the simulations, since the Persian Gulf meets the condition of shallow water, as introduced in Chapter 2. Specifically, the average depth of Persian the Gulf is only 50 meters, suggesting that the shallow layers are of primary interest. Owing to this shallow nature of the Persian Gulf, the water column is hence divided into ten layers in the vertical direction with increasing thicknesses from surface to bottom: 5 m, 8.45 m, 14.27 m, 24.11 m, 40.73 m, 68.8 m, 116.23m, 196.35 m, 331.71 m, and 560.37 m (A MATLAB code for determining this vertical configuration has been shown in Appendix 4). The nonlocal K-Profile parameterization (to determine vertical viscous and diffusive

coefficients) proposed by Large *et al.* (1994) is used in the present thesis, since it has been widely used in open ocean settings.

4.9 Conclusion

In this chapter, the numerical model, governing equations, discretization methods and some widely used numerical algorithms, mixing parameterization have been summarized; data preparation, boundary conditions and model setup have also been described. Using this methodology, we have conducted two studies (or two stages of one study): one is to examine the performance of various schemes in simulating the salinity distribution in a large-scale inverse estuary, and another one is to numerically predict the long-term balance of salinity in the Persian Gulf.

In the next chapter, the study of numerical modeling of salinity distribution in a large-scale inverse estuary will be presented.

Chapter 5 Numerical Modeling of Salinity Distribution in a Large-scale Inverse Estuary

Abstract This chapter will mainly present the study of numerical modeling of salinity distribution in a large-scale inverse estuary. The salinity distribution in the Persian Gulf will be simulated with 8 different schemes (combinations of equations of state, momentum methods and advection algorithms), and the obtained results will be compared with the World Ocean Atlas 2013 (WOA13) data. The comparisons can validate the utility of a numerical model in the prediction of salinity distribution in a large-scale inverse estuary. The most appropriate scheme for this case will be figured out, and this validated scheme can also be used for the further study with respect to the long-term balance of salinity in the Persian Gulf, which will be presented in Chapter 6.

5.1 Equation of State

5.1.1 Introduction

The equation of state (EOS) used in ocean or estuarine models is a function to determine the density of seawater, depending on salinity, temperature (or potential temperature), and pressure. It has to be implemented in almost any ocean or estuarine model, and even a small deficit in it can produce a significant impact on the simulation results (Thoma *et al.*, 2010).

The study of EOS has attracted a great amount of attention and has led to a vast collection of various approaches. However, only three widely accepted methods (International, JMcD, and MJWF03 equations) are focused on in this study; the history of the EOS for seawater is reviewed in detail elsewhere by Millero (2010).

5.1.2 International Equation of State.

An approach widely employed in the oceanographic community is the International Equation of State (EOS-80, Fofonoff and Millard, 1983), which is also called the "UNESCO" Equation of State (Post, 2012). The International Equation of State can be expressed in the form:

$$\rho = \rho(S, \mathrm{T}, p)\,, \tag{38}$$

where

ρ = density;

S = salinity;

T = temperature;

p = pressure;

The density of seawater can be calculated as:

$$\rho(\mathrm{S},\mathrm{T},\mathrm{p}) = \rho(\mathrm{S},\mathrm{T},0) / \left[1 - p / K(S,\mathrm{T},p)\right] \tag{39}$$

where

$\rho(\mathrm{S},\mathrm{T},0)$ = the density at the surface, which can be determined by a set of 15 coefficients;

$K(S,\mathrm{T},p)$ = the secant bulk modulus, which can be calculated by 26 coefficients.

5.1.3 JMcD Equation of State.

The temperature of a volume of water moving from one pressure to another will increase or decrease because it is compressed or expanded respectively (Stillinger and Rahman, 1974). However, the temperature change caused solely by compression or expansion is not of interest to the evaluation of some variables in oceanic or estuarine numerical models (e.g., thermal expansion and saline contraction coefficients), and hence the effects of the pressure on temperature are normally removed by replacing the in situ temperature with the potential temperature, which is the temperature a parcel of water would have if it was moved adiabatically to a reference pressure (Bolton, 1980). In other words, the intrinsic variable in most of the models is potential temperature rather than in situ temperature. Therefore, the use of the International Equation of State requires the time-consuming conversion between the potential temperature and the in situ temperature (Jackett and Mcdougall, 1995). Jackett and Mcdougall (1995) proposed an equation of state in terms of potential temperature rather than in situ temperature so that the density can be determined directly from the potential temperature. As the difference between the potential and in situ temperatures is usually very small, the functional form of the International Equation of State is retained:

$$\rho(S,\theta,\mathrm{p}) = \frac{\rho(S,\theta,0)}{1 - p / K(S,\theta,\mathrm{p})} \tag{40}$$

where

θ = the potential temperature.

Apart from the temperature variable, it has the same terms as the International Equation of State, but the 41 coefficients have been modified. This equation of state can be referred to as the "JMcD" Equation of State (Sun *et al.*, 1999).

5.1.4 MJWF03 Equation of State

McDougall *et al.* (2003) developed another equation of state that used potential temperature instead of in situ temperature, and it can be named the "MJWF03 Equation of State" (Jackett *et al.*, 2006).

Feistel and Hagen (1995) proposed an equation of state based on a Gibbs thermodynamic potential which is more accurate than the International Equation of State but is too computationally demanding. In order to improve the computational efficiency, McDougall *et al.* (2003) used the rational function approach by Wright (1997) with more terms considered.

The MJWF03 Equation of State is in the form:

$$\rho(S,\theta,\mathrm{p}) = \frac{P_1(S,\theta,\mathrm{p})}{P_2(S,\theta,\mathrm{p})} \tag{41}$$

where

$P_1(S,\theta,\mathrm{p})$ = is a polynomial with 12 terms;

$P_2(S,\theta,\mathrm{p})$ = a polynomial can be obtained by 13 terms.

5.2 Numerical Algorithms

The present study examines various combinations of numerical algorithms. In terms of methods for dealing with the free surface in the momentum equations, the rigid-lid method and implicit free surface method are investigated. In terms of algorithms for tracer equations, two

widely-used approaches, Adams-Bashforth approach and Lax- Wendroff approach, are compared. These algorithms have already been explained in Chapter 4.

For the purpose of comparing various alternatives, these numerical algorithms are combined with the equations of state, and these combinations are referred to as “schemes”. The equation of state, momentum method, and advection algorithm adopted in each scheme are summarized in Table 5-1. The sequence of these schemes has been tentatively manipulated for convenience of analysis. The purpose of the present study is to obtain some general conclusions about the suitability of different schemes, so the internal default parameters are not calibrated or compared.

Table 5-1. Equation of state, momentum method, and advection algorithm for each scheme

Scheme*	EOS	Momentum Method	Advection Algorithm
S1	JMcD	Implicit Free Surface	Adams-Bashforth
S2	MJWF03	Implicit Free Surface	Adams-Bashforth
S3	JMcD	Rigid-Lid	Adams-Bashforth
S4	JMcD	Implicit Free Surface	Lax-Wendroff
S5	JMcD	Rigid-Lid	Lax-Wendroff
S6	MJWF03	Implicit Free Surface	Lax-Wendroff
S7	MJWF03	Rigid-Lid	Adams-Bashforth
S8	MJWF03	Rigid-Lid	Lax-Wendroff

***. “S” represents “Scheme”**

5.3 Surface Salinity at Representative Locations

Due primarily to the large-scale nature of the Persian Gulf, it is quite difficult to show a detailed analysis of the salinity variation at all numerical grids. An approach of analyzing the

salinity variation at a number of representative locations can provide somewhat sufficient information on the salinity distribution in a large-scale case.

Thus, six locations distributed over different regions of the Persian Gulf are chosen as representative stations, and their latitudes and longitudes are shown in Table 5-2.

Table 5-2. The latitudes and longitudes of the representative locations

	L1*	L2	L3	L4	L5	L6
Latitude	24.625	25.875	26.375	27.125	28.625	29.625
Longitude	53.625	53.375	53.375	50.875	48.875	49.125

***. L represents "Location"**

The World Ocean Atlas 2013 (WOA13, 2013), produced by NOAA's National Oceanographic Data Center, provides a long-timespan set of climatology and salinity data for the world's oceans. It has a 0.25 degree horizontal resolution version for annual and seasonal salinity for six decades, and monthly data for decadal averages. The simulated 3-minute time-step results in this study are interpolated and averaged for comparison with the WOA13 data (for the study domain). In Figure 5-1(a) ~ Figure 5-1 (f), we show the WOA13 and simulated monthly averaged surface salinity for the period 2005-2012 obtained by various combinations (hereinafter referred to as "schemes") of equations of state, momentum methods, and advection algorithms at the six representative locations. This specific period is selected because it has a high data quality. With Figure 5-1 (a) ~ Figure 5-1 (f), it is easy to roughly measure or estimate the performance of each scheme. It can be noticed that the model follows closely the drop and rise of surface salinity with time at the representative stations, but most of the modeled results exhibit lower salinity relative to the observed data, as the simulations have neglected small desalination plants, some biogeochemical processes, and irregular wind bursts. Note that in Figure 5-1 (e) and (f), some modelled results obtained from certain schemes deviate greatly from the measurements, especially in June. Note that Location 5 and Location 6, corresponding to Figure 5-1 (e) and (f) respectively, are located at relative high latitudes. In June, there is a sharp change in surface salinity.

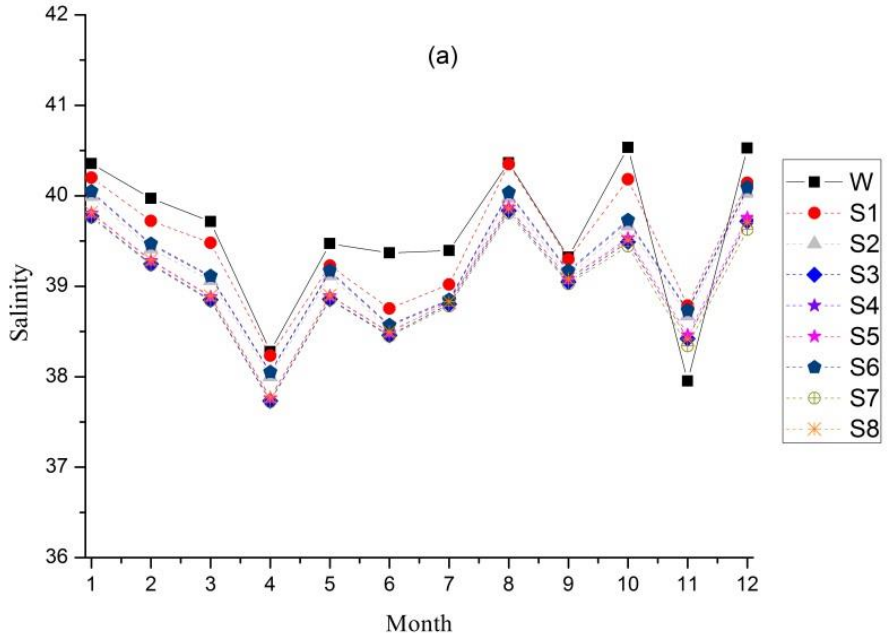

Figure 5-1 (a). WOA13 and simulated monthly averaged surface salinity at Location 1 using eight schemes (S1 to S8) for the period 2005-2012. "W" represents "WOA13"; "S" represents "Scheme"

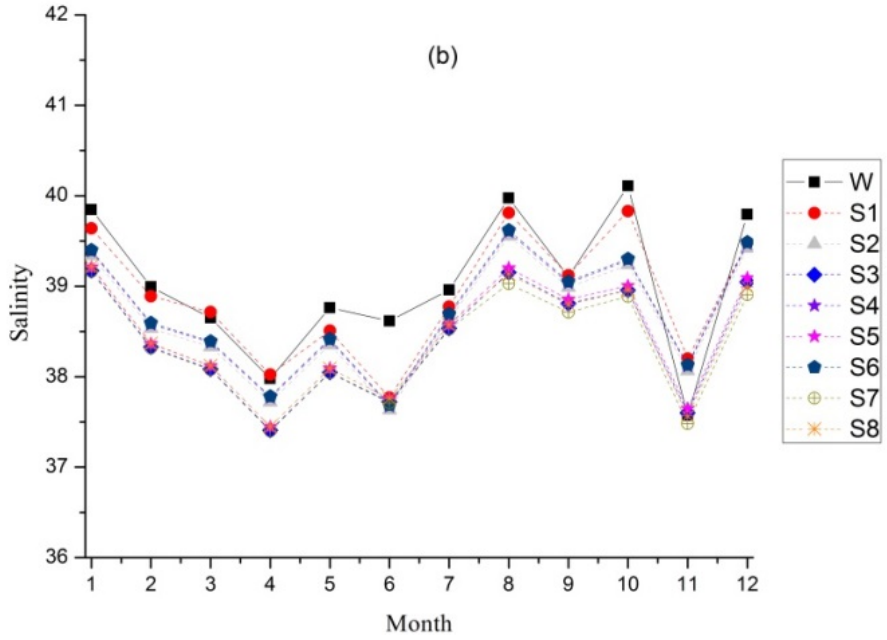

Figure 5-1 (b). WOA13 and simulated monthly averaged surface salinity at Location 2 using eight schemes (S1 to S8) for the period 2005-2012. "W" represents "WOA13"; "S" represents "Scheme"

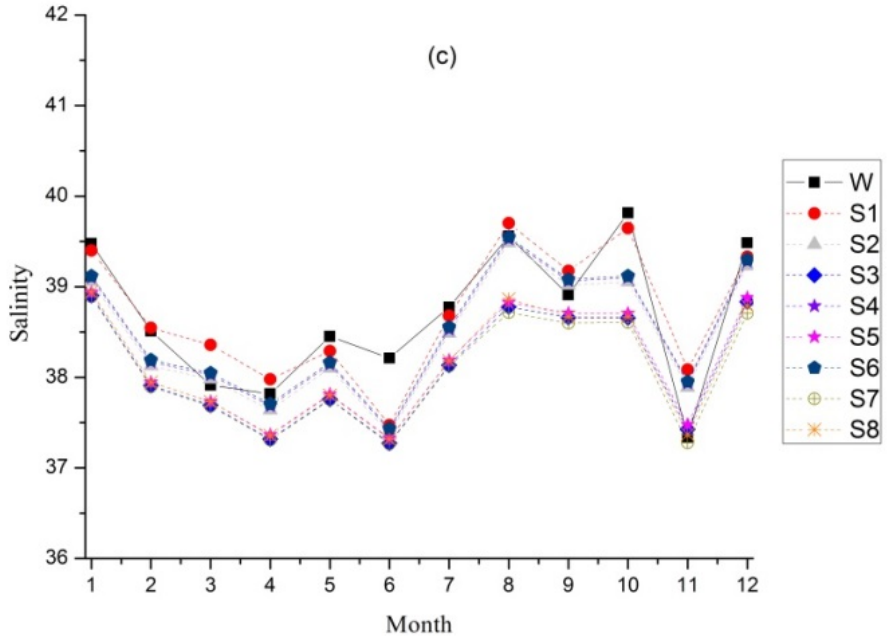

Figure 5-1 (c). WOA13 and simulated monthly averaged surface salinity at Location 3 using eight schemes (S1 to S8) for the period 2005-2012. "W" represents "WOA13"; "S" represents "Scheme"

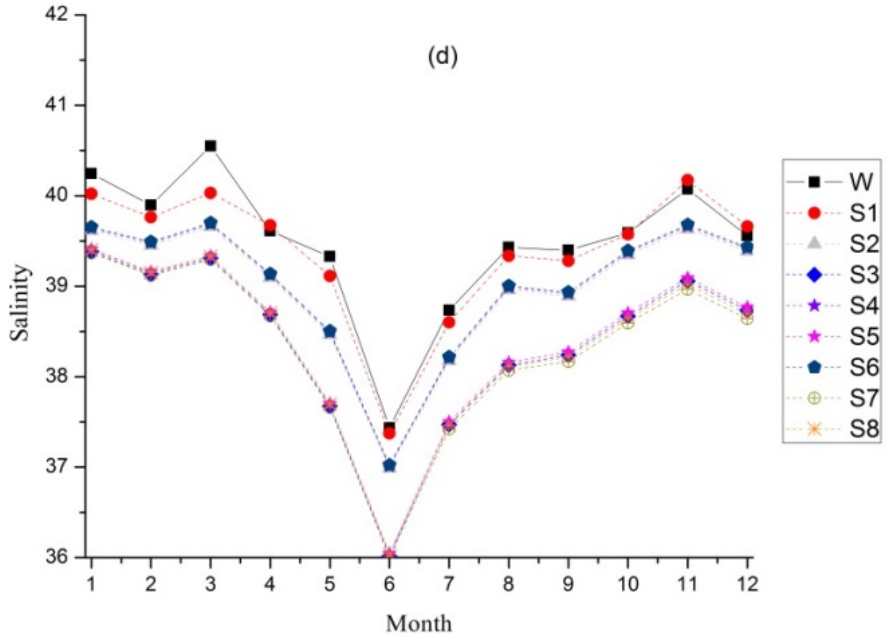

Figure 5-1 (d). WOA13 and simulated monthly averaged surface salinity at Location 4 using eight schemes (S1 to S8) for the period 2005-2012. "W" represents "WOA13"; "S" represents "Scheme"

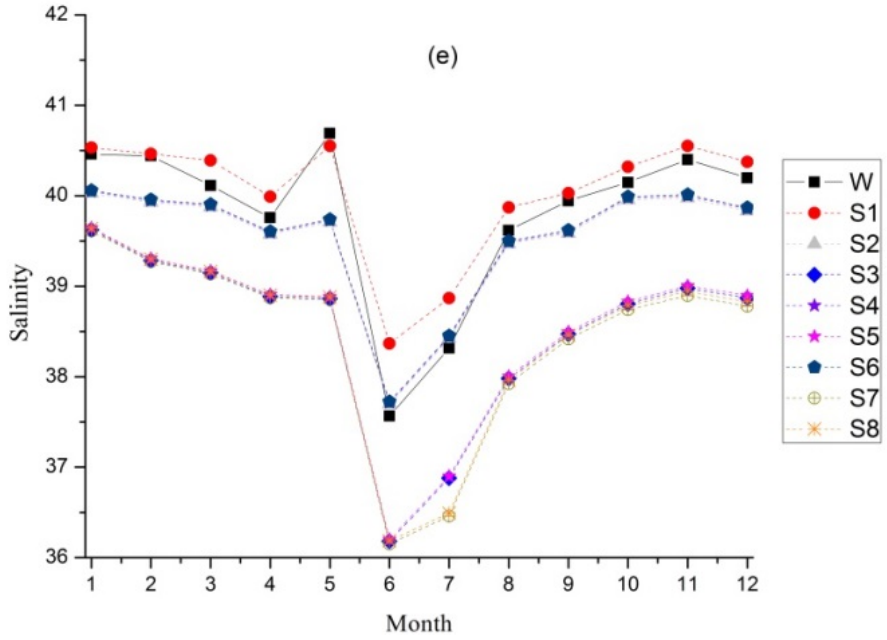

Figure 5-1 (e). WOA13 and simulated monthly averaged surface salinity at Location 5 using eight schemes (S1 to S8) for the period 2005-2012. "W" represents "WOA13"; "S" represents "Scheme"

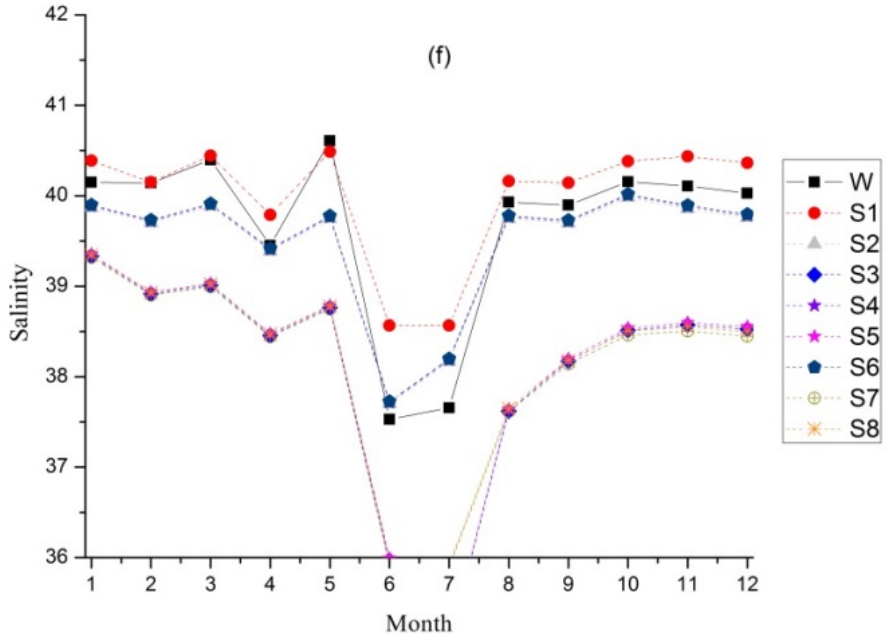

Figure 5-1 (f). WOA13 and simulated monthly averaged surface salinity at Location 6 using eight schemes (S1 to S8) for the period 2005-2012. "W" represents "WOA13"; "S" represents "Scheme"

Therefore, it can be reasonable to conclude that some schemes perform relatively poorly for surface salinity, especially at the high-latitude region of the Gulf where the salinity has a sharp change

For a further examination and explanation of these observations, quantitative analyses are conducted. The basic approach for obtaining a quantitative proxy of the performance of the various schemes is to compare the root mean square errors (RMSDs), which are discussed in more details in 0. Hence, the RMSDs at the representative locations for each scheme are calculated and summarized in Table 5-3.

Table 5-3. RMSDs for surface salinity at the representative locations

Scheme**	L1*	L2	L3	L4	L5	L6
S1	0.3752	0.3498	0.3546	0.1938	0.3246	0.4545
S2	0.5684	0.5175	0.4313	0.5526	0.4116	0.3881
S3	0.6941	0.6885	0.6583	1.1419	1.3373	1.6658
S4	0.5368	0.4855	0.4094	0.5281	0.3973	0.3778
S5	0.6658	0.6507	0.6177	1.1140	1.3147	1.6438
S6	0.5281	0.4742	0.3998	0.5140	0.3884	0.3714
S7	0.7148	0.7339	0.6902	1.1841	1.4171	1.6009
S8	0.6682	0.6743	0.6306	1.1428	1.3815	1.5669

***. "L" represents "Location"**

****. "S" represents "Scheme"**

The smallest RMSDs from Location 1 to Location 6 are 0.3752, 0.3498, 0.3546, 0.1938, 0.3246, and 0.3714 psu (practical salinity unit), respectively. Note that except for the sixth location, all the results with smallest RMSDs are achieved by the first scheme, implying that Scheme 1 is probably the most appropriate one for this case. The RMSDs obtained by Scheme

3, Scheme 5, Scheme 7, and Scheme 8 are measurably higher than the others, and it needs to be noted here that all of these four schemes have employed the rigid-lid approximation, suggesting that the results from the rigid-lid method are less accurate than those from the implicit free surface method. A possible reason for the relatively poor performance of the rigid-lid approximation for this case is that the approximation excludes the free freshwater flux.

The schemes are divided into four pairs to preliminarily judge the impact of the equations of state on the results. On average, Scheme 1 is better than Scheme 2, Scheme 3 is better than Scheme 7, Scheme 4 is worse than Scheme 6, and Scheme 5 is better than Scheme 8. These results might indicate that in this situation the JMcD Equation of State has an advantage over the MJWF03 Equation of State in terms of accuracy, even though JMcD Equation of State is the older one.

The differences between the results provided by Scheme 3 and Scheme 7, as well as Scheme 5 and Scheme 8 are somewhat smaller, from which we can observe the impacts of the equations of state on the results, which also depend on the method used for the free surface in the momentum equation. More specifically, the equation of state would have a smaller impact on the accuracy of simulated results when combined with the rigid-lid approximation. The mechanism for this is that the effect of one factor in a system on the errors might be offset or magnified by other effects. Moreover, this phenomenon can also be explained and quantified by the path analysis method (discussed in detail in 0) developed by Wright (1921), where the independent variables have both direct and indirect (through other variables) effects on the dependent variables. For example, the equation of state has both a direct effect and an indirect (through the momentum method and advection algorithm) effect on the accuracy of the results, and in total, the overall effect is the summation of these direct and indirect effects.

Likewise, we compared the advection algorithms in a similar way. The Lax-Wendroff method seems to be slightly better than the Adams-Bashforth method for this case, but the situation turns out to be inversed when JMcD Equation of State and rigid-lid method are being used. A reason for this occurrence is that the equations are solved or modeled sequentially rather than separately in numerical simulations, so the effect of one algorithm can be influenced by another, in accordance with the reasons explained earlier.

The computational costs are also considered in the present study. It can be summarized that the MJWF03 Equation of State, the rigid-lid momentum method, and the Adams-Bashforth advection algorithm can result in a reduction in computational cost. Actually, Scheme 7 can save as much as about 15% of Scheme 4. However, computational efficiency will not be regarded as the primary concern in this case, since the effects of different schemes will greatly change the results.

5.4 Surface Salinity at Various Latitudes

The outputs as well as the conclusions drawn in the preceding section are examined further by analyzing surface salinity at various latitudes.

For the purpose of obtaining a quantitative measure of the difference between the WOA13 data and simulations, scatter plots of WOA13 data versus simulated annual mean surface salinity at various latitudes for the period 2005-2012 are made in Figure 5-2 (a) ~ Figure 5-2 (e). Owing to the reasons stated in the last section, the model tends to under-predict the surface salinity in the Gulf, especially at relatively high latitudes, based on the fact that few symbols appear above the line of agreement.

Figure 5-2 (a) ~ Figure 5-2 (d) show a good match between WOA13 and simulated surface salinity using Scheme 1, in agreement with the conclusions drawn from the six representative locations. As expected, some schemes predict unsatisfactorily in the surface salinity, especially at relative high latitudes (e.g. Latitude 4), which demonstrates the statement made in the previous section.

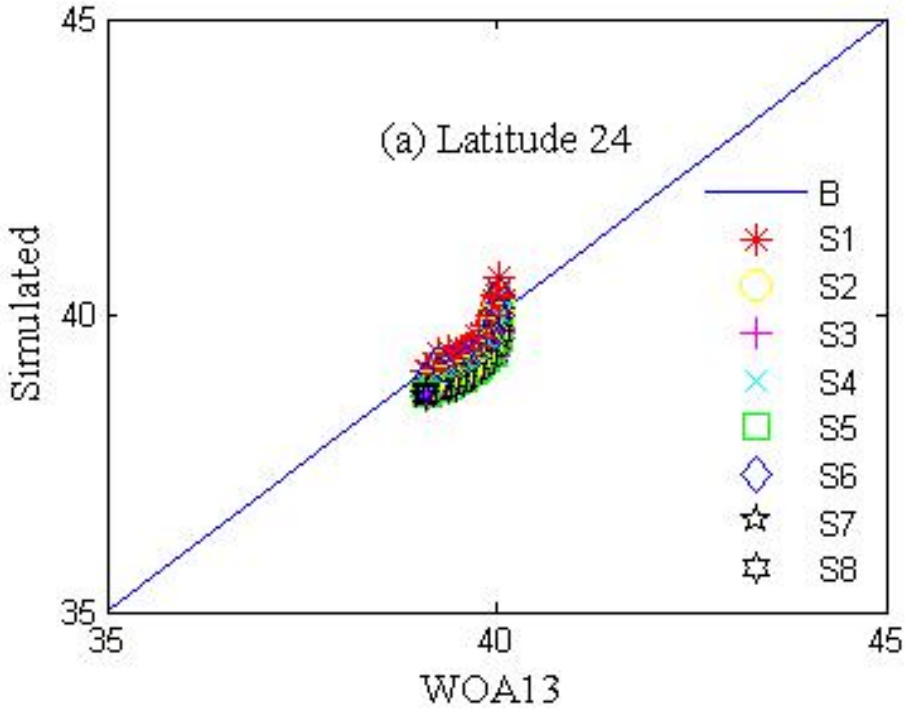

Figure 5-2 (a). Scatter plots of the WOA13 versus simulated annual mean surface salinity at Latitude 24°~25° using various schemes for the period 2005-2012. "B" is "Bisector"; "S" represents "Scheme".

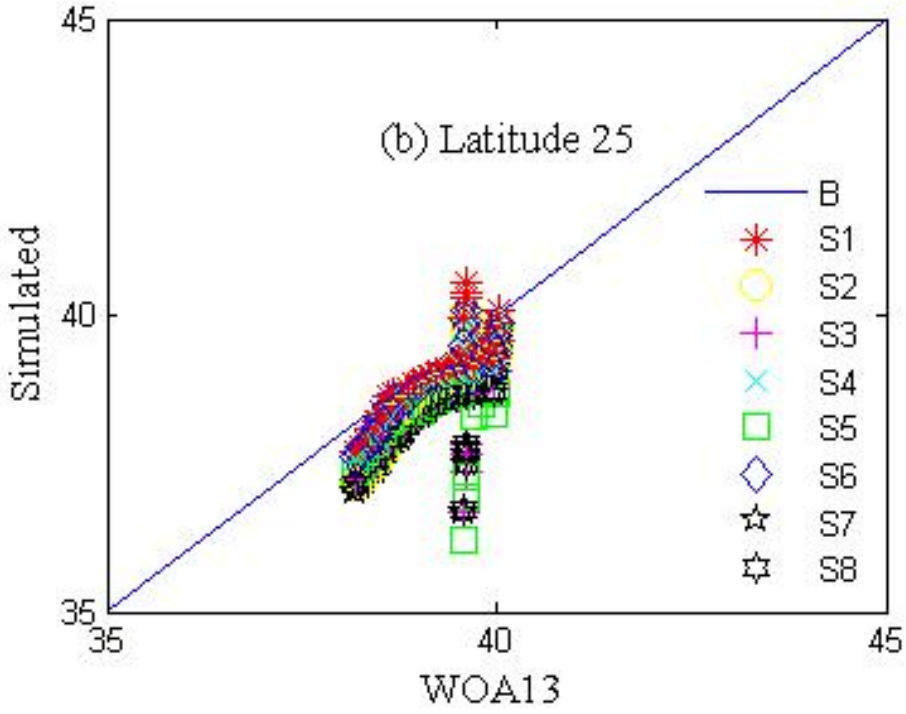

Figure 5-2 (b). Scatter plots of the WOA13 versus simulated annual mean surface salinity at Latitude 25°~26° using various schemes for the period 2005-2012. "B" is "Bisector"; "S" represents "Scheme".

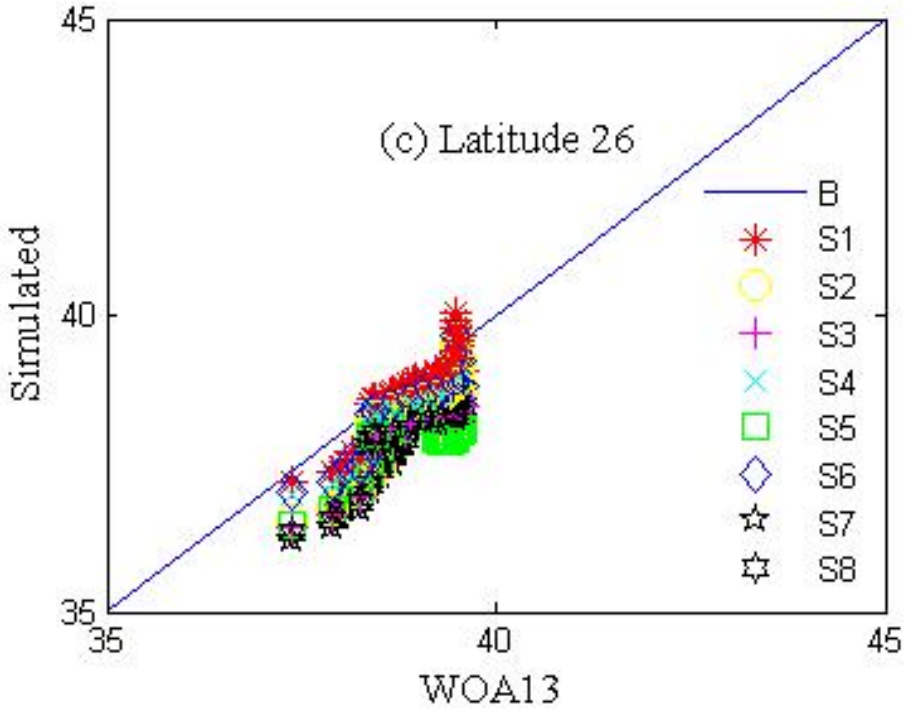

Figure 5-2 (c). Scatter plots of the WOA13 versus simulated annual mean surface salinity at Latitude 26°~27° using various schemes for the period 2005-2012. "B" is "Bisector"; "S" represents "Scheme".

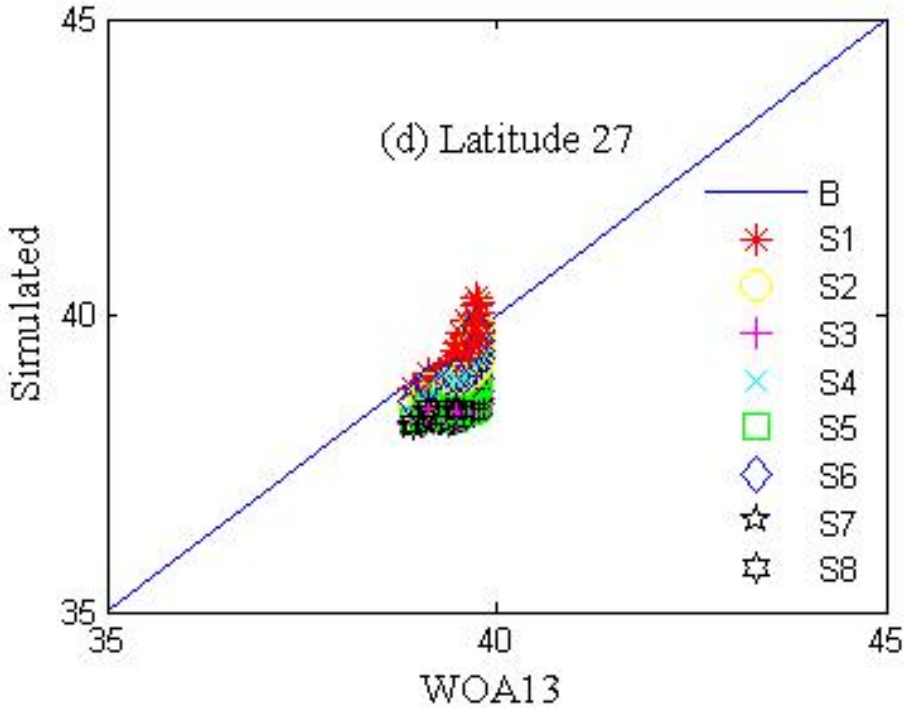

Figure 5-2 (d). Scatter plots of the WOA13 versus simulated annual mean surface salinity at Latitude 27°~28° using various schemes for the period 2005-2012. "B" is "Bisector"; "S" represents "Scheme".

To obtain more details, the RMSD values at various latitudes for surface salinity are calculated (in Table 5-4). It can be noticed that all of the lowest errors are obtained from Scheme 1, confirming that Scheme 1 is definitely the best scheme in terms of accuracy. Schemes with rigid-lid approximation (Scheme 3, 5, 7, 8) predict clearly worse results than others in the surface salinity, which confirms again the conclusion drawn from the analysis of surface salinity at the six representative locations. The large differences in predicted salinity by implicit free surface approach and rigid-lid approach highlight the limitation of the rigid-lid approach in including the free freshwater flux.

The RMSD for rigid-lid approach can be about 4 times larger than the implicit free surface method, which means that the benefits of saving computational time cannot make up the lower accuracy.

The schemes are grouped and compared in the same way as described in Section 4.1. According to the results, the JMcD Equation of State does not show a very obvious advantage over the MJWF03 Equation of State; but when coupled with implicit free surface and Adams-Bashforth method, the advantage becomes quite significant. Similarly, when combined with JMcD Equation of State and Implicit Free Surface, the Adams-Bashforth predicts better than Lax-Wendroff method.

Table 5-4. RMSD at various latitudes for surface salinity

Scheme**	LT1*	LT2	LT3	LT4	LT5
S1	0.2096	0.3395	0.2969	0.2697	0.4251
S2	0.3427	0.5873	0.6017	0.5166	0.6802
S3	0.5295	0.8890	0.8860	1.0791	1.4469
S4	0.3051	0.4533	0.4746	0.4888	0.6589
S5	0.4997	0.9765	1.0552	1.0475	1.4209
S6	0.2949	0.4385	0.4580	0.4724	0.6461
S7	0.5594	0.9479	0.9910	1.1164	1.4888
S8	0.5069	0.8899	0.9246	1.0746	1.4514

***. "LT" represents "Latitude"**

****. "S" represents "Scheme"**

Overall, the characteristics concluded by analyzing the surface salinity at various latitudes match correctly with those obtained by inspecting the representative locations. This fact confirms the conclusions drawn in the preceding section and justifies the utilization of the six stations as representative of the domain. Therefore, we will use these six representative locations again for the examination of the sub-surface salinity in the Persian Gulf, which will be presented in the next section. Besides, the comparisons demonstrate that the current numerical model with Scheme 1 performs better than the models employed in some previous studies, e.g. Hassanzadeh *et al.* (2011; Figure 5-3).

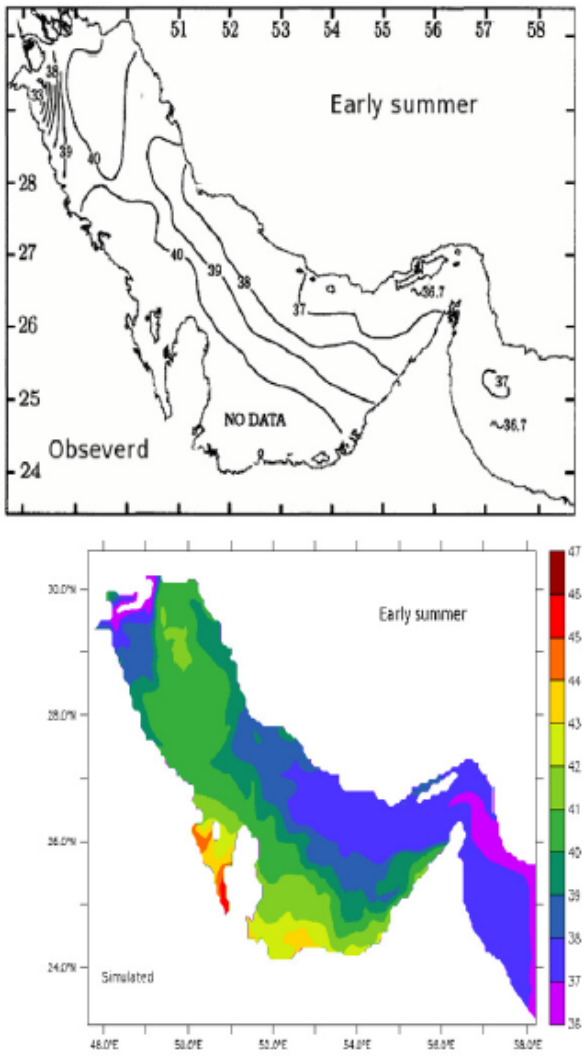

Figure 5-3. Comparison between the simulated salinity and observed salinity in early summer at the water surface Hassanzadeh et al. (2011)

5.5 Sub-surface Salinity at Representative Locations

The six representative stations have been validated in the last section, so they are employed as well for the investigation of sub-surface salinity in the Persian Gulf.

The WOA13 reported time variation of the sub-surface salinity at 5 m depth, and the data for the representative stations are compared with the simulated results, as shown in Figure 5-4 (a) ~ Figure 5-4 (f).

In light of the comparisons plotted, we notice that the results predicted by the different schemes are close. The figures (e.g., Figure 5) show that a very good match between data and

simulations is obtained, and that Scheme 1 is the most accurate. A possible reason for this is that the model is more capable in predicting smooth variation of salinity; basically, there are more sharp changes in the surface salinity, while the variation is much smoother in the sub-surface salinity. This can also explain the phenomenon that the model matches closely with the data in Figure 5-4 (a), (b), (c), and (d) but deviates farther in Figure 5-4 (e) and (f), where there are several sudden large variations. The advantage of Scheme 1 over the other schemes is not as evident as that for the surface salinity, probably because Scheme 1 is more competent in terms of the instantaneous surface variation. The model cannot exactly predict the small trends of variation, as the sub-surface salinity is also influenced by many different factors, such as biochemical processes, but for the overall trend, the model exhibits an excellent capability.

The RMSDs for sub-surface salinity at the representative locations are summarized in Table 5-5. Overall, Scheme 1 is the most appropriate for this case, similar to the expectations for surface salinity. It can also be observed that the results provided by the schemes with the implicit free surface approach exhibit an excellent match with the data. For simulations by the schemes with rigid-lid approximations, the match is also good, with a slightly higher RMSD value. Besides, the RMSDs are relatively higher at Location 5 and Location 6, mainly because of the sharp changes, as explained above.

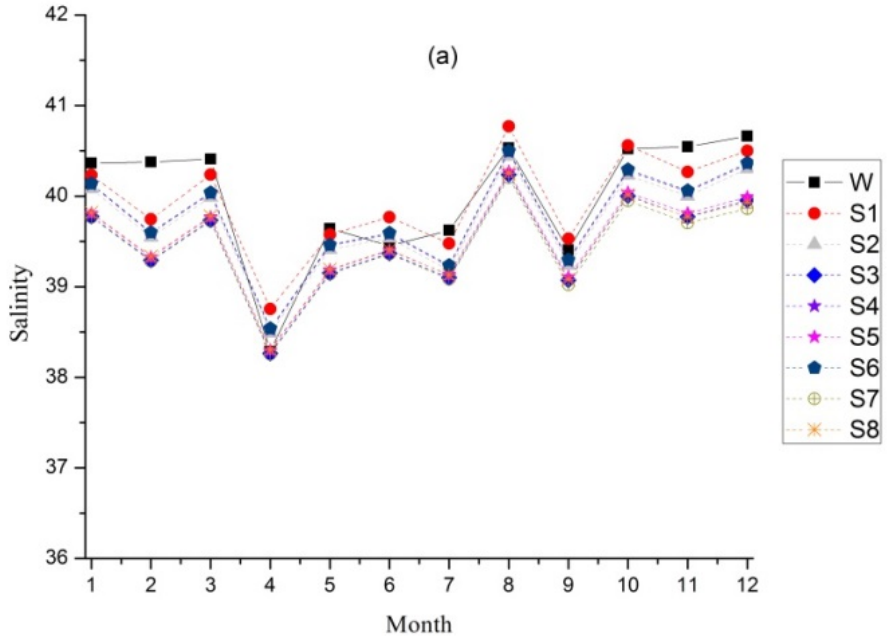

Figure 5-4 (a). WOA13 and simulated monthly averaged sub-surface salinity at Location 1 using various schemes for the period of 2005-2012. "W" represents "WOA13"; "S" represents "Salinity"

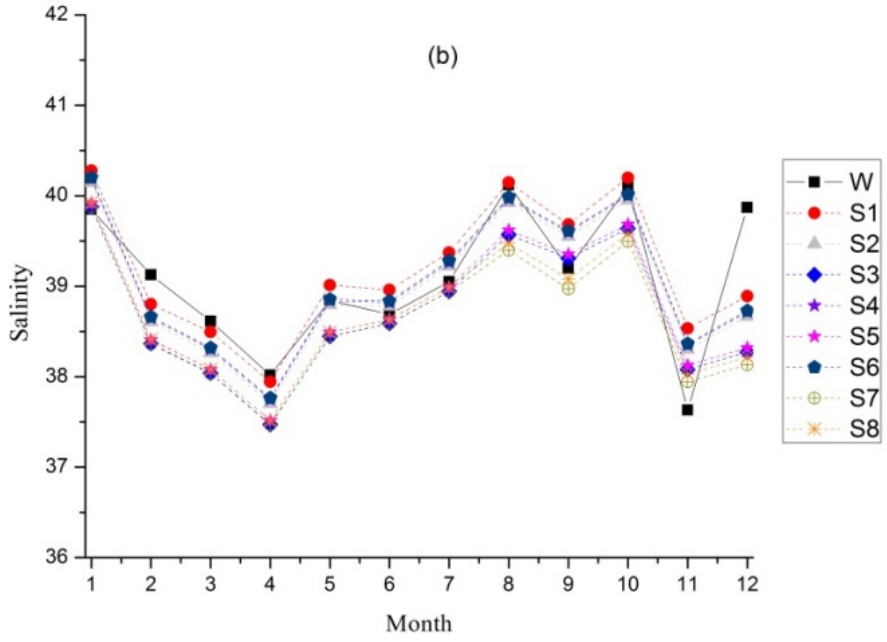

Figure 5-4 (b). WOA13 and simulated monthly averaged sub-surface salinity at Location 2 using various schemes for the period of 2005-2012. "W" represents "WOA13"; "S" represents "Salinity"

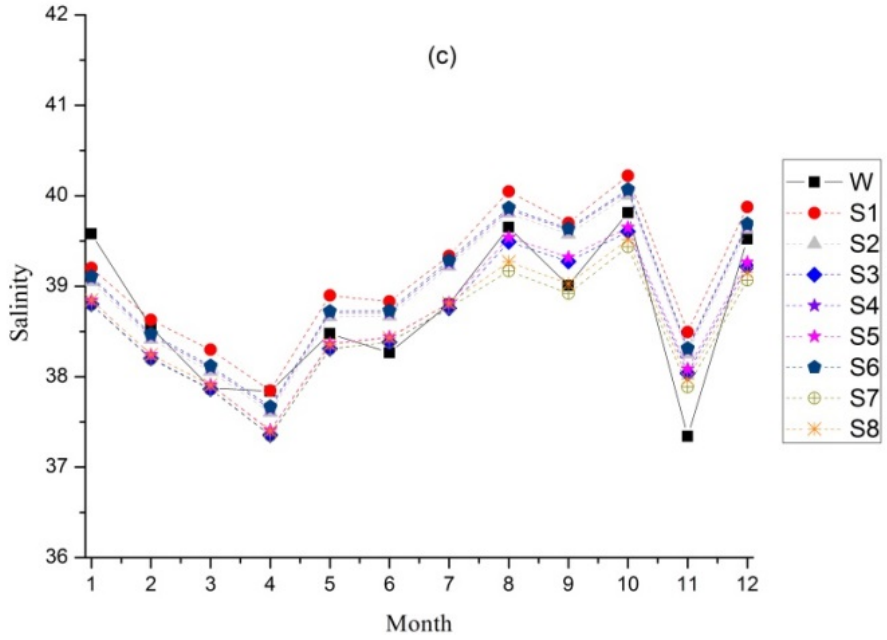

Figure 5-4 (c). WOA13 and simulated monthly averaged sub-surface salinity at Location 3 using various schemes for the period of 2005-2012. "W" represents "WOA13"; "S" represents "Salinity"

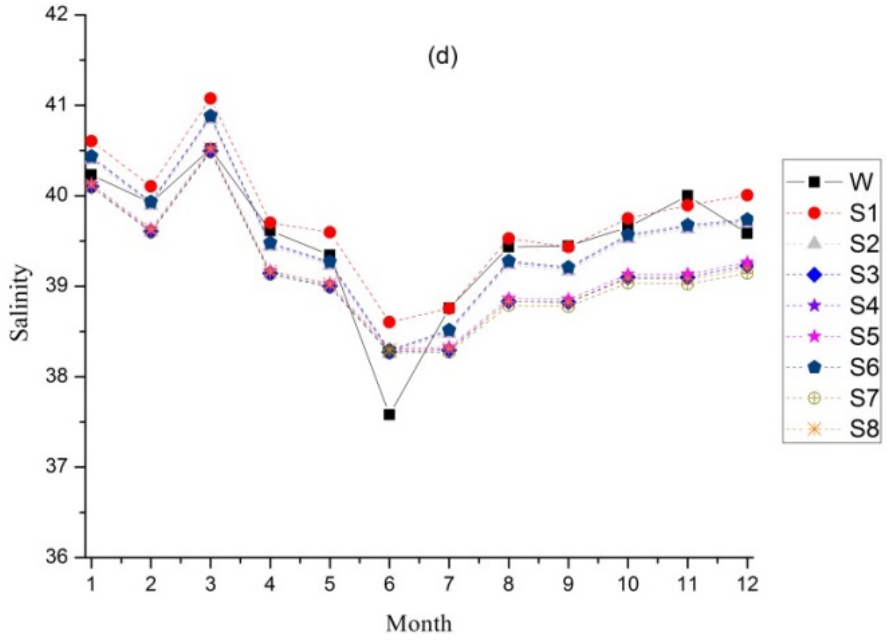

Figure 5-4 (d). WOA13 and simulated monthly averaged sub-surface salinity at Location 4 using various schemes for the period of 2005-2012. "W" represents "WOA13"; "S" represents "Salinity

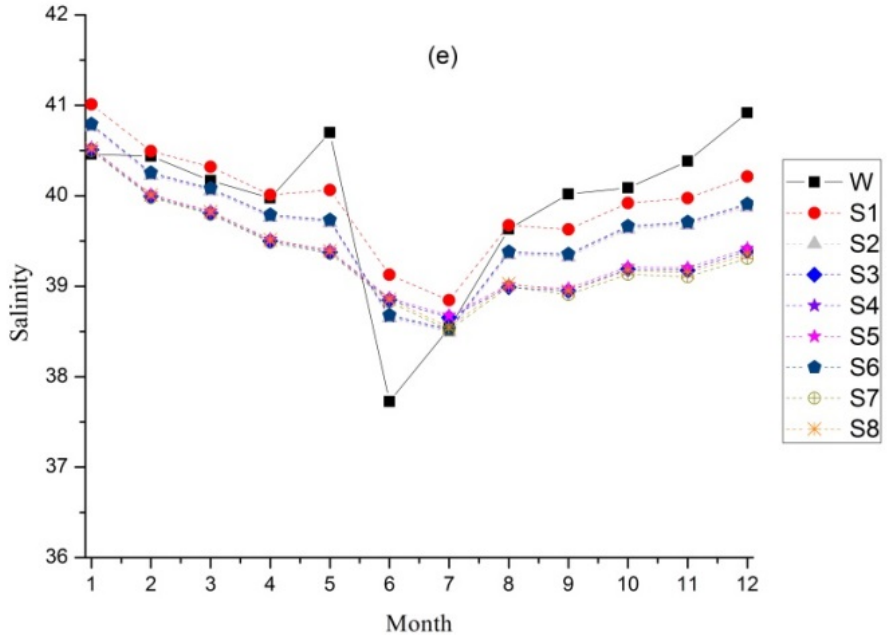

Figure 5-4 (e). WOA13 and simulated monthly averaged sub-surface salinity at Location 5 using various schemes for the period of 2005-2012. "W" represents "WOA13"; "S" represents "Salinity"

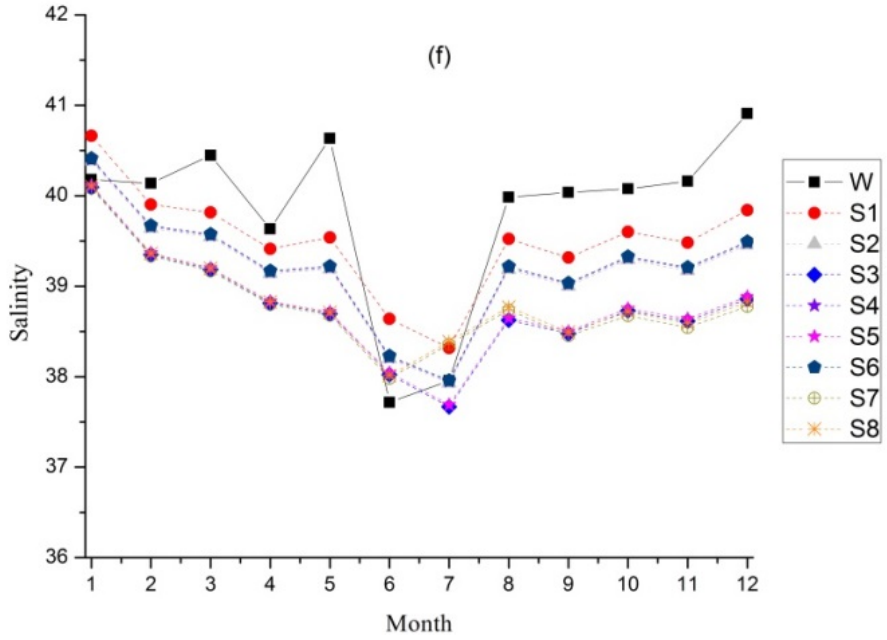

Figure 5-4 (f). WOA13 and simulated monthly averaged sub-surface salinity at Location 6 using various schemes for the period of 2005-2012. "W" represents "WOA13"; "S" represents "Salinity".

Table 5-5. RMSDs for sub-surface salinity at representative locations

Scheme**	L1*	L2	L3	L4	L5	L6
S1	0.2844	0.4597	0.5297	0.3880	0.5504	0.6757
S2	0.3865	0.4743	0.4069	0.2873	0.6065	0.8696
S3	0.5820	0.6227	0.3787	0.5122	0.9002	1.2758
S4	0.3549	0.4675	0.4279	0.2860	0.5957	0.8542
S5	0.5528	0.5969	0.3679	0.4923	0.8850	1.2570
S6	0.3466	0.4655	0.4394	0.2864	0.5892	0.8441
S7	0.6128	0.6746	0.3993	0.5466	0.9292	1.2986
S8	0.5631	0.6305	0.3694	0.5173	0.9043	1.2691

***. "L" represents "Latitude"**

****. "S" represents "Scheme"**

The impact of the momentum approach on the accuracy of the results in subsurface is not as large as that for surface salinity. This might be due to the reason that the rigid-lid approximation maintains the pressure variations at the upper surface by the force that would be exerted by the assumed rigid lid; in other words, the errors induced by the approximation at the surface (there is no vertical velocity) can be offset by the pressure variation. In effect, an observation for the deeper region of the Gulf shows that the performance of the rigid-lid approximation improves with the depth. However, for such a water body, the shallow region is of more interest.

In the case of sub-surface salinity modeling, the impacts of the equation of state and advection algorithm on the results are similar to those for surface salinity. The JMcD Equation of State is slightly better than the MJWF03 Equation of State and the Lax-Wendroff method is slightly better than the Adams-Bashforth method. However, the performance is also sensitive to the

momentum method, demonstrating that these methods or algorithms should not be considered separately.

Similar to the surface salinity analyses, the annual mean sub-surface salinity at various latitudes can give rise to the same conclusions as those drawn from the representative locations, but cannot provide detailed characteristics of seasonal variation; therefore, for brevity, they are not presented here.

5.6 Monthly averaged salinity distribution

Thus far, the most appropriate scheme for the prediction of salinity distribution in the Gulf has been figured out and verified: that is Scheme 1, which is the scheme with the JMcD Equation of State, the implicit free surface method for momentum equations, and the Adams-Bashforth advection algorithm for the tracer equations.

Therefore, the salinity distribution in the Persian Gulf modeled by Scheme 1 is looked at in this section.

In practice, the salinity distribution in a water body can be interpreted from a number of aspects; however, for the moment we will not attempt to describe all the aspects but instead focus on the surface salinity distribution due to the following reasons. Firstly, the surface salinity distribution is of primary interest for a preliminary analysis of shallow flows. Secondly, the surface salinity distribution to a large degree can represent the overall characteristics of the salinity distribution.

Two important observations for the surface salinity distribution in the Gulf have been reported by previous studies. One was from Reynolds (2003): the salinity in summer is lower than winter. Another was from Yao and Johns (2010): during winter and early summer, there is an increase in the salinity of the Indian Ocean's surface water, and the water becomes hypersaline in the northern Gulf and in the shallow southern Gulf; the salinity front, which separates the low-salinity Indian Ocean surface water and the high-salinity water in the Gulf, moves farther into the Gulf from winter to summer.

The monthly averaged surface salinity fields for the period 2005-2012 obtained from the current study are shown in Figure 5-5 (a) ~ Figure 5-5 (f) by alternate months.

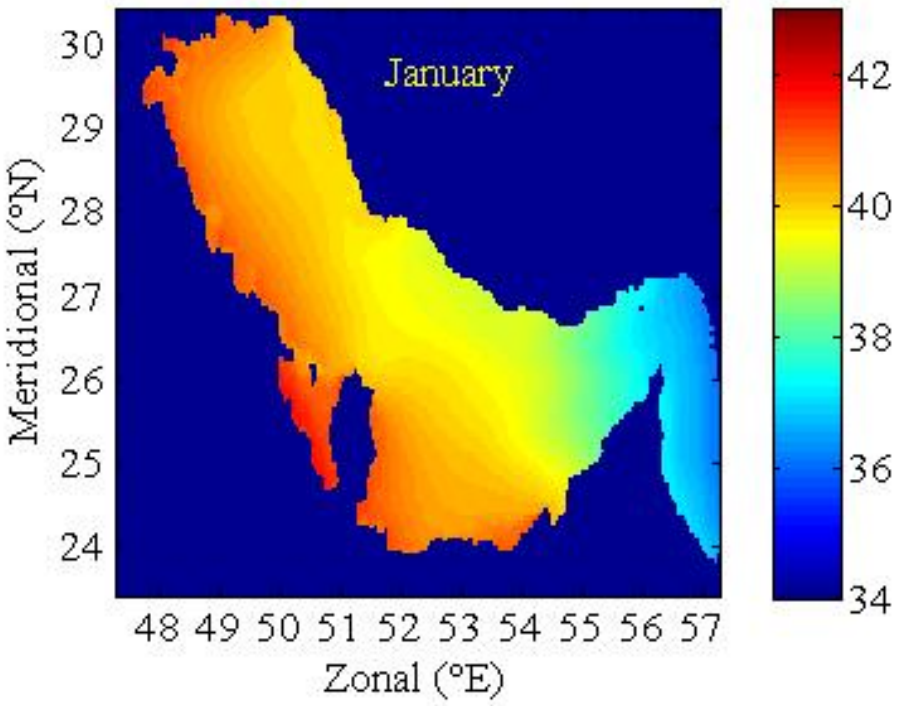

Figure 5-5 (a). Monthly averaged (January) surface salinity distribution in the Persian Gulf for the period 2005-2012

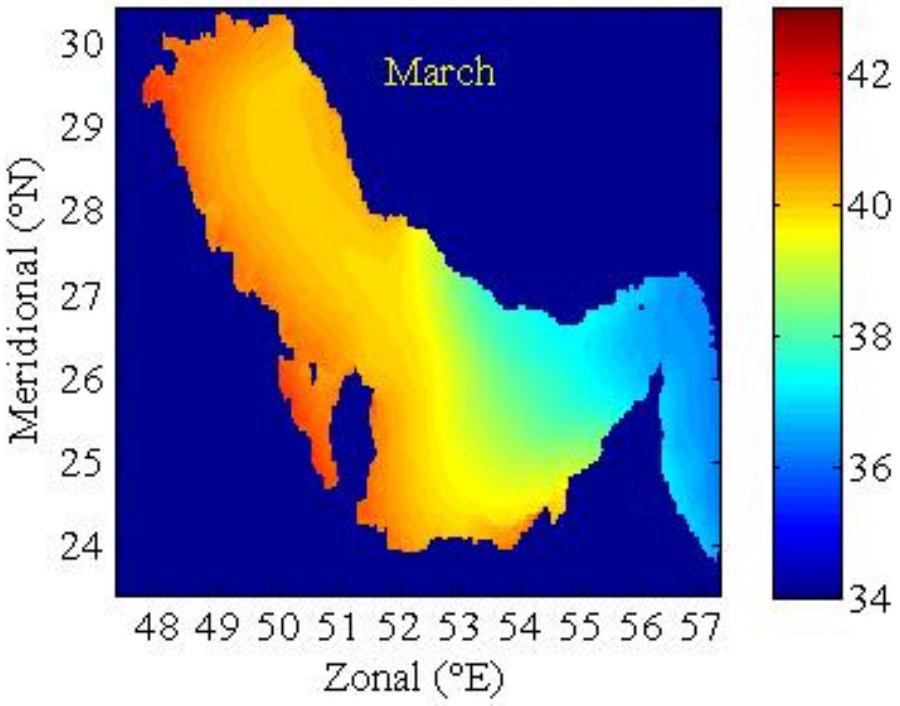

Figure 5-5 (b). Monthly averaged (March) surface salinity distribution in the Persian Gulf for the period 2005-2012

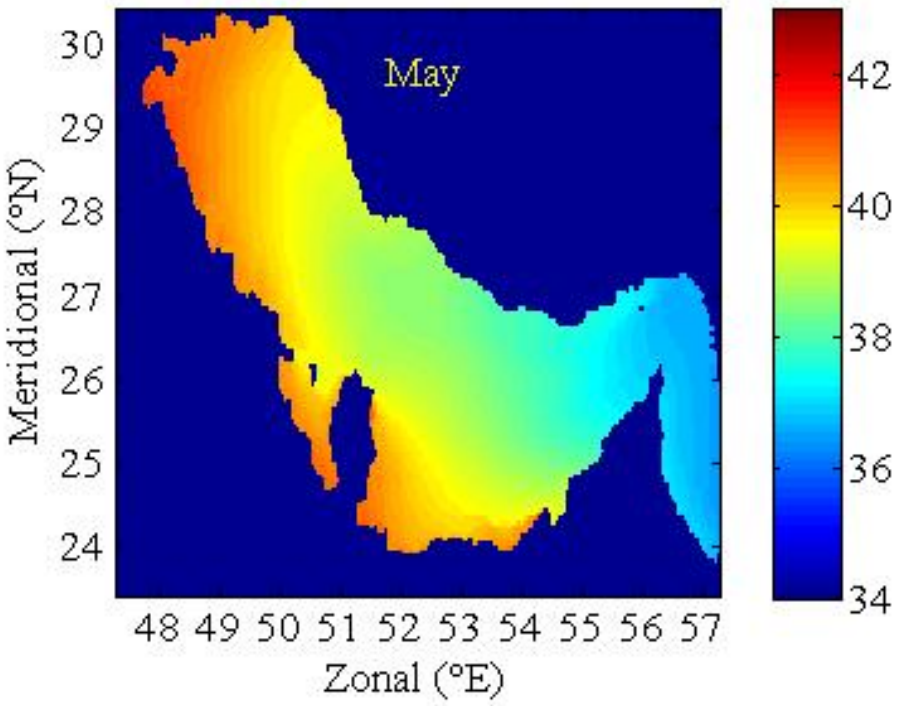

Figure 5-5 (c). Monthly averaged (May) surface salinity distribution in the Persian Gulf for the period 2005-2012

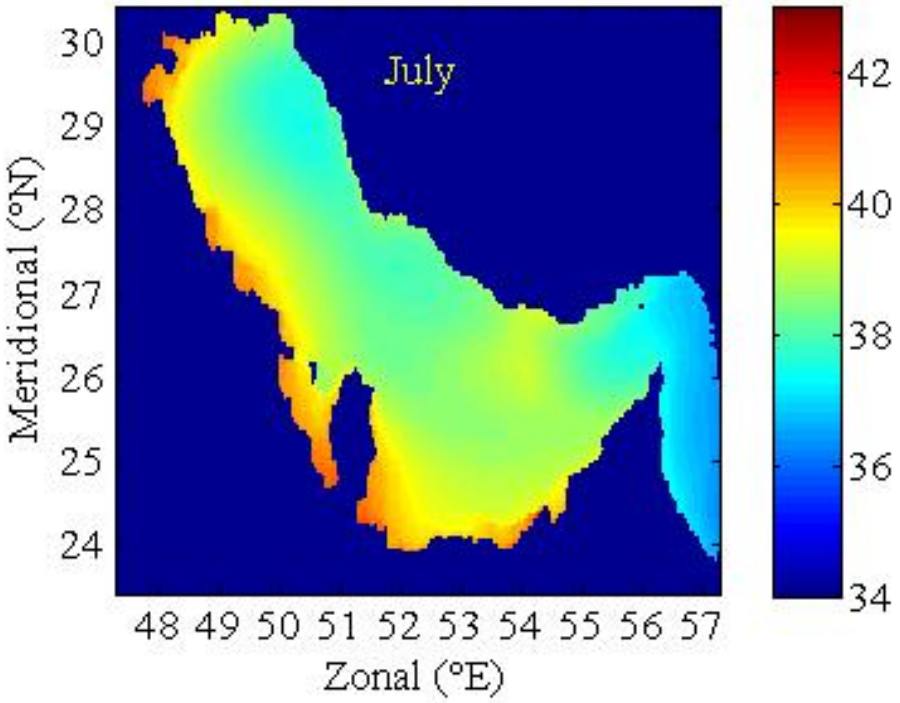

Figure 5-5 (d). Monthly averaged (July) surface salinity distribution in the Persian Gulf for the period

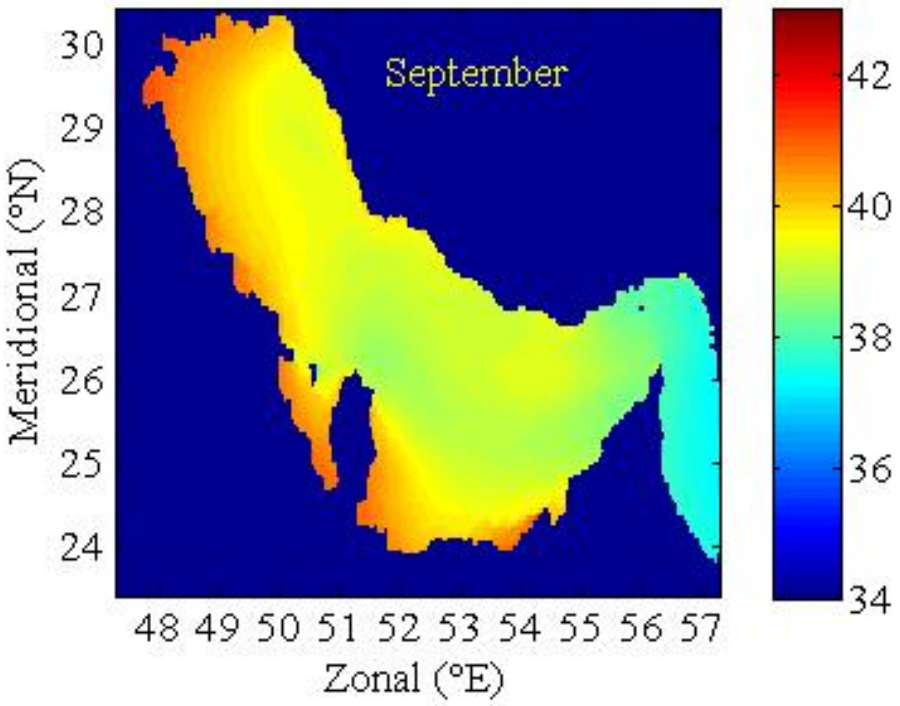

Figure 5-5 (e). Monthly averaged (September) surface salinity distribution in the Persian Gulf for the period 2005-2012

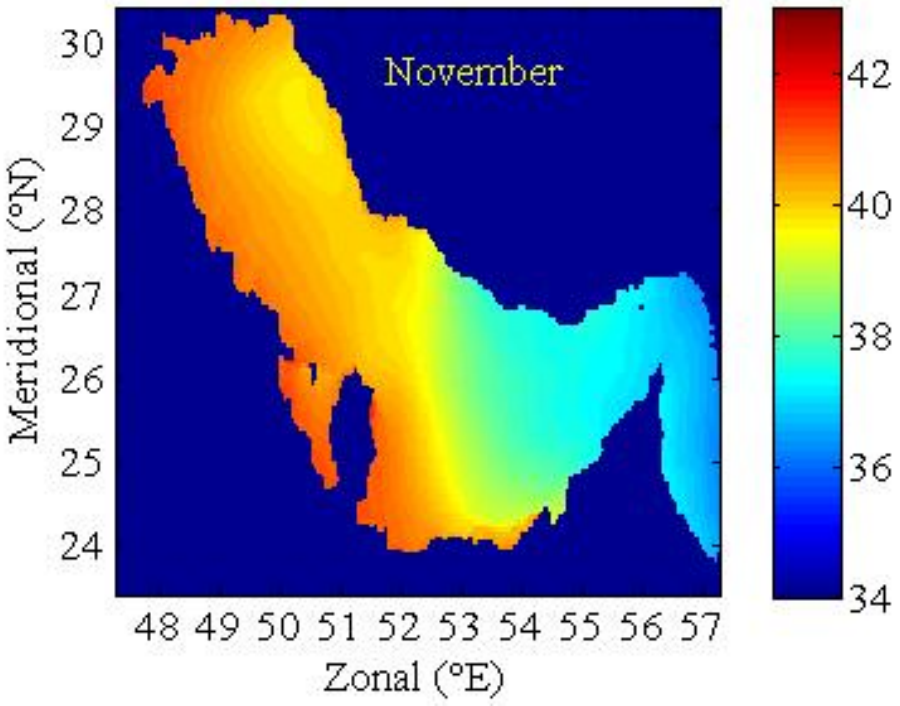

Figure 5-5 (f). Monthly averaged (November) surface salinity distribution in the Persian Gulf for the period 2005-2012

It can be seen that the salinity in summer is almost the lowest, which is in accordance with the observations of Reynolds (2003) but might contradict our intuitive judgement. Indeed, the temperature in summer is higher, but the wind is stronger during winter, introducing stronger winter evaporation, which can greatly concentrate the water in the Persian Gulf.

The salinity is always higher in shallower regions, probably because of the accumulation effects and the restriction of water exchange with ambient waters. In addition, the salinity front moves landward into the Persian Gulf from winter to summer, but during the period from fall to winter, it undergoes oscillations due to the existence of complex processes in this period, such as the strong variations in evaporation.

5.7 Discussions and Conclusions

In this study, numerical modeling of salinity distribution in a large-scale inverse estuary has been investigated. The Persian Gulf was chosen to be the study region since it is a typical large-scale inverse estuary and has been of significant research interest over the past several decades. Using different schemes (i.e., various combinations of equations of state, methods for solving the momentum equations, and advection algorithms for tracer equations), eight in all, we performed long-term and basin-wide simulations for the salinity distribution in the Persian Gulf for the period 2005-2012.

The modeled surface salinity at representative locations, surface salinity at various latitudes, and sub-surface salinity at representative locations were compared with the corresponding WOA13 data. The associated methodologies are discussed at some length. The most appropriate scheme for the case under study was figured out and verified through analyses of the comparisons; in practice, this validated scheme can also be used for further studies with respect to the long-term balance of salinity in a large-scale inverse estuary under climate change.

Some features that make the present study distinctive from previous studies include:

- Long-term simulations have been conducted. Different with the majority of previous studies related to the Persian Gulf, which were typically limited in time from hours to a few months, the current study simulated the salinity distribution in the study domain for decades.

Therefore, the results can be more convincing in terms of validating the model, and inspecting the long-term characteristics.

- This study evaluated the performance of various schemes. To the author's knowledge, previous numerical studies in this topic used various schemes but did not explain with details about the reason why their schemes were selected. In this thesis, however, various schemes have been assessed in detail through a practical and large-scale case study.

The important observations of the present study are listed below:

- The adoption of an appropriate scheme has a crucial impact on the simulation, especially for surface salinity distribution. Therefore, it is necessary to first consider the performance of various schemes prior to applying the model to a practical problem.

- The employed model followed closely the increase and decrease of salinity with time, but tended to underestimate the salinity because small desalination plants and biogeochemical processes as well as irregular wind bursts were not taken into account.

- The schemes with the implicit free surface approach had a closer agreement with the WOA13 data as compared to those provided by the schemes with the rigid-lid approximation, possibly because the rigid-lid approximation excluded the free freshwater flux.

- The impact of the momentum methods on the simulated sub-surface salinity distribution was not as large as that for the surface salinity distribution, since the rigid-lid approximation, while not precise enough for the surface, can still maintain a reasonable accuracy for subsurface values.

- The equation of state, advection algorithm and momentum method, interact and have impact on each other. The mechanism is that the effect of one factor in a system might be offset or magnified by other effects; and this fact can also be explained and quantified by the path analysis model initially developed by Wright (1921).

- The MJWF03 Equation of State, rigid-lid momentum method, and Adams-Bashforth advection algorithm can result in a reduction in computational cost. However,

computational efficiency has not been regarded as the primary concern of this project, as the effects of different schemes were rather obvious.

- The most appropriate scheme in this case study is the scheme with the JMcD Equation of State, implicit free surface approach for solving the momentum equations, and Adams-Bashforth advection algorithm for tracer equations.

- The model deviated farther from the actual measurements at locations with higher latitudes, mainly due to sharp changes in salinity with time that exist at higher latitudes but not at lower latitudes. Those sharp changes could be the result of specific geometry of the domain that influences the hydrodynamic and mixing, and the impact of the rivers located at higher latitudes.

- The model performed better for sub-surface salinity than for surface salinity because the model is more capable in predicting smoother variations of salinity, and the variation is relatively smoother in sub-surface salinity.

At the moment, the optimal scheme for the case of the Persian Gulf has been pointed out and validated, which is the scheme with JMcD Equation of State, implicit free surface approach for solving the momentum equations, and Adams-Bashforth advection algorithm for tracer equations.

This scheme will be discussed and employed further to inspect the long-term variation of salinity in the Persian Gulf, which will be presented in the next chapter.

Chapter 6 Numerical Modeling of the Long-term Salinity Response of the Persian Gulf to the Climate Change and Anthropogenic Activities

Abstract This chapter will explain the study of the long-term salinity response of the Persian Gulf to the climate change and anthropogenic activities. It is important to predict the long-term salinity variation in the Persian Gulf, especially in terms of environmental management and water resources utilization. The Persian Gulf is a shallow body of water, so its salinity is obviously sensitive to climate changes and anthropogenic activities. However, to the best of the author' knowledge, a detailed numerical prediction of long-term (both temporal and spatial) salinity response of the Persian Gulf to the climate change and anthropogenic activities has not been reported in the literature. Therefore, this study will use the model calibrated and validated in the previous chapter to predict the spatial and temporal salinity variations in the Persian Gulf for the period 2015-2060, corresponding to the climate change and anthropogenic activities. The results will show that the salinity in the Persian Gulf tends to increase with time and there are some distinctive spatial characteristics of the salinity distribution.

6.1 Introduction

Partially due to the climate change, there have been changes of salinity in Earth's oceans, and some oceans are getting saltier while some others are getting fresher. It has been reported that the change of salinity in world's oceans over the past 50 years has been about 0.2 psu, which is about 0.5 percent (IS, 2015). Salinity is playing an important role not just in the water body itself but also in, just to mention a few, global circulation, climate, agriculture, natural habitat, and so on. Besides, a prediction of long-term balance of salinity can also provide useful information for future water management, development of water transport and environmental assessment of proposed industries.

The Persian Gulf is a partially enclosed marginal sea connected to the Indian Ocean. The problem with respect to salinity in this area is more serious than the majority of other water bodies in the world, mainly because it is an inverse estuary. More specifically, the evaporation in the Persian Gulf is much larger than the sum of the precipitation, river discharges, and seawater compensation (Cavalcante *et al.*, 2011). Therefore, it encounters a severe net freshwater loss.

Predictions of salinity variations in water bodies are significantly important, particularly in terms of environment management and water resources utilization. Since the Persian Gulf is a

shallow body of water (Badri *et al.*, 2010), the salinity in it is greatly sensitive to climate changes and anthropogenic activities. Thus, in order to reasonably predict the salinity variation in the Persian Gulf, it is necessary to take into account the climate change and anthropogenic activities in this region.

Generally, long-term salinity responses of a water body to future climate changes and anthropogenic activities can be predicted by two families of methods: statistical methods and numerical simulation methods. Nunes-Vaz (2012) analyzed the salinity change of Spencer Gulf in South Australia based on observational data spanning 27 years, and found out the relationship between forcing and salinity response by using a statistical method. This computed relationship can be used in turn to compute the future salinity variation corresponding to the predicted forcing. Statistical method has been widely applied to similar problems. However, it primarily has two disadvantages to be utilized for the case of the Persian Gulf. First, statistical method requires a complete dataset of all the relevant variables but this kind of dataset is not always available. Second, typically statistical method can only predict the overall trend of salinity variation in a water body but sometimes spatial characteristics may also be of interest. Numerical simulation method can overcome these two drawbacks of statistical method, and its application has been widely accepted. Elhakeem and Elshorbagy (2013) proposed a hydrodynamic simulation for the prediction of future salinity change in the Persian Gulf. Their method can be very practical and robust, especially when there is a lack of data in the study domain. However, to the authors' knowledge, a detailed numerical prediction of the long-term (both temporal and spatial) salinity response of the Persian Gulf to the climate change and anthropogenic activities has not been reported in the literature.

In the previous chapter, a numerical model was calibrated and validated according to the WOA13 data (World Ocean Atlas, 2013), and in the present chapter this validated model is used to simulate the salinity in the Persian Gulf for the period 2015-2060, with the climate change and anthropogenic activities in this region considered. Finally, the results are analyzed and discussed to conclude the long-term characteristics of salinity changes in this region.

This chapter is organized as follows: Section 6.2 introduces the adopted approach; Section 6.3 describes the validation of the numerical model; Section 6.4 presents and discusses our predictions; and Section 6.5 summarizes the conclusions.

6.2 Approach

Chapter 3 summarized the general methodology of the studies presented in the current thesis, and this section primarily describes the approach specifically used in the present study.

MITgcm (MIT general circulation model; Marshall *et al.,* 1997) is employed as our primary numerical model. A distinctive feature of MITgcm is that it has a non-hydrostatic capacity. However, the Persian Gulf is a shallow body of water, so we first examined whether the hydrostatic assumption can be applied to this case or not prior to using the non-hydrostatic capacity directly. It was found that the hydrostatic simulation produces almost the same results as those predicted by the non-hydrostatic simulation but save more than 20% of the simulation time. Therefore, the hydrostatic assumption is adopted in the present study.

The time step is set to be 180 seconds, which meets the Courant stability condition. A smaller time step (90 seconds) has been tested but it does not change the results. We use a spherical polar coordinate system with a grid resolution of 0.05°×0.05°, and interpolate the outputs using Kriging interpolation method (Oliver & Webster, 1990). The deviation of the interpolated results from those produced by the simulation with a grid resolution of 0.01°×0.01° is negligible.

Basic inputs for the simulation include the bathymetry, temperature, and wind stress, initial condition of salinity, river discharges, precipitation, heat flux, evaporation, boundary tidal forcing and desalination capacity. The temperature and wind stress are regarded as the representations of the climate change in the Persian Gulf while the river discharges and desalination capacity are viewed as the main representations of the anthropogenic activities. To incorporate the climate change into our simulation, a downscaling method is employed to obtain the projections of temperature and wind speed in the Persian Gulf corresponding to the four representative concentration pathways (Van Vuuren, *et al.*, 2011), and the averaged values of these projections are used. In terms of human activities, the properties of river discharges and precipitation are basically kept constant, and a parameter for the freshwater flux is employed to represent the impacts of human activities.

6.3 Validation

In order to calibrate and validate the numerical model, the salinity distribution in the Persian Gulf for the period 2005-2012 is simulated and compared with the WOA13 data. The calibration and validation are basin-wide and long-term, so they can be more convincing than most of the previous studies.

Chapter 5 compared various combinations of equations of state, momentum methods and numerical algorithms, and figured out the most appropriate scheme for predicting the salinity distribution in the Persian Gulf. Some parts of the comparisons are observed and analyzed further in this section, for validating the utilization of the numerical model in predicting the long-term salinity response of the Persian Gulf to the climate change and anthropogenic activities.

Figure 6-1 (a) to Figure 6-1 (f) shows the WOA13 and the simulated monthly-averaged surface salinity for the period 2005-2012 at 6 stations distributed in different regions of the Persian Gulf. These figures indicate that the model predicts correctly the drop and rise of the salinity changes, which demonstrates the utilization of the numerical model in predicting the trend of salinity variations in the Persian Gulf.

Overall, the simulated results match the WOA13 data satisfactorily. The deviations are mainly due to the fact that some irregular wind bursts, floods, biological process, some small desalination plants, etc. are ignored. In general, the simulated results deviate farther from the WOA13 data during summer, primarily because there are more sudden and large variations during summer while the numerical model is more capable of predicting relatively smooth variations.

The model overestimates the salinity in some parts, while underestimates it in some other parts, so the majority of the errors can be offset. Therefore, it can be concluded that the model performs better in predicting the overall balance of salinity in the study domain than the monthly-averaged salinity distribution. In addition, the model can perform better in capturing the sub-surface salinity, since there are fewer sudden and large changes of salinity below the surface than at the surface. Therefore, the model can also satisfactorily achieve the main goal of the present study (to predict the long-term salinity variations in the Persian Gulf).

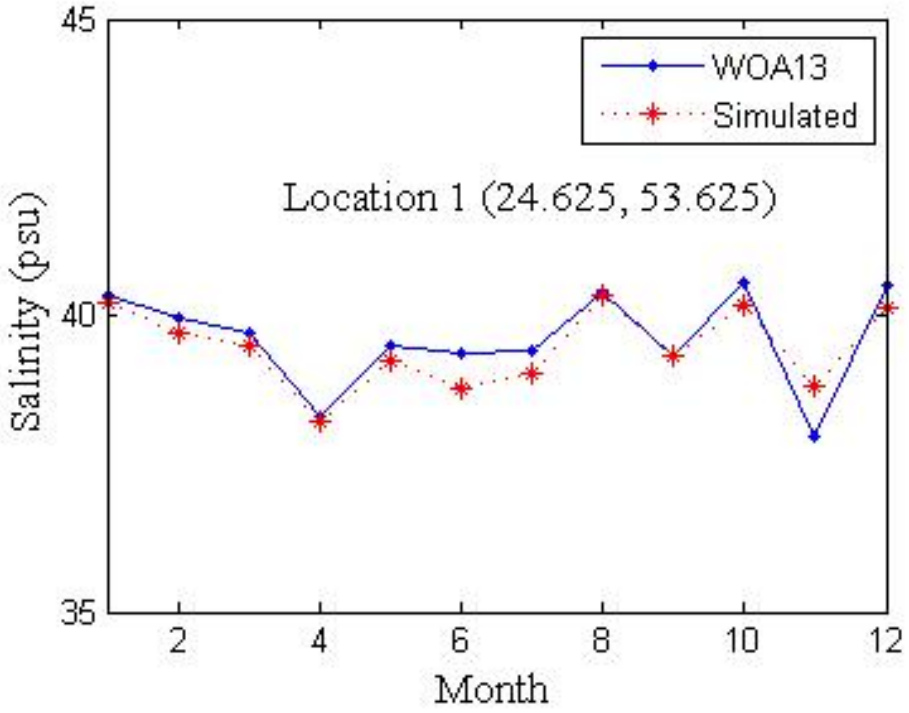

Figure 6-1 (a). WOA13 and simulated monthly-averaged surface salinity for the period 2005-2012. The first number in the parenthesis represents the latitude, and the second one represents the longitude

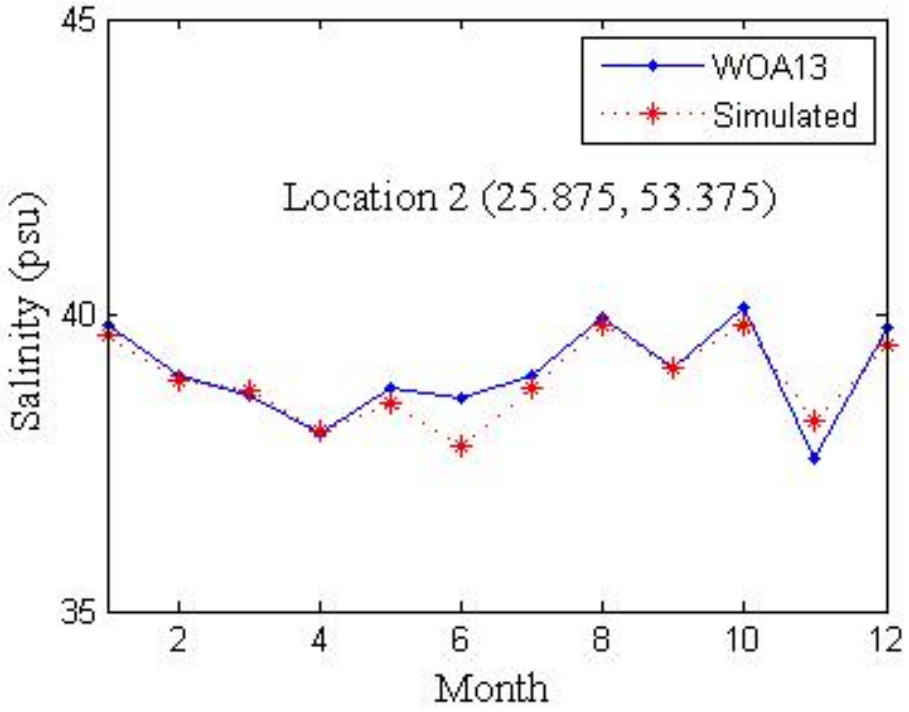

Figure 6-1 (b). WOA13 and simulated monthly-averaged surface salinity for the period 2005-2012. The first number in the parenthesis represents the latitude, and the second one represents the longitude

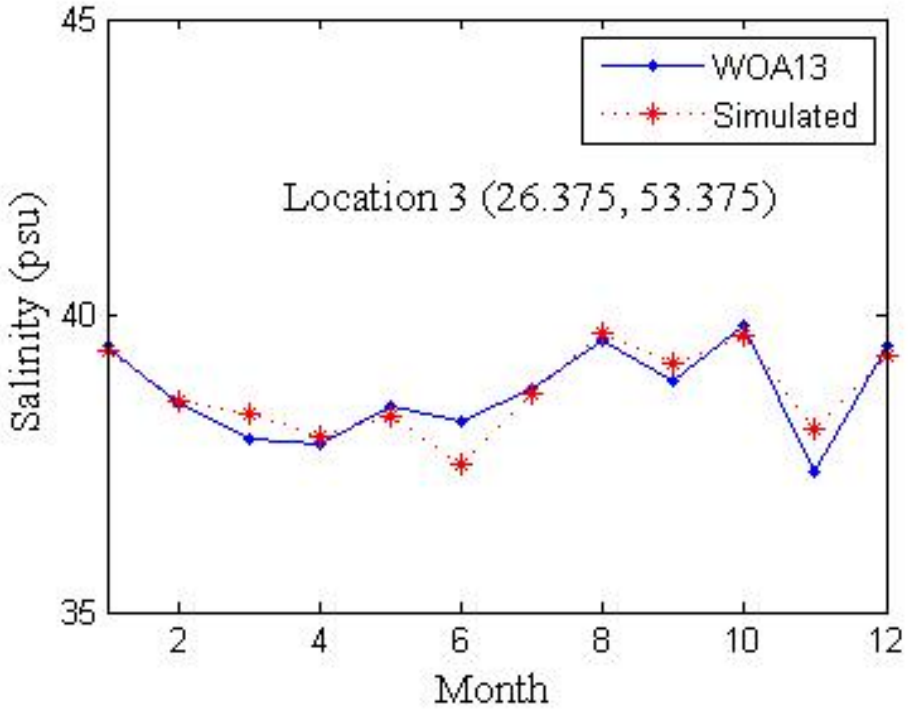

Figure 6-1 (c). WOA13 and simulated monthly-averaged surface salinity for the period 2005-2012. The first number in the parenthesis represents the latitude, and the second one represents the longitude

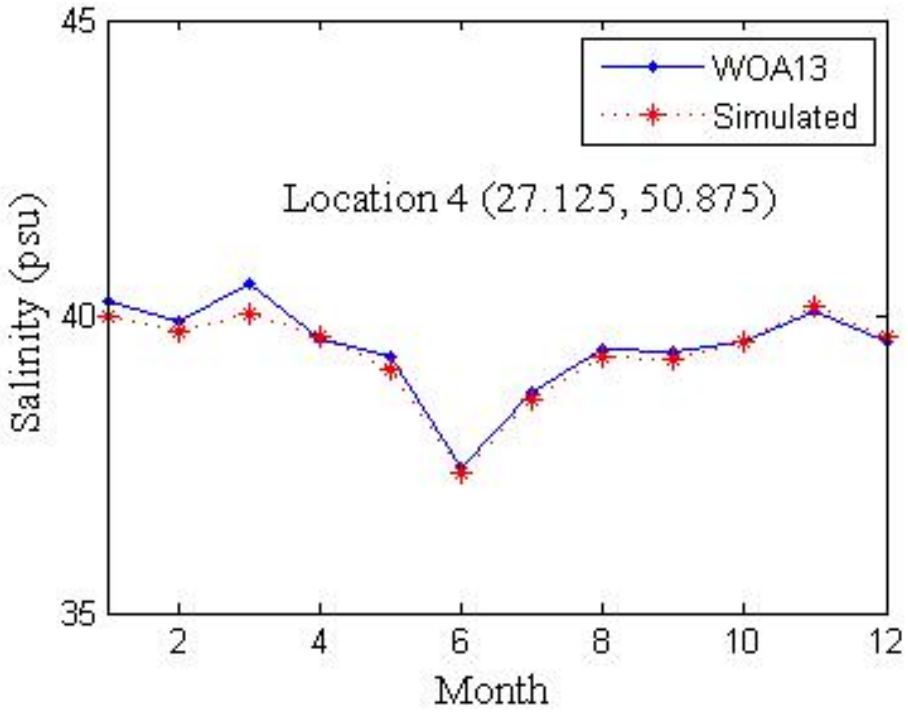

Figure 6-1 (d). WOA13 and simulated monthly-averaged surface salinity for the period 2005-2012. The first number in the parenthesis represents the latitude, and the second one represents the longitude

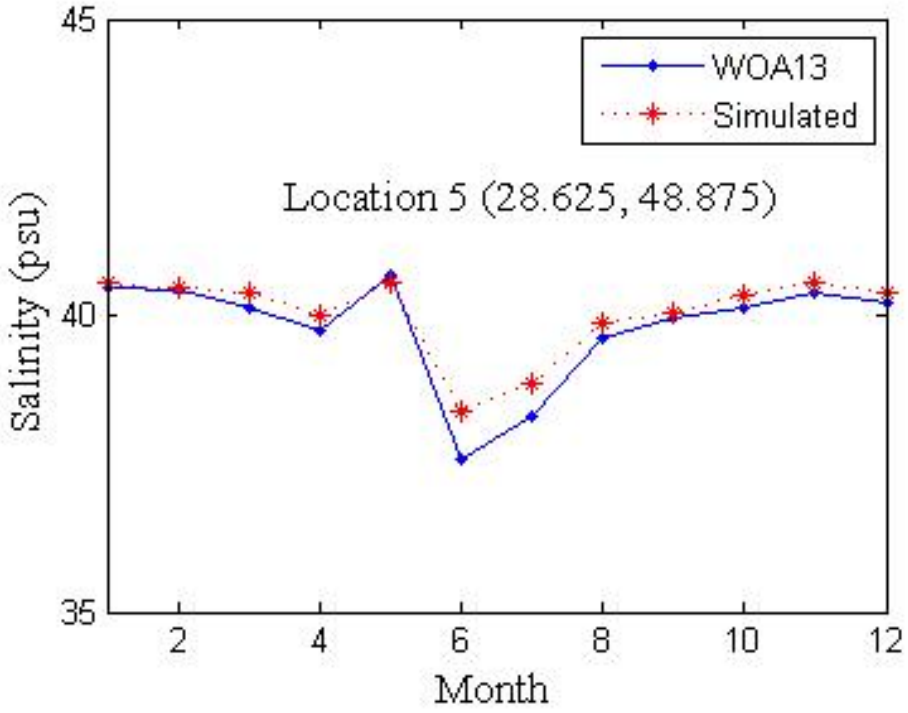

Figure 6-1 (e). WOA13 and simulated monthly-averaged surface salinity for the period 2005-2012. The first number in the parenthesis represents the latitude, and the second one represents the longitude

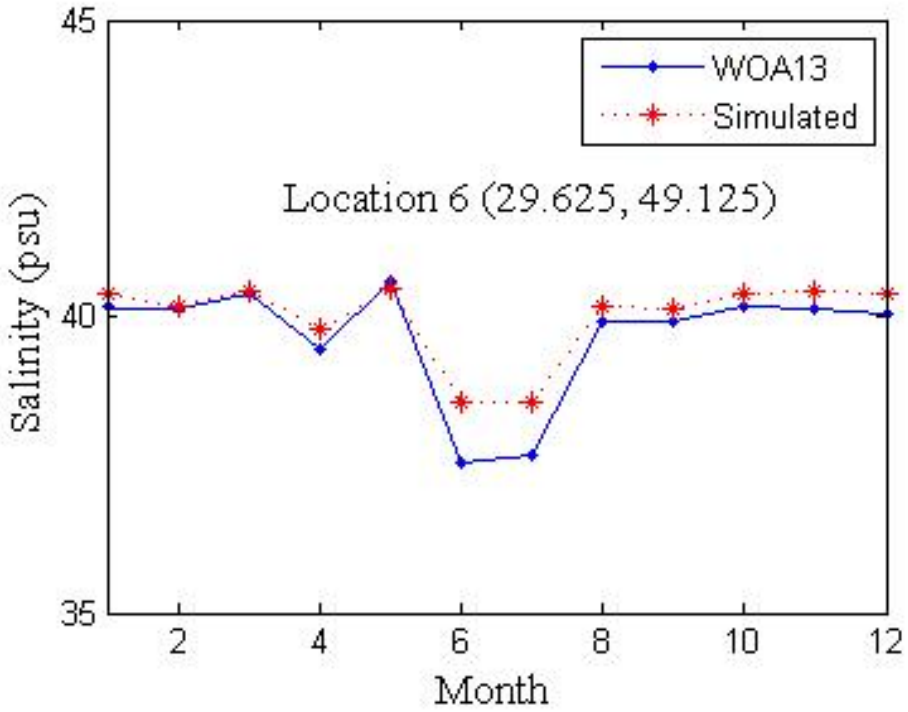

Figure 6-1 (f). WOA13 and simulated monthly-averaged surface salinity for the period 2005-2012. The first number in the parenthesis represents the latitude, and the second one represents the longitude

6.4 Results and discussion

6.4.1 The Long-term Salinity Variations of the Persian Gulf

To predict the long-term (both temporal and spatial) salinity response of the Persian Gulf to the climate change and anthropogenic activities, we use the validated numerical model to simulate the salinity distributions in the Persian Gulf for the period 2015-2060. For long-term predictions, seasonal variations are less concerning, so the output-write-interval is set to be one year, and the salinity distributions in January is employed for the analysis of the long-term characteristics of salinity variations in the Persian Gulf.

From the simulated results (Figure 6-2 (a) ~ Figure 6-2 (f)), one can see that the salinity in the Persian Gulf is continually increasing with time in the future half-century. There are several facts that can lead to this increase: for instance, the temperature and wind speed in the Persian Gulf are continually increasing so that the evaporation is getting stronger and stronger. Besides that, human activities, such as establishments of dams and desalination plants, also have an impact on the balance of salinity in this region.

Overall, the salinity increase in the southern Gulf is faster than that in the northern Gulf. This characteristic is partially determined by the fact that nowadays there are more human activities in the southern Gulf. To be precise, there are more desalination plants.

Similarly, the salinity in the middle-Gulf is increasing faster than that in the western Gulf. The increase of salinity is relatively small in the eastern Gulf because it is closer to the Indian Ocean, the water from which can dilute the water in the Persian Gulf.

Besides, the coastal salinity will be higher than that offshore. In addition to the fact that there are more human activities along coastal areas, there are two more reasons: first, the water near shore is generally shallower so the accumulation effect is more influential; second, the communication between the water in near shore with the ambient water is more restricted than that offshore.

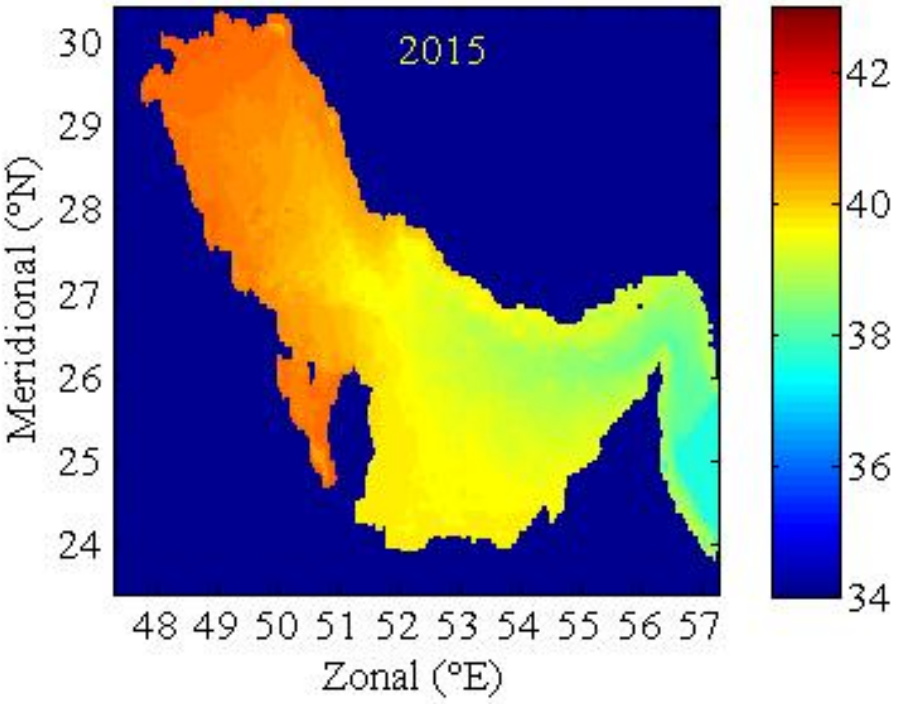

Figure 6-2 (a). Salinity distribution in the Persian Gulf in 2015

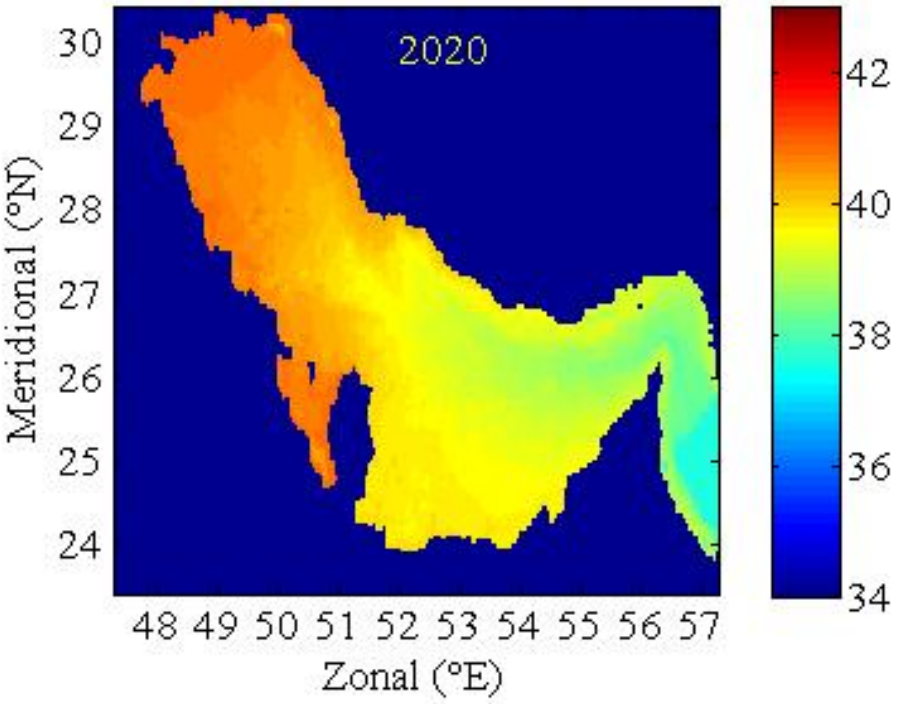

Figure 6-2 (b). Salinity distribution in the Persian Gulf in 2020

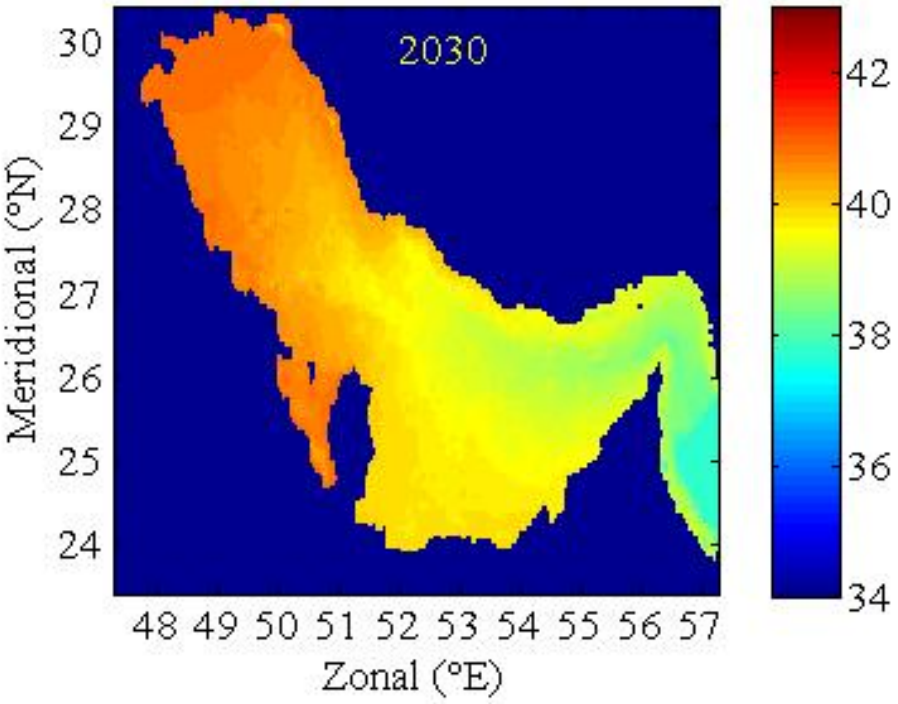

Figure 6-2 (c). Salinity distribution in the Persian Gulf in 2030

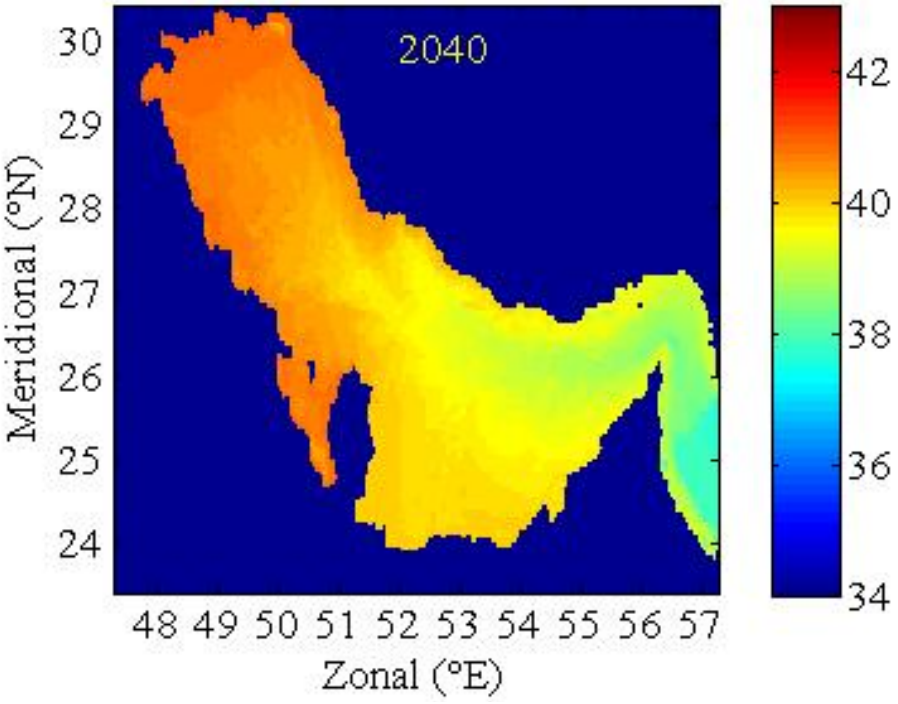

Figure 6-2 (d). Salinity distribution in the Persian Gulf in 2040

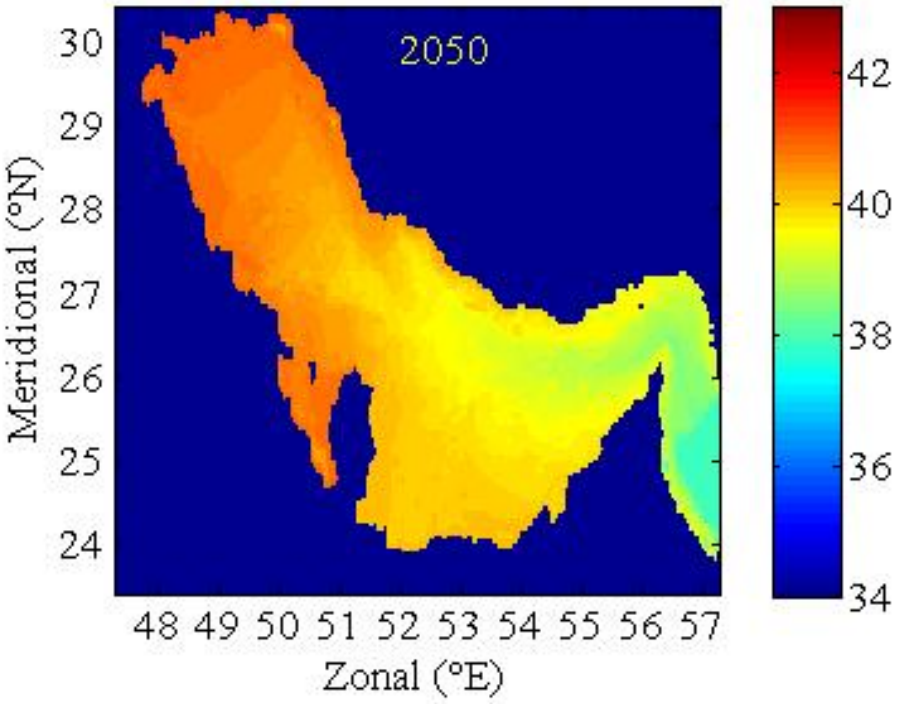

Figure 6-2 (e). Salinity distribution in the Persian Gulf in 2050

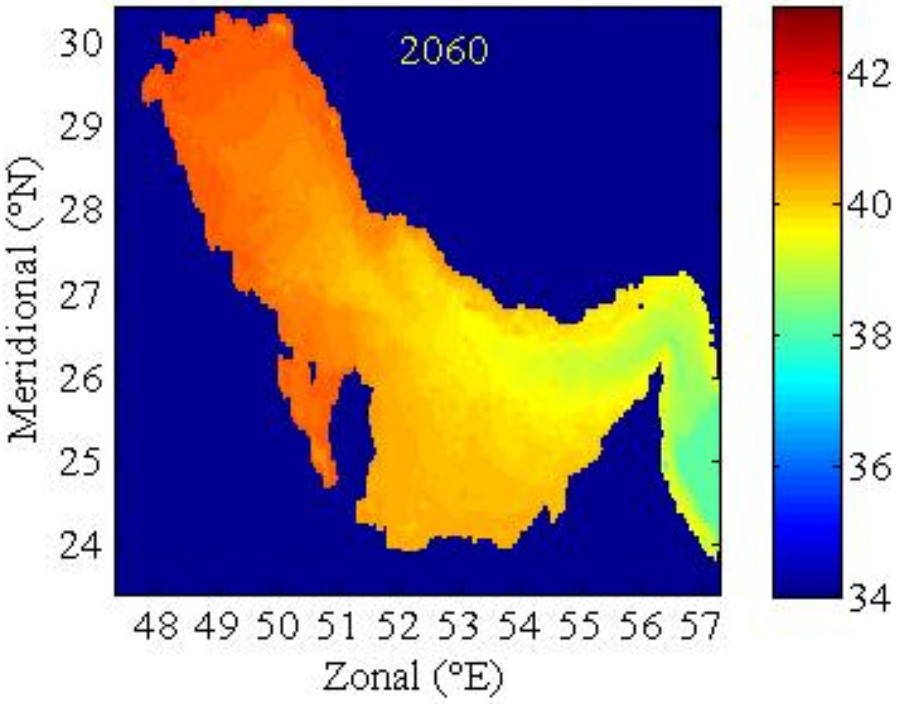

Figure 6-2 (f). Salinity distribution in the Persian Gulf in 2060

6.4.2 The Long-term Salinity Variations at Various Latitudes

Section 6.4.1 qualitatively analyzed the long-term salinity variations of the Gulf. For the purpose of obtaining a more detailed and quantitative representation of the long-term trends of salinity variations at various latitudes, time series of latitude-averaged salinity in the surface layer during the period 2015-2060 are plotted in Figure 6-3.

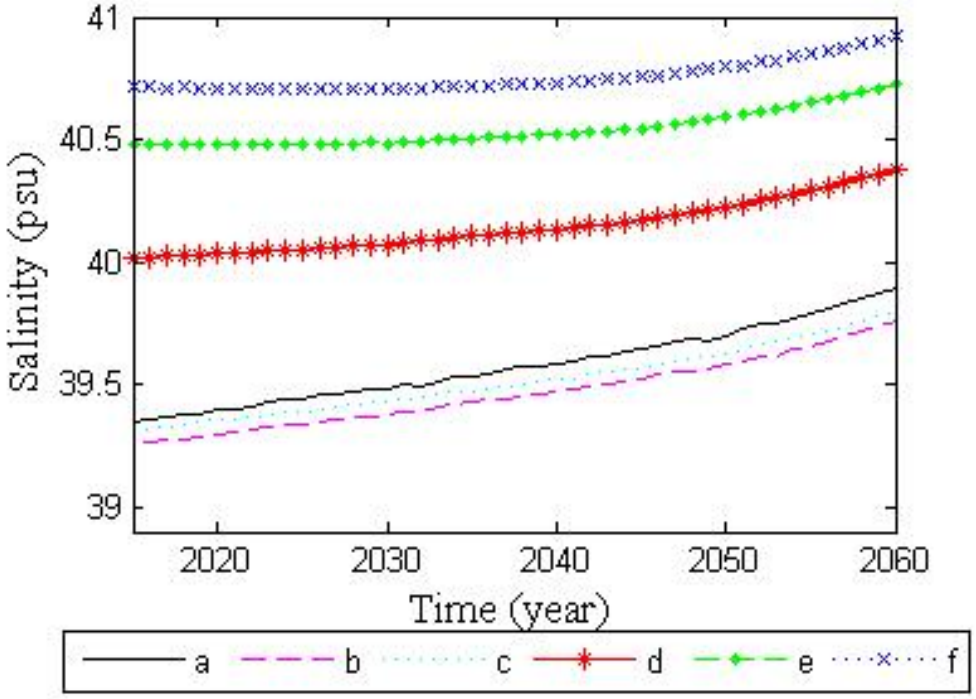

Figure 6-3. Time series of latitude-averaged salinity in the surface layer during the period 2015-2060. (a): Latitude 23°~25°; (b) Latitude 25°~26°; (c) Latitude 26°~27°; (d) Latitude 27°~28° ; (e) Latitude 28°~29°; (f) Latitude 29°~31°

From Figure 6-3, one can understand that the latitude-averaged salinities are generally increasing with time, similar to the domain-averaged trends. Small oscillations occur, primarily at low latitudes, and these oscillations are mainly caused by the hydrodynamics in the Persian Gulf. The reason why oscillations are more likely to occur at low-latitude regions of the Persian Gulf is that these regions are closer to the Strait of Hormuz, which can make the flow dynamics and other associated processes in these regions more complex.

In order to obtain a more straightforward measure of the general trends of salinity variations in the Persian Gulf at various latitudes, the fitted functions are calculated using a linear regression method (see Appendix 1).

Table 6-1. Fitted functions for salinity variations at various latitudes

Latitude	Fitted Function
a (23°~25°)	$S = 0.0144 y_r + 16.4136$
b (25°~26°)	$S = 0.0104 y_r + 18.1971$
c (26°~27°)	$S = 0.0101 y_r + 18.8782$
d (27°~28°)	$S = 0.0074 y_r + 25.1372$
e (28°~29°)	$S = 0.0049 y_r + 30.6259$
f (29°~31°)	$S = 0.0040 y_r + 32.5613$

The intercepts of the fitted functions for the various latitudes (from low latitudes to high latitudes) are 16.4136, 18.1971, 18.8782, 25.1372, 30.6259, and 32.5613, respectively. Both these items and the plots (Figure 6-3) suggest that presently the salinity in the northern Gulf is higher than that in the southern Gulf. Basically this characteristic can be attributed to the fact that the water in the southern Gulf is more diluted by seawater because this region is closer to the Indian Ocean.

However, a closer examination reveals the fact that the current situation will gradually change in the future. The coefficients of independent variables in the fitted equations (from low latitudes to high latitudes) are 0.0114, 0.0104, 0.0101, 0.0074, 0.0049, and 0.0040, respectively. These coefficients imply that the speed of the salinity increase is decreasing along the positive meridional direction, which means that the salinity in the southern Gulf will increase faster than that in the northern Gulf. This feature is mainly due to the human activities and climate change. Therefore, it is reasonable to conclude that the differences of salinity between the southern and northern Gulf will be decreasing with time in the next half-century.

In addition, the slopes of the lines in Figure 6-3 are typically positive, and these slopes are generally increasing with time (as Figure 6-3 shows, all of the lines are concave). The characteristics of these slopes indicate that the speed of the increase of latitude-averaged

salinities in the Gulf is also increasing with time, which is consistent with the fact that the temperature and the wind speed are increasing, and there will be more human activities in the future.

6.4.3 The Long-term Salinity Variations at Various Longitudes

To obtain a more detailed and quantitative representation of the long-term trends of salinity variations at various longitudes, time series of longitude-averaged salinity in the surface layer during the period 2015-2060 are plotted in Figure 6-4. Note that the figure does not show the salinity at regions farther than Longitude 56°. As a matter of fact, the increase of salinity in the regions farther than the Strait of Hormuz is quite small because of the proximity to the Indian Ocean and the less-restricted water exchange, so the salinity in these regions is less concerning.

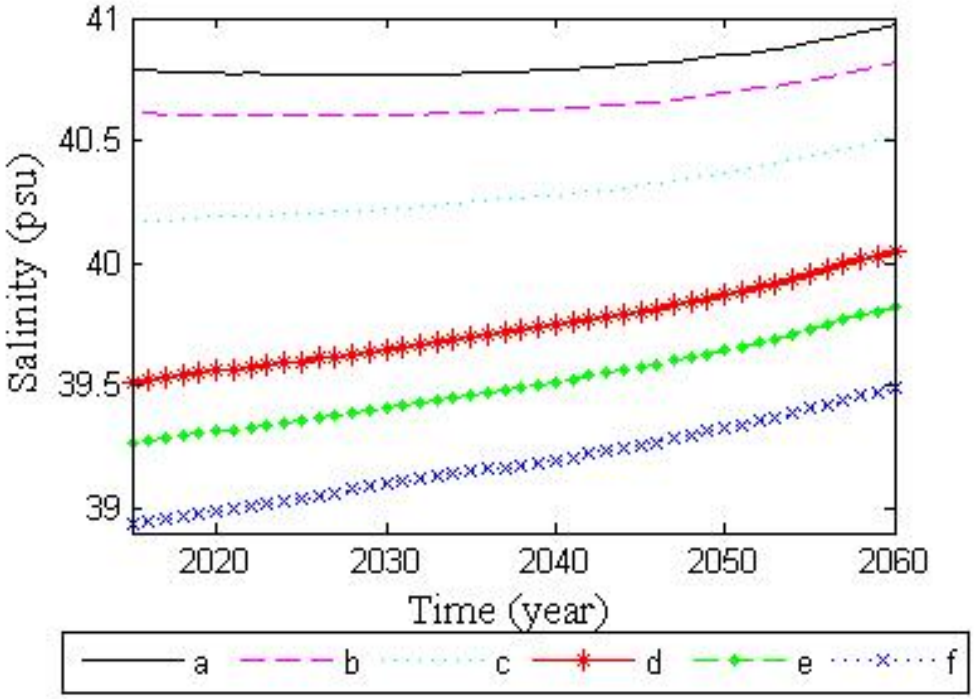

Figure 6-4. Time series of longitude-averaged salinity in the surface layer during the period 2015-2060. (a): Longitude 47°~49°; (b) Longitude 49°~50°; (c) Longitude 50°~52°; (d) Longitude 52°~53° ; (e) Longitude 53°~54°; (f) Longitude 54°~56°

Figure 6-4 implies that generally the longitudinally-averaged salinities tend to increase with time, similar to the laterally-averaged and latitude-averaged trends of salinity variations. Some small oscillations will also occur. The reason why oscillations are more likely to occur at higher longitudes is similar to the reason explained in the previous section: this region is closer to the Strait of Hormuz so the flow dynamics as well as other associated processes are more complex.

Also, the fitted functions for the trends of salinity variations in the Persian Gulf at various longitudes are calculated in Table 6-2, aiming to get a more straightforward measure of the general trends.

Table 6-2. Fitted functions for salinity variations at various longitudes

Longitude	Fitted Function
a (47°~49°)	$S = 0.0035y_r + 33.6236$
b (49°~50°)	$S = 0.0041y_r + 32.3239$
c (50°~52°)	$S = 0.0072y_r + 25.7115$
d (52°~53°)	$S = 0.0114y_r + 16.5809$
e (53°~54°)	$S = 0.0119y_r + 15.3187$
f (54°~56°)	$S = 0.0118y_r + 15.1454$

The intercepts of these functions (from low longitudes to high longitudes) are 33.6236, 32.3239, 25.7115, 16.5809, 15.3187, and 15.1454, respectively. Both these items and Figure 6-4 can imply that at present the salinity in the western Gulf is higher than that in the eastern Gulf. This characteristic can attribute to a fact similar to the one explained in the previous section; that is, the water in the eastern Gulf is more diluted by seawater as this region is closer to the Indian Ocean.

A closer inspection about the speed of salinity increase with time is also conducted. The coefficients of independent variables in the fitted equations (from low longitudes to high longitudes) are 0.0035, 0.0041, 0.0072, 0.0114, 0.0119, and 0.0118 respectively. These coefficients demonstrate that the speed of salinity first increases and then decreases along the positive zonal direction. In other words, the salinity at middle-longitude regions increases faster than that at low-longitude and high-longitude regions. In addition to the human activities, the

dilution process can be another factor that is responsible for this feature, particularly for the fact that the speed of salinity increase in the eastern Gulf is decreasing along the positive zonal direction.

In accordance with the latitude-averaged trends, almost all of the lines are concave, which means that the speeds of increase of the salinities at various longitudes will continuously increase with time. However, according to the classification shown in Table 1-1, the Gulf water will still be “seawater” instead of “Brine water”.

6.5 Conclusion

In the present study, the calibrated model is employed to predict the long-term salinity response of the Persian Gulf to the climate change and anthropogenic activities. The simulated salinity distributions in the Persian Gulf in various future years (temporal distribution), the latitude-averaged and longitude–averaged salinities (spatial distribution) in the surface layer during the period 2015-2060 are observed and analyzed. Some important observations of the present study are listed below:

- In General, the salinity in the Persian Gulf is continually increasing with time during the next half-century (about 1.27%), as a result of the climate change (the increasing wind speed and temperature) and anthropogenic activities (e.g. desalination).
- The speed of salinity increase in the Persian Gulf is also increasing with time, which can make the problem associated with salinity in this region more and more serious.
- Small oscillations related to the trends of salinity variations are more likely to occur at low-latitude and high-longitude regions, mainly because these regions are more influenced by the seawater inflow from the Strait of Hormuz.
- The salinity will constantly be higher near shore than offshore, since there are more human activities and typical the coastal regions in the Persian Gulf are also shallow-water regions.
- The salinity in the southern Gulf increases faster than that in the northern Gulf during the next half-century, partially due to the spatial distribution of anthropogenic activities.
- The salinity at middle-longitude regions increases faster than those at low-longitude and high-longitude regions, as a result of the human activities, and seawater inflows.

In this chapter, we predicted the trend of long-term balance of salinity in the Persian Gulf from the current situation to the year of 2060. Further studies can be conducted to predict the trends corresponding to some other scenarios. The purpose of the project is to obtain the general trend of the salinity variation in this region, and the next chapter will summarize and conclude this thesis.

Chapter 7 Summary and Conclusions

This thesis introduced the background knowledge, described the study domain, reviewed the relevant literature, and presented two studies related to the salinity distribution in the Persian Gulf.

In the study of numerical modeling of salinity distribution in an inverse estuary, the salinity distribution in the Persian Gulf for the period 2005-2012 was simulated. Eight combinations of equations of state, methods for dealing with the free surface in the momentum equations, and advection algorithms for tracer equations were examined, and their results were compared with WOA13 data. The surface salinity distribution at representative locations, surface salinity distribution at various latitudes, and sub-surface salinity distribution at representative locations were analyzed for evaluating the performance of the distinctive schemes. Finally, the scheme with JMcD Equation of State, implicit free surface approach for solving the momentum equations, and Adams-Bashforth advection algorithm for tracer equations was figured out to be the best scheme for predicting the salinity distribution in the Persian Gulf.

In the study of the long-term salinity response of the Persian Gulf to the climate change and anthropogenic activities, the calibrated and validated numerical model was employed to predict the spatial and temporal salinity variations in the Persian Gulf for the period 2015-2060, with the climate change and anthropogenic activities considered. The model predicted that the salinity in the Persian Gulf would increase with time in the next half-century and there would be some distinctive spatial characteristics of the salinity distribution.

Some features that make the present study distinctive from previous studies include:

- Long-term simulations have been conducted. Different from the majority of previous studies related to the Persian Gulf, which were typically limited in time from hours to a few months, the current study simulated the salinity distribution in the study domain for decades. Therefore, the results can be more convincing in terms of validating the model, and inspecting the long-term characteristics.

- This study evaluated the performance of various schemes. To the author's knowledge, previous numerical studies in this topic used various schemes but emphasis little on the

reason why their schemes were selected. In this thesis, various schemes have been assessed in detail through a practical and large-scale case study.

- This thesis made the first (to the best of our knowledge) numerical prediction of the long-term trend of salinity changes in the study domain under climate change and human activities in the future.

Some important conclusions of the present thesis are:

- The adoption of an appropriate scheme has a crucial impact on the simulation, especially for surface salinity distribution. Therefore, it is necessary to first consider the performance of various schemes prior to applying the model to a practical problem.

- The employed model followed closely the drop and rise of salinity with time, but tended to underestimate the salinity because small desalination plants and biogeochemical processes as well as irregular wind bursts were not taken into account.

- The schemes with the implicit free surface approach had a closer agreement with the WOA13 data as compared to those provided by the schemes with the rigid-lid approximation, possibly because the rigid-lid approximation excluded the free freshwater flux.

- The impact of the momentum methods on the simulated sub-surface salinity distribution was not as large as that for the surface salinity distribution, since the rigid-lid approximation maintained the pressure variation at the upper surface by a force that would be exerted by a rigid lid.

- The impacts of the equation of state and advection algorithm on the results were also susceptible to the momentum method, and vice versa. The mechanism is that the effect of one factor in a system might be offset or magnified by other effects; and this fact can also be explained and quantified by the path analysis model initially developed by Wright (1921).

- The MJWF03 Equation of State, rigid-lid momentum method, and Adams-Bashforth advection algorithm can result in a reduction in computational cost. However, computational efficiency has not been regarded as the primary concern of this project, as

the effects (in terms of accuracy: e.g., by comparing RMSDs) of different schemes were rather obvious.

- The most appropriate scheme in this case study is the scheme with the JMcD Equation of State, implicit free surface approach for solving the momentum equations, and Adams-Bashforth advection algorithm for tracer equations.

- The model deviated farther from the actual measurements at locations with higher latitudes, mainly due to sharp changes in salinity with time.

- The model performed better for sub-surface salinity than for surface salinity because the model is more capable in predicting smoother variations of salinity, and the variation is relatively smoother in sub-surface salinity.

- There are obvious seasonal variations in salinity, as net results of seasonal tidal characteristics, wind, temperature, and so on.

- The salinity is typically higher in shallower regions, probably caused by the accumulation effects and the restriction of water exchange with the ambient waters in these regions.

- In General, the salinity in the Persian Gulf is continually increasing with time during the next half-century about (1.27%), as a result of the climate change and anthropogenic activities.

- The speed of salinity increase in the Persian Gulf is also increasing with time, which can make the problem associated with salinity in this region more and more serious.

- The speed of salinity increase in the Persian Gulf is larger than the average speed in worlds' oceans, which means that the problem associated with salinity in the Persian Gulf will be more serious than the majority of other water bodies.
- Small oscillations related to the trends of salinity variations are more likely to occur at low-latitude and high-longitude regions, mainly because these regions are more influenced by the seawater inflow from the Strait of Hormuz.
- The salinity will constantly be higher near shore than offshore, since there are more human activities and the water is shallower.

- The salinity in the southern Gulf increases faster than that in the northern Gulf during the next half-century, partially due to the spatial distribution of anthropogenic activities and the density-driven processes.
- The salinity at middle-longitude regions increases faster than those at low-longitude and high-longitude regions, as a result of the human activities and seawater inflows.

Suggestions for future work

- In order to conduct reasonable numerical simulations of the long-term balance of salinity in the Persian Gulf, it is necessary to reasonably predict the climate change in the study domain. The projections of temperature and wind corresponding to the four representative concentration pathways were obtained by using a downscaling method, and the average values were used to represent the climate change. This method can generate an "averaged" scenario and predict a general trend of the balance of salinity in the Persian Gulf corresponding to this scenario. In a future work, the four distinctive scenarios can be simulated separately, which can give an idea about the salinity response of the Persian Gulf to each of these scenarios.

- The hydrostatic assumption was used in the present study because a comparison was done which shows that the non-hydrostatic simulation was more time-consuming but produces almost the same results as those produced by the hydrostatic simulation. However, this comparison was done only in a short-term simulation (4 months). It can be useful to check the non-hydrostatic capacity in a long-term simulation, as an effort towards improving the accuracy of long-term numerical simulations.

- A structured grid was used in the present project, and this kind of grid can have many limitations. For example, it cannot correctly represent the boundaries. Therefore, a future study is proposed to adopt unstructured grids.

- The properties of rainfall distributions in the future were assumed to be constant, which might have an adverse impact on the reliability of the numerical prediction. A future study can be done to project the precipitation in the Persian Gulf. Similarly, the evaporation, irregular wind bursts, long-shore currents, storm events, and the salinity of the rivers can also be projected.

- Attribution studies can be conducted to investigate the contributions of some factors (such evaporation, desalination plants, and precipitation) to the salinity variations in the Gulf.
- Regional studies can also be performed using the outputs from the present global study (multi-level simulations).

References

Adcroft, A., Campin, J. M., Dutkiewicz, S., Evangelinos, C., Ferreira, D., Forget, G., ... & Molod, A. (2008). *MITgcm user manual.*

Adcroft, Alistair, *et al.* (2004). *Overview of the formulation and numerics of the MIT GCM.* Proceedings of the ECMWF seminar series on Numerical Methods, Recent developments in numerical methods for atmosphere and ocean modeling.

AHA (American Heart Association): Statistical Primer for Cardiovascular Research (2015). Retrieved from http://circ.ahajournals.org/content/117/13/1732/F2.expansion.html.

Allsop, N. K., Yao. F (2010). *Experiences of hybrid Ocean modeling of the Persian Gulf on the Blue Gene/P.* Retrieved from http://www.hpc.kaust.edu.sa/events/Supercomputing__44___November_2010/posters/KAUST_NKA_SC10.pdf.

Anderson, J. D., & Wendt, J. F. (1995). *Computational fluid dynamics* (Vol. 206). New York: McGraw-Hill.

Artale, V., Sannino, G., Carillo, A., & Ruggiero, V. (2007). *A Regional Ocean Climate Model for the Mediterranean Sea With a Two-way Grid Refinement at the Strait of Gibraltar*. AGU Fall Meeting Abstracts. Vol. 1, p. 0144).

Austin, J.A. (2004). Estimating effective longitudinal dispersion in the Chesapeake Bay. *Estuarine, Coastal and Shelf Science,* 60, 359-368.

Badri, M. A., Wilders, P., & Azimian, A. R. (2010). *Flow estimation for the Persian Gulf using a kelvin wave expansion*. Delft University of Technology.

Becker, J. J., D. T. Sandwell, W. H. F. Smith, J. Braud, B. Binder, J. Depner, D. Fabre, J. Factor, S. Ingalls, S-H. Kim, R. Ladner, K. Marks, S. Nelson, A. Pharaoh, R. Trimmer, J. Von Rosenberg, G. Wallace, P. Weatherall., *Global Bathymetry and Elevation Data at 30 Arc Seconds Resolution*. SRTM30_PLUS, Marine Geodesy, 32:4, 355-371, 2009.

Bolton, D. (1980). *The computation of equivalent potential temperature.* Monthly weather review, 108(7), 1046-1053.

Bryan, K. (1969). *A numerical method for the study of the circulation of the world ocean*. Journal of Computational Physics, 4(3), 347-376.

Bryman, A., & Cramer, D. (1994). *Quantitative data analysis for social scientists (rev*. Taylor & Frances/Routledge.

CATDS. Salinity Expert Center: Sea Surface Salinity (2015). Retrieved from http://www.salinityremotesensing.ifremer.fr/sea-surface-salinity/definition-and-units

Cavalcante, G. H., Kjerfve, B., Feary, D. A., Bauman, A. G., & Usseglio, P. (2011). *Water currents and water budget in a coastal megastructure, Palm Jumeirah lagoon, Dubai, UAE*. Journal of Coastal Research, 27(2), 384-393.

Chao, S. Y., Kao, T. W., & Al-Hajri, K. R. (1992). *A numerical investigation of circulation in the Arabian Gulf*. *Journal of Geophysical Research: Oceans (1978–2012)*, *97*(C7), 11219-11236.

Chang, Y. S., Özgökmen, T. M., Peters, H., & Xu, X. (2008). *Numerical simulation of the Red Sea outflow using HYCOM and comparison with REDSOX observations*. Journal of Physical Oceanography, 38(2), 337-358.

Chu, W. S., Barker, B. L., & Akbar, A. M. (1988). *Modeling tidal transport in the Arabian Gulf*. Journal of Waterway, Port, Coastal, and Ocean Engineering,114(4), 455-471.

Dawoud, M. A. (2012). *Environmental impacts of seawater desalination: Arabian Gulf case study*. International Journal of Environment and Sustainability (IJES),1(3).

Di Iorio, D., & Castelao, R. M. (2013). The dynamical response of salinity to freshwater discharge and wind forcing in adjacent estuaries on the Georgia coast. *Oceanography*, *26*(3), 44-51.

Dolgopolova, E. N., & Isupova, M. V. (2010). Classification of estuaries by hydrodynamic processes. *Water resources*, *37*(3), 268-284.

Dukowicz, J. K., & Smith, R. D. (1994). *Implicit free surface method for the Bryan Cox Semtner ocean model*. Journal of Geophysical Research: Oceans (1978–2012), 99(C4), 7991-8014.

Durran, D. R. (1991). *The Third-Order Adams-Bashforth Method: An Attractive Alternative to Leapfrog Time Differencing*. Mon. Wea. Rev., 119, 702–720.

Elliott, M., & McLusky, D. S. (2002). *The need for definitions in understanding estuaries*. Estuarine, Coastal and Shelf Science, 55(6), 815-827.

Elhakeem, A., & Elshorbagy, W. (2013). *Evaluation of the long-term variability of seawater salinity and temperature in response to natural and anthropogenic stressors in the Arabian Gulf*. *Marine pollution bulletin*, *76*(1), 355-359.

Elshorbagy, W., Azam, M. H., & Taguchi, K. (2006). *Hydrodynamic characterization and modeling of the Arabian Gulf*. Journal of waterway, port, coastal, and ocean engineering, 132(1), 47-56.

Emery, K. O. (1956). *Sediments and water of Persian Gulf*. *AAPG Bulletin*,*40*(10), 2354-2383.

Environment Canada: Weather. (2015). Retrieved from http://weather.gc.ca/verification/scores/rmse_e.html

Feistel, R., & Hagen, E. (1995). *On the GIBBS thermodynamic potential of seawater*. Progress in Oceanography, 36(4), 249-327.

Fernández, V., Dietrich, D. E., Haney, R. L., & Tintoré, J. (2005). *Mesoscale, seasonal and interannual variability in the Mediterranean Sea using a numerical ocean model.* Progress in Oceanography, 66(2), 321-340.

Ferziger, J. H., & Perić, M. (2002). *Computational methods for fluid dynamics* (Vol. 3, pp. 196-200). Berlin: Springer.

Fofonoff, N.P., Millard, R.C.,1983. *Algorithms for computation of fundamental properties of seawater*. Unesco Tech. Pap. Mar. Sci. 44, 29.

Fowler, H. J., Blenkinsop, S., & Tebaldi, C. (2007). Linking climate change modeling to impacts studies: recent advances in downscaling techniques for hydrological modeling. *International Journal of Climatology*, *27*(12), 1547-1578.

Georgiou, I. Y., McCorquodale, J. A., Schindler, J., Retana, A. G., FitzGerald, D. M., Hughes, Z., & Howes, N. (2009). *Impact of multiple freshwater diversions on the salinity distribution in the Pontchartrain Estuary under tidal forcing.*Journal of Coastal Research, 59-70.

Gisen, J.I.A, Savenije, H.H.G., Nijzink, R.C., and Wahab, A.K.A. (2014). Testing a 1-D Analytical Salt Intrusion Model and its Predictive Equations in Malaysian Estuaries. *Hydrological Sciences Journal*, DOI: 10.1080/02626667.2014.889832.

Gning, N., Le Loc'h, F., Thiaw, O. T., Aliaume, C., & Vidy, G. (2010). *Estuarine resources use by juvenile Flagfin mojarra in an inverse tropical estuary (Sine Saloum, Senegal).*Estuarine, Coastal and Shelf Science, 86(4), 683-691.

Griffies, S. M., Pacanowski, R. C., Schmidt, M., & Balaji, V. (2001). *Tracer conservation with an explicit free surface method for z-coordinate ocean models.* Monthly Weather Review, 129(5), 1081-1098.

Griffiths, D. V., & Smith, I. M. (2006). *Numerical methods for engineers*. CRC press.

Hassanzadeh, S., Hosseinibalam, F., & Rezaei-Latifi, A. (2011). Numerical modelling of salinity variations due to wind and thermohaline forcing in the Persian Gulf. *Applied Mathematical Modelling*, *35*(3), 1512-1537.

Howarth, R., Chan, F., Conley, D. J., Garnier, J., Doney, S. C., Marino, R., & Billen, G. (2011). *Coupled biogeochemical cycles: eutrophication and hypoxia in temperate estuaries and coastal marine ecosystems.* Frontiers in Ecology and the Environment, 9(1), 18-26.

IS (Inside Science, 2015). Retrieved from http://www.insidescience.org/content/human-activity-changing-ocean-salt-levels/890

Jackett, D. R., & Mcdougall, T. J. (1995). *Minimal adjustment of hydrographic profiles to achieve static stability*. Journal of Atmospheric and Oceanic Technology, 12(2), 381-389.

Jackett, D. R., McDougall, T. J., Feistel, R., Wright, D. G., & Griffies, S. M. (2006). *Algorithms for density, potential temperature, conservative temperature, and the freezing temperature of seawater*. Journal of Atmospheric and Oceanic Technology, 23(12), 1709-1728.

Janekovic, I., Sikiric, M. D., Tomazic, I., & Kuzmic, M. (2010). *Hindcasting the Adriatic Sea surface temperature and salinity: A recent modeling experience*.Geofizika, 27(2), 85-100.

Johns, W. E., Yao, F., Olson, D. B., Josey, S. A., Grist, J. P., & Smeed, D. A. (2003). *Observations of seasonal exchange through the Strait of Hormuz and the inferred heat and freshwater budgets of the Persian Gulf*. Journal of Geophysical Research: Oceans (1978–2012), 108(C12).

Kämpf, J., & Ellis, H. (2014). *Hydrodynamics and Flushing of Coffin Bay, South Australia: A Small Tidal Inverse Estuary of Interconnected Bays.* Journal of Coastal Research

Kappus, U., Bleek, J.M., Blair, S.H (1978). *Rainfall frequencies for the Persian Gulf coast of Iran.*

Killworth, P. D., Webb, D. J., Stainforth, D., & Paterson, S. M. (1991). *The development of a free-surface Bryan-Cox-Semtner ocean model*. Journal of Physical Oceanography, 21(9), 1333-1348.

Kuijper, K., & Van Rijn, L. C. (2011). A*nalytical and numerical analysis of tides and salinities in estuaries; part II: salinity distribution in prismatic and convergent tidal channels*. Ocean Dynamics, 61(11), 1743-1765.

Large, W. G., McWilliams, J. C., & Doney, S. C. (1994). Oceanic vertical mixing: A review and a model with a nonlocal boundary layer parameterization. *Reviews of Geophysics*, *32*(4), 363-403.

Lax, P., & Wendroff, B. (1960). *Systems of conservation laws.* Communications on Pure and Applied mathematics, 13(2), 217-237.

Levitus, S., Antonov, J. I., Baranova, O. K., Boyer, T. P., Coleman, C. L., Garcia, H. E., ... & Zweng, M. M. (2013). *The World Ocean Database*. Data Science Journal, 12(0), WDS229-WDS234.

Lewis, R. E., & Uncles, R. J. (2003). Factors affecting longitudinal dispersion in estuaries of different scale. *Ocean Dynamics*, *53*(3), 197-207.

Liu, W. C., Hsu, M. H., Kuo, A. Y., & Hung, H. Y. (2007). *Effect of channel connection on flow and salinity distribution of Danshuei River estuary.* Applied mathematical modeling, 31(6), 1015-1028.

Liu, J.B., & Bao, Y. (2011). *Spacial distribution of salinity and the mechanism of saltwater intrusion in the Modaomen water channel of pear river estuary.* AIP Conference Proceedings, 2011, Vol.1376, pp.405-407.

Machalinska-Murawska, J., & Szydłowski, M. (2014). *Lax-Wendroff and McCormack Schemes for Numerical Simulation of Unsteady Gradually and Rapidly Varied Open Channel Flow.* Archives of Hydro-Engineering and Environmental Mechanics, 60(1-4), 51-62.

Marshall, J., & Plumb, R. A. (1965). *Atmosphere, ocean and climate dynamics: an introductory text* (Vol. 8). Academic Press.

Marshall, J., Hill, C., Perelman, L., Adcroft, A. (1997). *Hydrostatic, quasi-hydrostatic and nonhydrostatic ocean modeling.* J. Geophys. Res. 102, C3 5,733–5,752

McDougall, T. J., Jackett, D. R., Wright, D. G., & Feistel, R. (2003). *Accurate and computationally efficient algorithms for potential temperature and density of seawater. Journal of Atmospheric and Oceanic Technology*, *20*(5), 730-741.

McDonald, J. E. (1952). *The Coriolis Effect*. WH Freeman.

Meinshausen M, Smith SJ, Calvin K, Daniel JS, Kainuma MLT, Lamarque J-F, Matsumoto K, Montzka SA, Raper S, Riahi K et al (2011). The RCP greenhouse gas concentrations and their extensions from 1765 to 2300. Climatic Change. doi: 10.1007/s10584-011-0156-z.

Meshal, A. H., & Hassan, H. M. (1986). *Evaporation from the coastal water of the central part of the Gulf*. Arab Gulf Journal of Scientific Research, 4(2), 649-655.

MIF: Cartesian Coordinates (2015). Retrieved from http://www.mathsisfun.com/data/cartesian-coordinates.html

Mikhailov, V.N., & Gorin, S.L. (2012). *New Definitions, Regionalization, and Typification of River Mouth Areas and Estuaries as Their Parts*. Water Resources, 39 (3): 247-260.

Millero, F.J. 2010. *History of the equation of state of seawater*. Oceanography 23(3):18–33, doi:10.5670/oceanog.2010.21.

NCAR (National Center for Atmospheric Research): Climate Change Scenarios (2015). Retrieved from https://gisclimatechange.ucar.edu/question/63.

Nguyen, D.H., Umeyama, M., Shintani, T. (2012). Importance of geometric characteristics for salinity distribution in convergent estuaries. *Journal of Hydrology*, 449, 1-13.

NWP (Numerical Weather Prediction): vertical resolution and coordinates (2015). Retrieved from http://www.met.tamu.edu/class/metr452/models/2001/vertres.html

Nunes-Vaz, R. A. (2012). *The salinity response of an inverse estuary to climate change & desalination.* Estuarine, Coastal and Shelf Science, 98, 49-59.

NOAA: Acoustic Doppler Current Profiler. (2015). Retrieved from http://oceanexplorer.noaa.gov/technology/tools/acoust_doppler/acoust_doppler.html

OI (Ocean Instruments): Acoustic Doppler Current Profiler. (2015). Retrived from http://www.whoi.edu/instruments/viewInstrument.do?id=819

Oliver, M. A., & Webster, R. (1990). Kriging: a method of interpolation for geographical information systems. *International Journal of Geographical Information System*, *4*(3), 313-332.

Perrone, T. J. (1979).*Winter Shamal in the Persian Gulf*. Technical Rep. 79–06, Naval Environment Prediction Research Facility, Monterey, Calif.

Peterson, R.N. *et al.* (2008). Determination of transport rates in the Yellow River-Bohai Sea mixing zone via natural geochemical tracers. *Continental Shelf Research*, 28, 2700-2707.

Prasuhn, A. L. (1992). *Fundamentals of hydraulic engineering* (1st. ed.). New York: Oxford University Press.

Pritchard, D. W. (1952). *Estuarine hydrography.* Advances in geophysics, 1, 243.

Pritchard, D. W. (1967). What is an estuary: Physical viewpoints. *Estuaries,* Washington, D. C.

Privett, D. W. (1959). *Monthly charts of evaporation from the N. Indian Ocean (including the Red Sea and the Persian Gulf).* Quarterly Journal of the Royal Meteorological Society, 85(366), 424-428.

Post, V. E. A. (2012). *Electrical conductivity as a proxy for groundwater density in coastal aquifers.* Groundwater, 50(5), 785-792.

Pous, S., Carton, X., & Lazure, P. (2013). *A process study of the wind-induced circulation in the Persian Gulf. Open Journal of Marine Science*, *3*, 1.

QG (Queensland Government): Salinity (2015). Retrieved from https://www.qld.gov.au/environment/land/soil/salinity/impacts/

Reynolds, M. (1993). *Physical oceanography of the Gulf, Strait of Hormuz, and the Gulf of Oman—Results from the Mt Mitchellb expedition.* Marine Pollution Bulletin, 27, 35-59.

Ross, D. A., & Stoffers, P. (1978). *General data on bottom sediments including concentration of various elements and hydrocarbons in the Persian Gulf and Gulf of Oman.* Woods Hole Oceanographic Institution Technical Report, 78-39.

Sadrinasab, M., & Kämpf, J. (2004). *Three dimensional flushing times of the Persian Gulf.* Geophysical research letters, 31(24).

Sadrinasab, M., & Poorkiani, K. (2011). *A Three-dimensional Numerical Modeling of Contaminant Dispersion from Arvand Rood River into the Persian Gulf.* Journal of the Persian Gulf, 2(4), 19-26.

Savenije, H.G. (2012). *Salinity and Tides in Alluvial Estuaries*. Delft: The Netherlands.

Sea-Bird: CTD Basics (2015). Retrieved from http://www.seabird.com/document/an93-ctd-basics

Shaha, D.C., and Cho, Y. K. (2011). Determination of spatially varying Van der Burgh's coefficient from estuarine parameter to describe salt transport in an estuary. *Hydrol. Earth Syst. Sci*., 15, 1369-1377.

Shaughnessy, E. J. (2010). Introduction to fluid mechanics.

Shirkhani, H., Seidou, O., Mohammadian, A., Qiblawey, H. (2015). Projection of Significant Wave Height in a Coastal Area under RCPs Climate Change Scenarios, *Natural Hazards*

Review, ASCE, 2015,

Singh, G., Kanwar, V., & Bhatia, S. (2013). *Exponentially Fitted Variants of the Two-Step Adams-Bashforth Method for the Numerical Integration of Initial Value Problems*. Applications & Applied Mathematics, 8(2).

Smith, R. D., Dukowicz, J. K., & Malone, R. C. (1992). *Parallel ocean general circulation modeling.* Physica D: Nonlinear Phenomena, 60(1), 38-61.

Stenström, P. (2004). *Hydraulics and mixing in the Hudson River estuary: A numerical model study of tidal variations during neap tide conditions.* Journal of Geophysical Research: Oceans (1978–2012), 109(C4).

Stillinger, F. H., & Rahman, A. (1974). *Molecular dynamics study of liquid water under high compression.* The Journal of Chemical Physics, 61(12), 4973-4980.

Sun, S., Bleck, R., Rooth, C., Dukowicz, J., Chassignet, E., & Killworth, P. (1999). *Inclusion of thermobaricity in isopycnic-coordinate ocean models*.Journal of Physical Oceanography, 29(10), 2719-2729.

TET (The Engineering ToolBox): Salinity of Water (2015). Retrived from http://www.engineeringtoolbox.com/water-salinity-d_1251.html

Thoma, M., Grosfeld, K., Smith, A. M., & Mayer, C. (2010). *A comment on the Equation of State and the freezing point equation with respect to subglacial lake modeling*. Earth and Planetary Science Letters, 294(1), 80-84.

Thoppil, P. G., & Hogan, P. J. (2010). *A modeling study of circulation and eddies in the Persian Gulf.* Journal of Physical Oceanography, 40(9), 2122-2134.

TOH (The Ozone Hole): The Coriolis Effect (2015). Retrieved from http://www.theozonehole.com/coriolis.htm

Van Vuuren, D. P., Edmonds, J., Kainuma, M., Riahi, K., Thomson, A., Hibbard, K., & Rose, S. K. (2011). The representative concentration pathways: an overview. *Climatic Change*, *109*, 5-31.

USEPA (United States Environmental Protection Agencey): Estuarine Science (2015). Retrieved from http://omp.gso.uri.edu/ompweb/doee/science/physical/chsal1.htm.

Wang, F., & Xu, Y. J. (2008). *Development and application of a remote sensing-based salinity prediction model for a large estuarine lake in the US Gulf of Mexico coast.* Journal of hydrology, 360(1), 184-194.

Wolfram Mathworld: Spherical Coordinates (2015). Retrieved from http://mathworld.wolfram.com/SphericalCoordinates.html

WOA (World Ocean Atlas, 2009). National Oceanographic Data Center (NODC). Retrived from http://www.nodc.noaa.gov/

WOA13 (World Ocean Atlas, 2013). National Oceanographic Data Center (NODC). Retrived from http://www.nodc.noaa.gov/

Wright, S. (1921). *Correlation and causation.* Journal of agricultural research,20(7), 557-585.

Wright, D. G. (1997). *An equation of state for use in ocean models: Eckart's formula revisited.* Journal of Atmospheric and Oceanic Technology, 14(3), 735-740.

Xuan, J. L., Huang, D., Zhou, F., Zhu, X. H., & Fan, X. (2012). *The role of wind on the detachment of low salinity water in the Changjiang Estuary in summer.*Journal of Geophysical Research: Oceans (1978–2012), 117(C10).

Yao, F., & Johns, W. E. (2010). *A HYCOM modeling study of the Persian Gulf: 1. Model configurations and surface circulation.* Journal of Geophysical Research: Oceans (1978–2012), 115(C11).

Yelland, M., & Taylor, P. K. (1996). Wind stress measurements from the open ocean. *Journal of Physical Oceanography*, *26*(4), 541-558.

Zhao, B., & Zhang, B. (2011). *Comparison of different order Adams-Bashforth methods in an atmospheric general circulation model.* Acta Meteorologica Sinica, 25, 754-764.

Zhang, E., Savenije, H. H., Wu, H., Kong, Y., & Zhu, J. (2011). *Analytical solution for salt intrusion in the Yangtze Estuary, China.* Estuarine, Coastal and Shelf Science, 91(4), 492-501.

Appendix 1 Employed Mathematical Tools

A1.1 Root-mean-square Deviation

For the purpose of assessing the performance of the simulations, root-mean-square deviation has been calculated for comparing the simulated data and observational data.

Root-mean-square deviation, also known as root-mean-square error, is a widely used method for measuring the differences between predicted values and observed values. It aggregates the errors produced by estimations for a series of time into one single error so it can serve as a convenient tool for measure of accuracy. It is defined mathematically as (e.g. Environment Canada, 2015):

$$RMSD = \sqrt{\frac{1}{N}\sum_{i=1}^{N}(F_i - o_i)^2} \tag{42}$$

where

$RMSD$	=	Root-mean-square Deviation
F_i	=	the forecast values of the parameter in question;
o_i	=	the corresponding verifying value (observed or analysed);
N	=	the number of verifying points (grid points or observations) in the verification area.

The results range from zero to infinity, and a result of zero indicates that the prediction is perfect. It can be concluded from the equation above that the Root-mean-square deviation is a kind of average error, which is weighted based on the square of the error. The root-mean-square deviation can show the average magnitude of the forecast error, but cannot point out the direction the error. Large errors have a stronger impact on the root-mean-square deviation than smaller errors, as the squared quantity is employed in this method.

There are also some other parameters for measuring errors between predictions and observations based on root-mean-square deviation. The normalized root-mean-square deviation can be expressed as:

$$NRMSD = \frac{RMSD}{o_{\max} - o_{\min}} \tag{43}$$

where

o_{max} = the largest verifying values;

o_{min} = the smallest verifying values.

The coefficient of variation of the root-mean-square error is defined as:

$$CV(RMSD) = \frac{RMSD}{\overline{o}} \tag{44}$$

where

CV = coefficient of variation;

$\overline{o}$ = the mean of the verifying values.

A1.2 Path Analysis

The impact of a scheme on the simulated salinity in the Persian Gulf will change when combined with other schemes. For example, the equation of state would have a smaller impact on the accuracy of simulated results when combined with the rigid-lid approximation. The mechanism for this is that the effect of one factor in a system on the errors might be offset or magnified by other effects. Moreover, this phenomenon can also be explained and quantified by the path analysis model developed by Wright (1921), where the independent variables have both direct and indirect (through other variables) effects on the dependent variables; for example, the equation of state has both a direct effect and an indirect (through the momentum method and advection algorithm) effect on the accuracy of the results, and in total, the overall effect is the summation of these direct and indirect effects.

Path analysis is basically a straightforward extension of multiple regressions, and it can be explained by the following example given by Bryman and Cramer (1990).

Figure A1-1 indicates that age has a direct impact on job satisfaction. Besides, age also has indirect impacts on job satisfaction through autonomy and income: it affects income, which can affect job satisfaction directly; it affects autonomy, which can affect job satisfactory directly; it affects autonomy, which can affect income which affects job satisfaction.

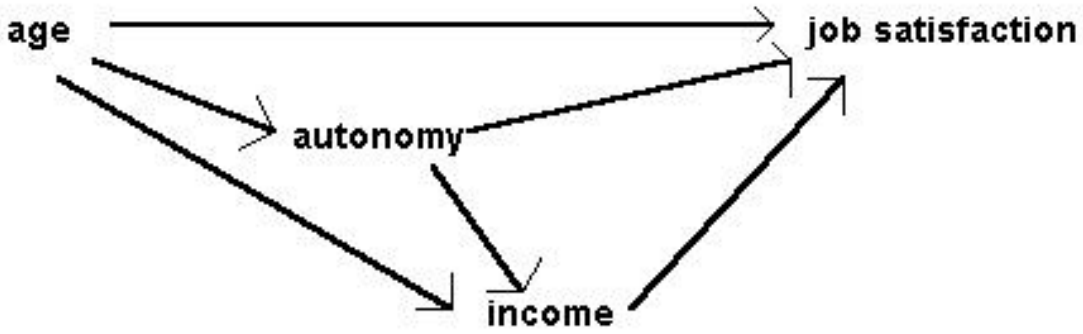

Figure A1-1. Diagram for path analysis in the job survey (Bryman & Cramer, 1990)

Therefore these relationships can be described as:

$$\begin{aligned} J_s &= \alpha_{11}A_{ge} + \alpha_{12}A_{uto} + \alpha_{13}I_{nc} + e_1 \\ I_{nc} &= \alpha_{21}A_{ge} + \alpha_{22}A_{uto} + e_2 \\ A_{uto} &= \alpha_{31}A_{ge} + e_3 \end{aligned} \tag{45}$$

where

J_s = job satisfaction;

A_{ge} = age;

A_{uto} = autonomy;

I_{nc} = income;

α = path coefficients;

e = errors;

Using regression analyses, the path coefficients can be calculated:

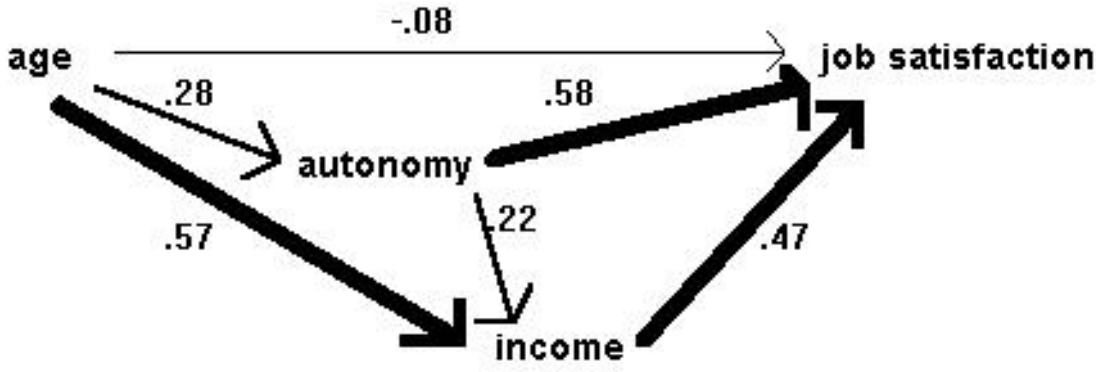

Figure A1-2. Diagram for path analysis in the job survey with path coefficients (Bryman & Cramer, 1990)

The overall impact of one variable on another can be calculated by summing the direct effect and indirect effects. For example, to calculate the overall impact of age on job satisfaction (Figure A1-2):

Direct effect: -0.8

Indirect effect 1 (through income): $0.57 \times 0.47 = 0.26$;

Indirect effect 2 (through autonomy): $0.28 \times 0.58 = 0.16$;

Indirect effect 3 (through autonomy – income): $0.28 \times 0.22 \times 0.47 = 0.03$;

Therefore, the total effect of age on job satisfaction = $-0.08 + 0.26 + 0.16 + 0.03 = 0.37$.

A1.3 Linear Regression

Linear regression is a method of modeling the relationship between a scalar dependent variable and one or more independent variables. When there is only one independent variable, the method is called simple linear regression. Simple linear regression fits a straight line through the set of points by making the sum of squared residuals of the model the smallest

When there is more than one independent variables, the method is called multiple linear regression (Figure 1-3; AHA, 2015).

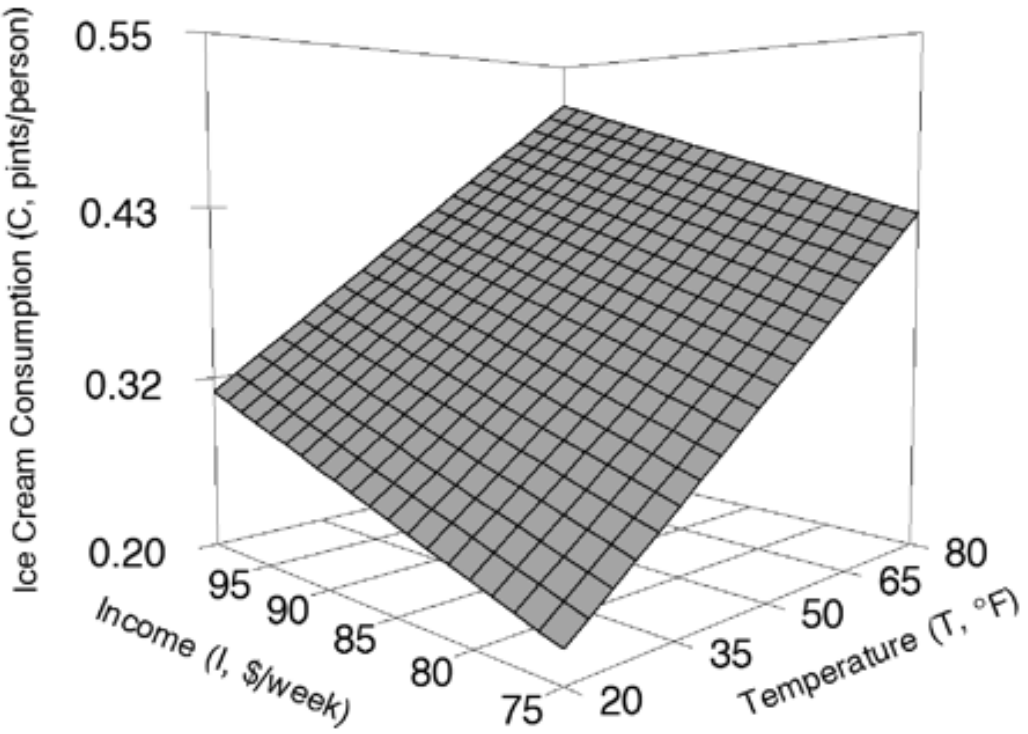

Figure A1-3. An example of three-dimenional plot of a best-fit multiple linear regression plane (AHA, 2015)

Multiple linear regression is a generalization of linear regression, as oppose to simple linear regression, which is a specific case of linear regression. Multiple linear regression can be expressed as:

$$y_i = \alpha_0 + \alpha_1 x_{i1} + \alpha_2 x_{i2} + \cdots + \alpha_n x_{in} + e_i \tag{46}$$

where

y_i = i th observation of the dependent variable;

$\alpha_0, \alpha_1, \alpha_2, \cdots \alpha_n$ = coefficients to be fitted;

x_{ij} = i th observation of the j th independent variable ;
$j = 1, 2, \cdots n$;

e_i = the i th independent identically distributed normal error.

Appendix 2 More Details on the Equations of Fluid Motions

A2.1 Equations of Fluid Motions in Lagrangian Form

Continuity equation:

$$\frac{D\rho}{Dt} + \rho \nabla \cdot \vec{v} = 0 \tag{47}$$

where (D/Dt) is the total derivative (also called variously the "Lagrangian derivative", the "substantial derivative", or the "material derivative"); ρ denotes the density; $\vec{v} = (u, v, w)$ represents the velocity; $\nabla \cdot \vec{v}$ is the divergence of the velocity.

Momentum equations (x, y, z components):

$$\rho \frac{Du}{Dt} = -\frac{\partial p}{\partial x} + \frac{\partial \tau_{xx}}{\partial x} + \frac{\partial \tau_{yx}}{\partial y} + \frac{\partial \tau_{zx}}{\partial z} + \rho f_x \tag{48}$$

$$\rho \frac{Dv}{Dt} = -\frac{\partial p}{\partial y} + \frac{\partial \tau_{xy}}{\partial x} + \frac{\partial \tau_{yy}}{\partial y} + \frac{\partial \tau_{zy}}{\partial z} + \rho f_y \tag{49}$$

$$\rho \frac{Dw}{Dt} = -\frac{\partial p}{\partial z} + \frac{\partial \tau_{xz}}{\partial x} + \frac{\partial \tau_{yz}}{\partial y} + \frac{\partial \tau_{zz}}{\partial z} + \rho f_z \tag{50}$$

where p is the pressure; τ_{ij} denotes a stress in the j direction exerted on a plan perpendicular to the i axis; $\vec{f} = (f_x, f_y, f_z)$ denotes the body force per unit mass acting on the fluid element.

Energy equation:

$$\begin{aligned} \rho \frac{D}{Dt}(e + \frac{V^2}{2}) = \rho \dot{q} &+ \frac{\partial}{\partial x}(k_T \frac{\partial T}{\partial x}) + \frac{\partial}{\partial y}(k_T \frac{\partial T}{\partial y}) + \frac{\partial}{\partial z}(k_T \frac{\partial T}{\partial z}) \\ &- \frac{\partial (up)}{\partial x} - \frac{\partial (vp)}{\partial y} - \frac{\partial (wp)}{\partial z} + \frac{\partial (u\tau_{xx})}{\partial x} \\ &+ \frac{\partial (u\tau_{yx})}{\partial y} + \frac{\partial (u\tau_{zx})}{\partial z} + \frac{\partial (v\tau_{xy})}{\partial x} + \frac{\partial (v\tau_{yy})}{\partial y} \\ &+ \frac{\partial (v\tau_{zy})}{\partial z} + \frac{\partial (w\tau_{xz})}{\partial x} + \frac{\partial (w\tau_{yz})}{\partial y} + \frac{\partial (w\tau_{zz})}{\partial z} + \rho \vec{f} \cdot \vec{v} \end{aligned} \tag{51}$$

where e is the internal energy per unit mass; $V^2/2$ represents the kinetic energy per unit mass; $\dot{q}$ refers to the rate of volumetric heat addition per unit mass; k_T is the thermal conductivity.

A2.2 A Derivation of the Coriolis Term

The Coriolis term can be derived in various ways, and its derivation is presented here through an example shown in Figure A2-1.

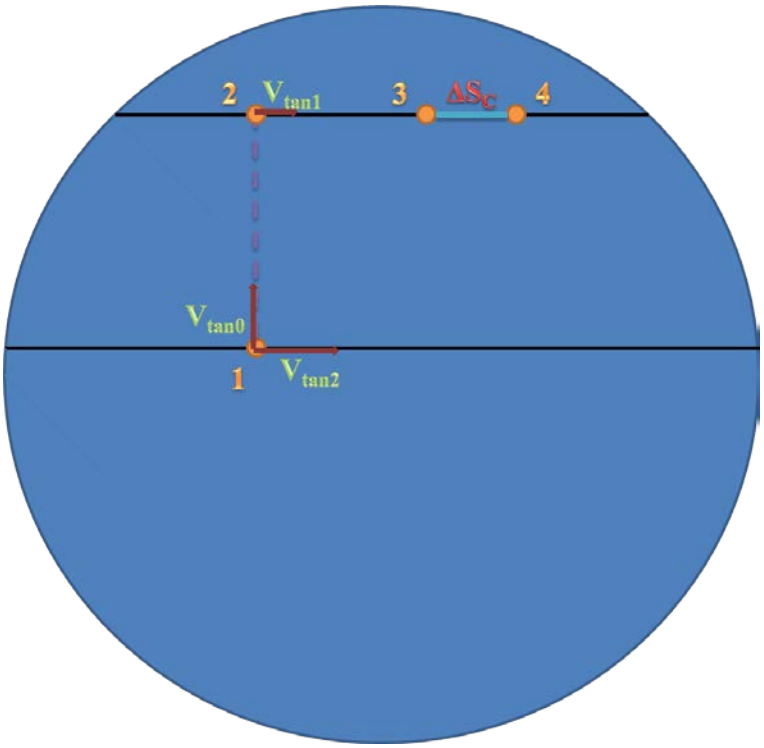

Figure A2-1. A Derivation of the Coriolis Term

An object at Location 1 has an initial velocity $v_{\tan 0}$ towards Location 2. If the Earth did not rotate, the object would arrive at Location 2. However, because of the Earth's rotation, the object also has an initial velocity component $v_{\tan 2}$, and the tangential velocity at Location 2 is $v_{\tan 1}$.

In a rotating object, the tangential speed can be calculated from the frequency of the rotation:

$$v_{\tan} = r_{dist}\omega_{ang} \tag{52}$$

where $v_{\tan}$ represents tangential speed, r_{dist} is the distance from the axis, and ω_{ang} indicates the angular speed. For the Earth, ω_{ang} is a constant, and therefore the tangential speed is in direct proportion to the distance from the axis. Thus, $v_{\tan 2}$ is larger than $v_{\tan 1}$.

If $v_{\tan 2}$ were equal to $v_{\tan 1}$, both the object and Location 2 would arrive at Location 3 after the object reached the line where Location 2 was; however, since $v_{\tan 2}$ is larger than $v_{\tan 1}$, instead of Location 3, the object will arrive at Location 4.

ΔS_C, the distance between Location 4 and Location 3, is caused by the Earth's rotation, and it can be assumed that:

$$\Delta S_C = \frac{1}{2} a_C t^2 \tag{53}$$

where a_C is the acceleration assumed.

In fact, ΔS_C is caused by the difference of the velocities, and it can be expressed as:

$$\Delta S_C = v_{\tan 2} t - v_{\tan 1} t \tag{54}$$

According to this equation and $r_{dist2} - r_{dist1} = v_{\tan 0} t$:

$$\Delta S_C = r_{dist2}\omega_{ang} t - r_{dist1}\omega_{ang} t = (r_{dist2} - r_{dist1})\omega_{ang} t = v_{\tan 0}\omega_{ang} t^2 \tag{55}$$

Therefore:

$$\Delta S_C = \frac{1}{2} a_C t^2 = v_{\tan 0}\omega_{ang} t^2 \Rightarrow a_C = 2\omega_{ang} v_{\tan 0} \tag{56}$$

This equation shows the scalar form of the acceleration caused by the Coriolis Effect, and it can also be extended to general and written in vector form:

$$\vec{a}_C = -2\vec{\Omega}\vec{v} \tag{57}$$

where $\vec{a}_C$ is the acceleration vector due to the Coriolis Effect;

$\vec{\Omega}$ is the Earth's rotation:

$$\vec{\Omega} = \omega_{ang} \begin{pmatrix} 0 \\ \cos\varphi \\ \sin\varphi \end{pmatrix} \tag{58}$$

in which φ represents the latitude.

$\vec{v}$ is the velocity:

$$\vec{v} = \begin{pmatrix} u \\ v \\ w \end{pmatrix} \tag{59}$$

Combining these equations, the following equation can be obtained:

$$\vec{a}_c = -2\omega \begin{pmatrix} w\cos\varphi - v\sin\varphi \\ u\sin\varphi \\ u\cos\varphi \end{pmatrix} \tag{60}$$

The vertical component of the Coriolis acceleration is quite small compared to the gravity, and it is thus generally ignored. Besides, a parameter can be used for the expression of the Coriolis acceleration and it is called Coriolis parameter, which is:

$$f = 2\omega\sin\varphi \tag{61}$$

Therefore, the Coriolis acceleration can be expressed as:

$$\vec{a}_c = f \begin{pmatrix} v \\ -u \end{pmatrix} \tag{62}$$

Appendix 3 Further Review on Previous Studies and Methodologies

A3.1 Relevant Instrument

CTD

A CTD (also called “Sonde”) is an instrument measures conductivity, temperature and depth Figure A3-1). In fact, all CTDs measure pressure rather than depth. A CTD contains a set of sensors, and these sensors generally scan at a rate of 24 Hz.

Figure A3-1. CTD in the University of Ottawa

The data obtained by CTD can be manipulated to calculate salinity, density, sound velocity, and other parameters, and auxiliary sensors can be incorporated into CTD to measure other parameters in a water body, such as dissolved oxygen, altimeter, and PH. Depth measurements are calculated from measurements of hydrostatic pressure, and salinity is calculated from electrical conductivity. The CTD can be lowered to a certain depth, and this depth is determined by the metal used for housing the sensors.

There are mainly three types of CTDs, namely, profiling CTDs, moored CTDs and thermosalinographs (Sea-Bird Scientific, 2015).

A profiling CTD measures the parameters of interest as it travels through the water. Commonly, the instrument is lowered over the side of a ship with a winch to scan a vertical column of water. A cage is usually used to place the profiling CTD package to protect the instrument from collision with the side of the ship.

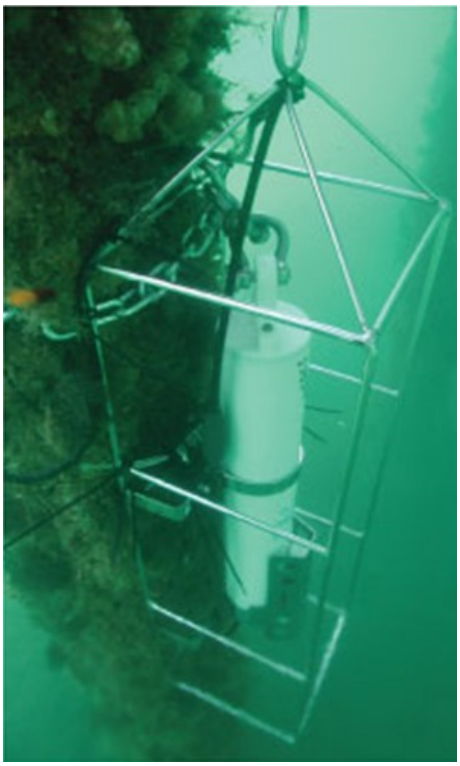

Figure A3-2. A CTD mounted to a pier (Sea-Bird Scientific, 2015)

A moored CTD measures water parameters in one fixed location for a certain period of time (Figure A3-2). The main purpose of using this type of CTD is to get a time series data that can reveal information about temporal or seasonal variations in the water, incursion of pollutants into the area, and so on.

A thermosalinograph is a shipboard CTD that has no pressure sensor. It is used to collect information about the sea surface, typically in flow-through systems operating continuously throughout a cruise.

ADCP

An Acoustic Doppler Current Profiler (ADCP) is an instrument measuring how fast water is moving across a column of water (OI, 2015). It can be used in various ways; for example, in shallow areas, it can be anchored to the seafloor and both the current speed at the bottom and at equal intervals all the way up to the surface can be measured; it can also be used in deep areas, where it can be lowered on a cable from the surface. It is a hydro-acoustic current meter similar to sonar, and it uses the Doppler effect of sound waves scattered back from particles within the column of water to measure the current velocities.

Figure A3-3. ADCP in Qater University

The ADCP emits a sequence of high frequency pulses of sound that scatter off of moving particles in the water column. The frequency of the return signal bounced back to the ADCP is different, based on whether the particles are moving toward or away from the sound source. Sound waves that hit particles far from the profiler take longer to come back, therefore the there is a difference of time that the waves take to bounce back, and by measuring the time and Doppler shift, the profiler is enabled to measure current speed at various depths with each series of pings.

An ADCP typically has four acoustic transducers; these transducers emit and receive acoustical pulses from four different directions; using trigonometric relations to convert the return signal

from the transducers to earth coordinates, the direction of the current can be calculated (NOAA, 2015).

Similar to CTD, an ADCP can either measure water velocities as it moves through the water (Figure A3-3) or be mounted for an extended period of time (Figure A3-4).

Figure A3-4. A driver dyploying a bottom-mounted acoustic doppler current profiler to investigate the hydrodynamics of coral reef systems (NOAA, 2015)

GPS Receiver

GPS refers to the global positioning system, which is a space-based satellite navigation system that provides location and time information, which can be obtained by using a GPS receiver. It can be used for military, civil and commercial users; for hydraulic engineers or oceanographers, a GPS receiver can be integrated with an ADCP to provide the location information Figure A3-5); and the GPS data and ADCP data can be synchronized very well.

Figure A3-5. ADCP-GPS integrated system

A3.2 Analytical Studies and Some Limitations

Analytical Method 1 (Austin, 2004)

A conceptual model based on the salt balance in a turbulent flow can be expressed as:

$$\frac{\partial}{\partial t}(A(x)S(x,t)) + \frac{\partial}{\partial x}(A(x)U(x,t)S(x,t)) = \frac{\partial}{\partial x}(A(x)K_H\frac{\partial S}{\partial x}) \qquad (63)$$

where x is the along-flow coordinate, which is called longitudinal coordinate in this report, with $x = 0$ at the head of the estuary; $A(x)$ is the cross-sectional area; $U(x, t)$ is the stream-wise advection, which is called longitudinal velocity; $S(x, t)$ is the salinity; and K_H is the effective dispersion coefficient, and it is called longitudinal dispersion coefficient in this thesis since this conceptual model is under the one-dimensional assumption.

As can be observed, it is a kind of advection-diffusion model, which can be used for an estuary: the first term in left hand side is temporal term; the second term in left hand side is advective term and the term in right hand side is diffusive term

Austin (2004) utilized the model above, and disregarded the time-varying fact of the salinity term in order to simplify it; the cross-sectional area $A(x)$ was also assumed to be constant in

time; $U(x, t)$ is estimated using $U(x, t) = F(t)\ A(x)\text{-}1$, where $F(t)$ is the estimated freshwater input.

To estimate the longitudinal dispersion coefficient $K_H(x, t)$, Austin integrated Taylor's model from the head of the freshwater-sea confluence ($x = 0$) to a longitudinal position $x = X$ within the confluence:

$$\int_0^X A(x)\frac{\partial S}{\partial t}dx + F(t)S(x)|_{x=X} - F(t)S(x)|_{x=0} = A(x)K_H(x,t)\frac{\partial S}{\partial x}|_{x=X} - A(x)K_H(x,t)\frac{\partial S}{\partial x}|_{x=0} \quad (64)$$

There are two boundary conditions at the head of the estuary (x = 0) can be applied:

$S(x = 0) = 0$, which means the water at the head of the estuary is always fresh, and

$K_H S_x(x = 0) = 0$, which means the diffusive flux of salt through the head of the estuary is zero.

Finally, Austin got their equation as shown below:

$$\int_0^X A(x)\frac{\partial S}{\partial t}dx + F(t)S(X) = A(x)K_H(X,x)\frac{\partial S}{\partial x} \quad (65)$$

where:

$A(x)$	=	Cross-sectional Area;
S	=	Salinity;
t	=	Time;
$F(t)$	=	Estimated Freshwater Input;
$K_H(X,t)$	=	Effective Dispersion Coefficient.

The equation can be solved on a consistent space-time grid.

Using the data on the salinity, $K_H(x, t)$ can be determined using a least squares method, either as a function of space or of time, by assuming that $K_H(x, t)$ is constant in the other dimension. $K_H(x, t)$ is a function of both but determining the space-time structure of this value in any statistically significant sense, given the noisy, limited, irregularly spaced data is difficult.

Therefore, Austin proposed two different approaches to solve the equation:

$K_H(x, t)$ is assumed constant in time to produce a spatially dependent estimate of $K_H'(x)$, and

$K_H(x, t)$ is assumed constant in space to produce a temporally dependent estimate $K_H'(t)$.

Austin stated that this method is useful for better understanding distribution of other tracers within the bay, as well as providing another metric against which numerical models should be measured.

Analytical Method 2 (Shaha & Chao, 2011)

Lewis and Uncles (2003) used the terminology in their study: the tidally averaged residual flux of salt, F_{res}, across any section of an estuary, which is the difference between the salt transported seawards by the freshwater flow and that "diffused" landward by the remaining dispersive processes. This transport can be expressed as:

$$F_{res}(x) = Rs - AK_{xe}\frac{ds}{dx} \tag{66}$$

where

$F_{res}(x)$ = The flux at a section located a distance x from the head of the estuary;

R = The freshwater inflow to the system;

A = The tidal average area of the cross-section;

K_{xe} = The longitudinal dispersion coefficient;

ds/dx = The local gradient in the cross-sectionally averaged;

s = The tidal mean salinity.

Lewis and Uncles (2003) conjectured that over a period of time long enough to smooth out variations in the river flow, tidal range and wind forcing, an estuary attains a steady state such that there is no net flux of salt. This expression describes the variation of the salinity along a well-mixed estuary. The form of this distribution is of fundamental interest as the salinity acts as a tracer, indicating the processes that inter-mix seawater with the freshwater supplied from riverine inputs.

Savenije (2005) made three assumptions:

$$\frac{1}{T}\int_0^T Q_t \frac{\partial s}{\partial x} dt \approx 0 \tag{67}$$

where T is the period, Q is the discharge, t represents tidal, s is the salinity, x is the longitudinal dispersion, t is the time.

$$\frac{1}{T}\int_0^T Q_f \frac{\partial s}{\partial x} dt \approx Q_f \frac{\partial s_{TA}}{\partial x} \tag{68}$$

where f represents freshwater, and TA represents tidal averaged.

$$\frac{1}{T}\int_0^T \frac{\partial}{\partial x}(AD\frac{\partial s}{\partial x})dt \approx \frac{\partial}{\partial x}(A_{TA}D_{TA}\frac{\partial s_{TA}}{\partial x}) \tag{69}$$

In which D represents the longitudinal dispersion coefficient.

Then the author integrated the salt balance equation with respect to x by assuming equilibrium between advective and dispersive fluxes under tidal average conditions, to give:

$$Q(S_{TA} - S_f) - A_{TA}D_{TA}\frac{\partial S_{TA}}{\partial x} = 0 \tag{70}$$

where:

Q = The freshwater discharge;

S_{TA} = The tidal average freshwater salinity;

A_{TA} = The tidal average cross-sectional area;

D_{TA} = The longitudinal dispersion coefficient.

This equation can also be used to determine the longitudinal dispersion coefficient under high water slack and low water slack conditions. Shaha (2011) modified the equation above and changed it into the form of equation proposed by Lewis and Uncles. They assumed the salinity S_f of freshwater discharge is zero, this equation can be expressed in general form for the spatially varying dispersion coefficient $D_i(x)$ as follows:

$$D_i(x) = \frac{QS_i(x)/A_i(x)}{\frac{\partial S_i}{\partial x}} \tag{71}$$

where:

i = High Water Slack or Low Water Slack;

Q = Freshwater Input;

$D_i(x)$ = Longitudinal Dispersion Coefficient;

$S_i(x)$ = Salinity;

$A_i(x)$ = Tidal Averaged Cross-sectional Area.

As can be observed, the effective longitudinal dispersion appears to be positively correlated with river discharge at both high water slack and low water slack.

Analytical Method 3 (Savenije, 2012)

Similar to the equation presented in the previous section, Savenije (2012) reorganized the equation:

$$S_i - S_f = -\frac{A}{Q_f} D_i \frac{dS_i}{dx} \tag{72}$$

shere S_i is the salinity at high water slack, low water slack and tidal averaged respectively; S_f is the salinity in freshwater; A is the tidal average cross-sectional area; Q_f is the freshwater discharge; D_i is the dispersion coefficient at high water slack, low water slack and tidal average respectively.

Van der Burgh developed a purely empirical method on the basis of the effective tidal average dispersion under equilibrium conditions. Plotting the longitudinal variation of the effective dispersion against the velocity of the fresh water discharge, he found a direct proportionality:

$$\frac{\partial D}{\partial x} = -K \frac{Q_f}{A} = -KU_f \tag{73}$$

K is the Van der Burgh coefficient, which is mainly obtained through calibration.

$$U_f = \frac{Q_f}{A} \tag{74}$$

The expression is used for high water slack, low water slack, and tidal average:

$$\frac{dD_i}{dx} = -K\frac{Q_f}{A} \tag{75}$$

Combination of the two equations yields:

$$\frac{dS}{S - S_f} = \frac{1}{K}\frac{dD}{D} \tag{76}$$

The subscript *i* has been disregarded for the sake of simplicity, and the integration results in:

$$\frac{S - S_f}{S_0 - S_f} = (\frac{D}{D_0})^{\frac{1}{K}} \tag{77}$$

where:

S = Mean Tidal Steady-state Salinity;

S_f = Freshwater Salinity;

S_0 = Salinity at the Mouth (x=0);

D = Longitudinal Dispersion Coefficient;

D_0 = Longitudinal Dispersion Coefficient at the Mouth;

K = Van der Burgh Coefficient.

Discussions about the Limitations of the Analytical Methods

Typically, analytical studies have made too many assumptions and many of these assumptions are quite questionable; for example, Austin (2004) disregarded the time-varying fact of the salinity term in the equation, which might be a quite severe problem. The influence of tides cannot be neglected in studying problems related to mixing or salinity distribution in an estuary; in other words, because of the existence of tides, the salinity as well as many other properties cannot keep constant in such a complex system, thus the assumption that the salinity is independent on time is not acceptable.

In Shahap's equation, the freshwater input Q is a constant, neither varies with time nor varies with space, therefore, Shaha can state that the effective longitudinal dispersion appears to be positively correlated with river discharge at both high water slack and low water slack; however, it's hard to predict the river input in a real estuary, as the estuarine system is too

complex and there are numerous influencing factors such as the rainfall, the tide, and wind. Another drawback of this equation is that it's only applicable to high water slack or low water slack, as the salt equilibrium assumption is not likely to be possible during other stages

In Savenije's method, the data on salinity at a specified point or at the mouth is easy to obtain, the freshwater salinity is usually assumed to be zero, and *K* is usually determined by calibration. The difficulty is how to determine D_0, the longitudinal dispersion coefficient at the mouth of the freshwater-sea confluence.

Savenije (2012) proposed an empirical equation to calculate the D_0:

$$D_0 = 1400 N_{R,0}^{0.5} \frac{L_{e,0}}{L_{a^*}} u_0 h_0 \tag{78}$$

where:

$N_{R,0}$ = Estuarine Richardson number;

$L_{e,0}$ = The tidal excursion length;

L_{a^*} = The weighted value for the convergence length over the length

u_0 = The maximum tidal velocity;

h_0 = The water depth.

L_{a^*} is the weighted value for the convergence length L_a over the length of the salt intrusion L_s:

$$L_{a^*} = \frac{L_{a1} x_1 + L_{a2}(L_s - x_1)}{L_s} \tag{79}$$

where

L_{a1} = Convergence length seaward of x_1;

L_{a2} = Convergence length landward of x_1.

However, the applicability of this equation is quite limited. Take a prismatic-shaped estuary as an example, the convergence length can be regarded as infinite, then the value of D_0, the longitudinal dispersion coefficient would be zero, which is not practical in an estuary.

Besides, the Richardson number in an estuary is also very difficult to determine, many studies have been proposed, but none of them is universally accepted as effective enough. Therefore, it can only be determined using experimental methods such as the tracer experiment. Analytical models are not able to adequately capture some observed flow properties, especially in large-scale estuaries with realistic topography and complex climate conditions

A3.3 Downscaling Method

Representative Concentration Pathways

The projections of climate changes in the current study are based on the Representative Concentration Pathways (RCPs), the four greenhouse gas concentration trajectories, which is developed for the climate modeling community as a basis for modeling experiments. Radiative forcing, the difference of insolation absorbed by the Earth and energy radiated back to space, acts as an important index in climate change studies.

Table Appendix 3-1. Main characteristics of each RCP (Van Vuuren *et al.*, 2011)

Scenario component	RCP2.6	RCP4.5	RCP6	RCP8.5
Greenhouse gas emissions	Very low	Medium-low mitigation. Very low baseline	Medium baseline; high mitigation	High baseline
Agricultural area	Medium for cropland and pasture	Very low for both cropland and pasture	Medium for cropland but very low for pasture (total low)	Medium for both cropland and pasture
Air pollution	Medium-low	Medium	Medium	Medium-high

Four possible ranges of radiative forcing values (+2.6, +4.5, +6.0, and +8.5 W/m^2) in the year 2100 relative to pre-industrial values have been considered and their corresponding Representative Concentration Pathways are named as RCP2.6, RCP4.5, RCP6, RCP8.5. RCP8.2 assumes that global annual anthropogenic greenhouse gas emissions rise continuously

throughout the 21st century; while in RCP2.6, RCP4.5, RCP6.0, the emissions peak around 2010-2020, 2040, 2080 respectively, then decline. RCP2.6 is a mitigation scenario leading to a very low forcing level; RCP4.5 and PCP 6 are medium stabilization scenarios; RCP8.5 is a very high baseline emission scenario (Table Appendix 3-1; Van Vuuren *et al.*, 2011).

Table Appendix 3-2. Overview of representative concentration pathways (Van Vuuren *et al.*, 2011)

RCPs	Description
RCP2.6	Peak in radiative forcing at ~ 3 W/m^2 before 2100 and then decline.
RCP4.5	Stabilization without overshoot pathway to 4.5 W/m^2 at stabilization after 2100
RCP6	Stabilization without overshoot pathway to 6 W/m^2 after 2100
RCP8.5	Rising radiative forcing pathway leading to 8.5 W/m^2 by 2100

Table Appendix 3-2 shows an overview of representative concentration pathways by Van Vuuren *et al.* (2011). Table Appendix 3-3 shows the mid-21st century projections of global warming from the IPCC Fifth Assessment Report.

Table Appendix 3-3. Projections of Global Warming Increase (°C) for 2046-2065

Scenario	Mean and likely range
RCP2.6	1.0 (0.4 to 1.6)
RCP4.5	1.4 (0.9 to 2.0)
RCP6.0	1.3 (0.8 to 1.8)
RCP8.5	2.0 (1.4 to 2.6)

Van Vuuren *et al.* (2011) stated that emissions for most gases will be concentrated in specific areas in the future such as Eastern United States, Western Europe, Eastern China and Indian and emissions have a trend of being more concentrated in currently low-income regions (Figure A3-6).

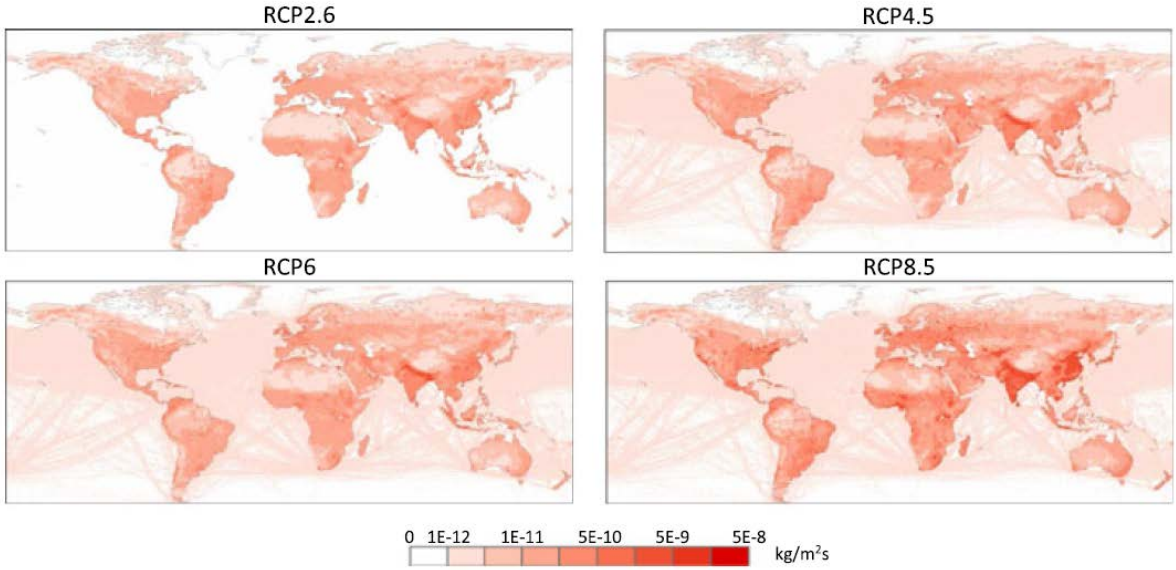

Figure A3-6. Emission pattern for 2100, for CH4 across the four RCPs (Van Vuuren et al., 2011)

ECP refers to extended concentration pathway, which is also useful for climate simulations. The RCPs have been extended to 2300 by Meinshausen *et al.* (2011), and Figure A3-7 shows the emissions of CO_2 and radiative forcing trajectories for extended concentration pathways.

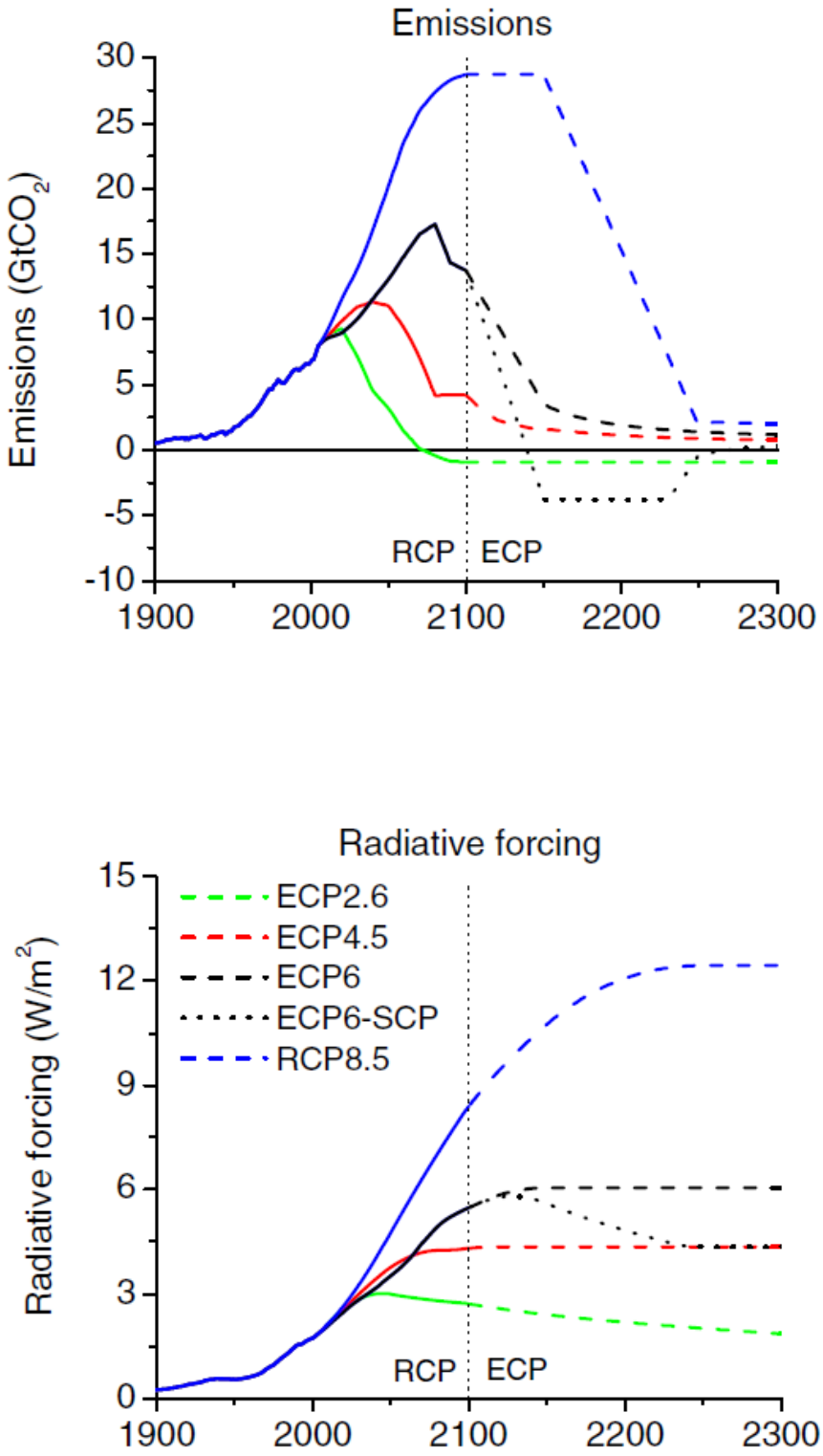

Figure A3-7. Extension of the RCPs. The ECP6-SCP shows an alternative extension for RCP6 (Meinshausen et al., 2011)

Downscaling Methods

Downscaling methods are used in this study to obtain local-scale climate projections from the outputs provided by Global Climate Models (GCMs), which are run at coarse spatial resolution. Downscaling is to take information known at large scales to predict information at local scales.

There are mainly two downscaling methods. One is dynamical and the other one is statistical. Dynamical downscaling is based on mapping high-resolution models on a regional sub-domain, with a boundary condition from observational data or obtained by lower-resolution model. Statistical downscaling is to develop statistical relationships between local-scale variables and large-scale predictors and use these relationships to predict local climate characteristics in the future from the output of global climate model (NCAR, 2015).

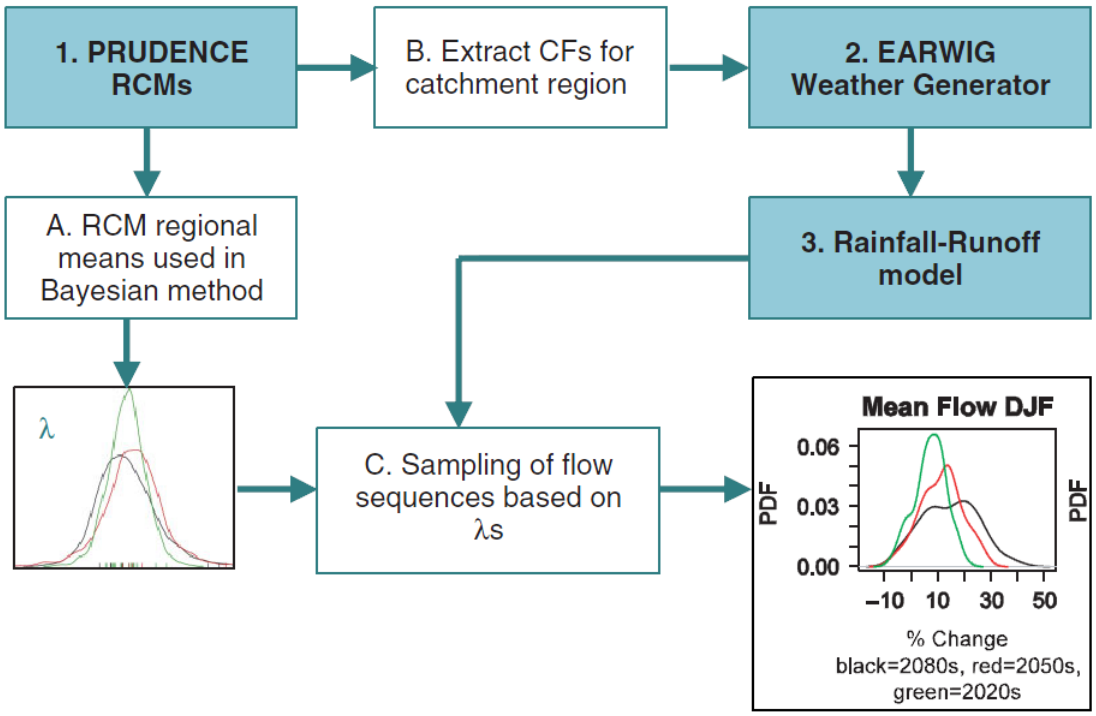

Figure A3-8. Flow diagram showing steps in the methodology used to produce probabilistic scenarios of climate change impacts for the River Eden (Fowler et al., 2007)

The statistical downscaling method is employed in the current thesis, for the following reasons: firstly, statistical downscaling techniques are much cheaper and more computationally

efficient; secondly, they can produce point-scale climatic variables; thirdly, they are based on standard and accepted statistical procedures; and finally they are able to integrate observational data into predictions.

Fowler *et al.* (2007) summarized some new developments associated with downscaling techniques. There are inherent uncertainties in the climate modeling process; therefore it can be advisable to incorporate uncertainties into climate predictions; namely, to take probabilistic treatments of projected climatic variables (Figure 3-8).

Pattern scaling technique is another new development; it is to standardise the climate change pattern for a variable derived from a global climate model over a geographic region, then the change pattern at any future time can be derived based on the assumption that the response signal patterns are almost independent of the forcing patterns and are approximately stationary in time.

A3.4 Coordinate Systems

The current study has considered three different types of coordinate systems: Cartesian coordinate system, Spherical Polar coordinate system, and sigma coordinate system. Finally, the Spherical Polar coordinate system is selected.

To begin with, most of the data collected for this study are in the form of (Latitude, Longitude, Value), like the bathymetry. If spherical polar coordinate system is not used, it will take a great deal of efforts to transform these data to match the coordinate system, and will introduce noticeable round-off errors. The Cartesian coordinate system, which is the most widely used coordinate system, is not natural for describing positions in a sphere.

Furthermore, the main advantage of sigma coordinate system is its treatment of the deeper layers, but the shallower layers have been of more interests in this study.

Additionally, the Coriolis Effect is significant for large-scale water bodies such as the Persian Gulf, and the Spherical Polar coordinate system are more advantageous in terms of incorporating the Coriolis term than other coordinate systems, as is more capable of precisely representing the Earth.

These three coordinate systems are described in the rest of this section.

Cartesian coordinates

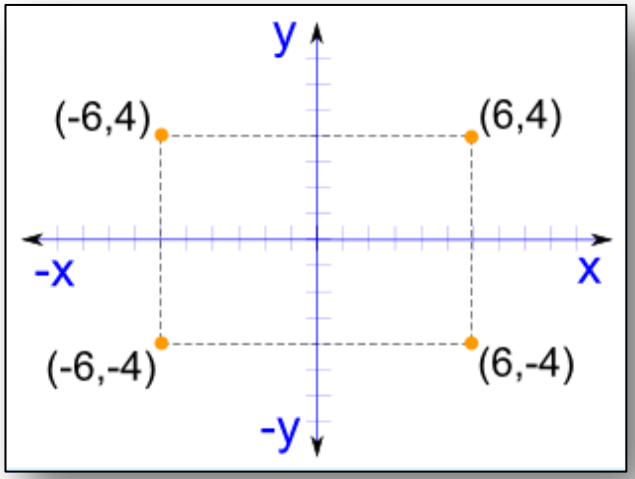

Figure 3-9. Two-dimensional Cartesian coordinate system (MIF, 2015)

Cartesian coordinate system can describe a point in any-dimensional space, but usually it can be used either as two-dimensional or three-dimensional coordinate system.

The two-dimensional Cartesian coordinate describes any point in a plane by two coordinates, which are the signed distances to two fixed perpendicular lines. The three-dimensional Cartesian coordinate (Figure A3-10; MIF, 2015) describes any point in a three-dimensional space by three coordinates, which are the signed distances to three mutually perpendicular planes.

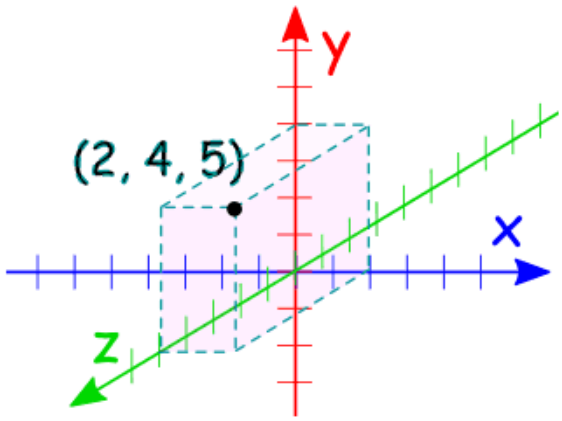

Figure A3-10. Three-dimensional Cartesian coordinate system (MIF, 2015)

In Cartesian coordinate, a point is typically expressed by parentheses, coordinates and commas. The coordinates are usually signified by the letters x and y in two-dimensional space, and *x, y, z* in three-dimensional space. In the field of hydraulics and oceanography, a point in a three-dimensional space can be expressed as:

$$(x, y, z)$$

where

x = Zonal direction;

y = Meridional direction;

z = vertical direction.

Spherical Coordinates

Spherical coordinate system, also known as the "spherical polar coordinate system", is typically used for three-dimensional space (Wolfram Mathworld, 2015).

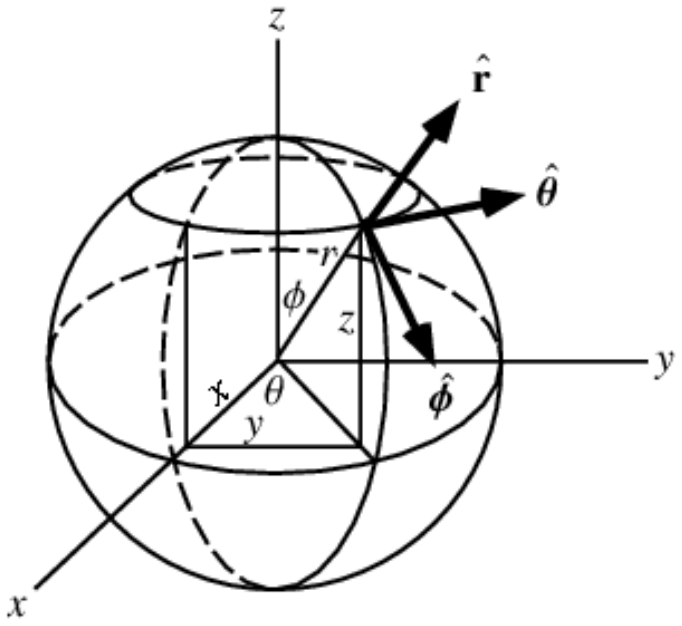

Figure A3-11. Spherical coordinate system (Wolfram Mathworld, 2015)

In spherical coordinates, any point can be described by the radial distance, the polar angle, and the azimuthal angle. The radial distance is the distance of the observed point from the origin of the coordinate system; the polar angle is the angle measured from the zenith direction; the azimuth angle is the angle of the orthogonal projection of that point on a reference plane that passes through the origin and is normal to the zenith, measured from an axis on the plane.

Spherical polar coordinate system is natural for describing positions on a sphere. Similar to Cartesian coordinate, a point in spherical polar coordinate system can be expressed by parentheses, the three parameters and commas:

$$(\gamma, \theta, \varphi)$$

Where

γ = the radial distance;

θ = azimuthal angle;

φ = polar angle.

If the object of study is the Earth, the azimuthal angle is called longitude, and the polar angle is called latitude.

In addition, the spherical polar coordinate system can also be used for describing two-dimensional space, where the sphere is taken as a unit sphere and the radius is unity.

Sigma coordinates

Sigma coordinate system (Figure A3-12; NWP, 2015) uses the independent variable sigma to denote a scaled pressure level, it describes the vertical position of a point according to pressure, that is this the ratio of the pressure difference between that point and the top of the domain to that of the pressure difference between a fundamental base below the point and the top of the domain.

The sigma coordinate system is a topographically conformal vertical coordinate system since it is pressure based and normalized. It is natural for describing continuous fields where terrain varies widely but smoothly and it will assign increasing vertical resolution near the ground. This coordinate system is widely used for fields associated with fluid dynamics such as

oceanography, atmosphere and meteorology, since it enables the governing equations of fluid dynamics to be written in a relatively simple form. In oceanic models with sigma coordinates, the number of vertical levels in the water column is the same everywhere in the domain irrespective of the depth of the water column.

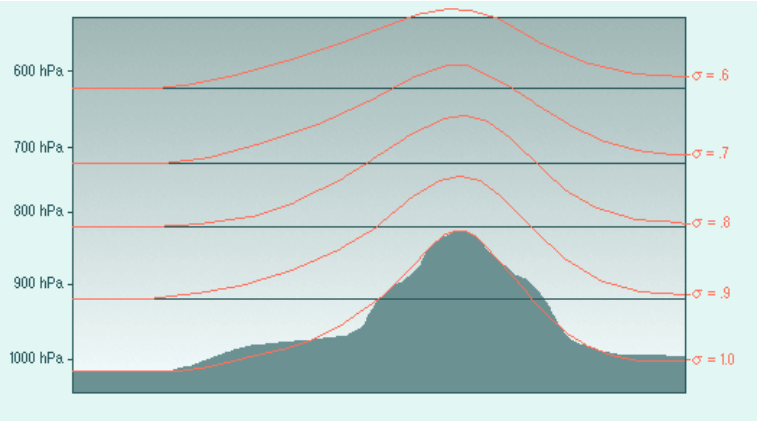

Figure A3-12. An example of sigma coordinate model (NWP, 2015)

Additionally, there are also some hybrid sigma-pressure models that are widely used in the field of meteorology and oceanography. Hybrid sigma-pressure coordinate system combines sigma-denominated layers at the bottom and pressure-denominated layers aloft.

Appendix 4 Some MATLAB Codes for Configuring the Model and Preparing the Data

A4.1 Bathymetry Data

This MATLAB script prepares the bathymetry data. It filters out unnecessary points, reshapes the dataset, plots the bathymetry and writes the data into the binary format.

```
% Select the xyz data that are needed
% n_Meridional = the number of grids in Meridional direction.
% base = the index for the first needed Zonal value for each Meridional value.
% i= the index for all the needed values
initial_selected_xyz=zeros(28000,3);
for n_Meridional=1:140;
   base=3+7212*(n_Meridional-1);
```

```
    for n_Zonal=1:200;
        i=base+6*(n_Zonal-1);
        initial_selected_xyz(((n_Meridional-1)*200+n_Zonal),:)=xyzpersiangulf(i,:);
    end
end
 % The needed points are selected)

% write the initial selected xyz data to excel
xlswrite('a05_initial_selected_xyz.xlsx',initial_selected_xyz);

% remove xy data
initial_selected_z=initial_selected_xyz(:,3);
% Only Z values are retained

% reshape z data and write to excel
z_reshape=reshape(initial_selected_z,[200 140]);
xlswrite('a06_z_reshape.xlsx', z_reshape);
% Z values are reshaped  to match the Coordinate system)

%get the final bathymetry and set the values for land as zero
z_reshape(z_reshape>0)=0;
bathymetry=z_reshape;
% Land is set to be zero

%write the final bathymetry to excel
xlswrite('a07_bathymetry.xlsx',bathymetry);

%write the final bathymetry to binary
fid=fopen('bathymetry.bin','w','b');
fwrite(fid,bathymetry,'real*4');
fclose(fid);

%Plot the bathymetry
%Set the colorbar, title, labels and ticks
imagesc(bathymetry');
axis xy;
colorbar;
caxis([-100 0]);
```

```
title('Bathymetry of Persian Gulf');
xlabel('Zonal (°E)');
ylabel('Meridional (°N)');
set(gca,'XTick',15:20:195);
set(gca,'YTick',12:20:132);
set(gca,'XTickLabel',{'48','49','50','51','52','53','54','55','56','57'});
set(gca,'YTickLabel',{'24','25','26','27','28','29','30'});

%Save the Figure as .jpg Figure
saveas(gcf,'bathymetry.jpg')
```

A4.2 Wind Data

This MATLAB script prepares the wind data. It calculates the wind stress from the wind speed, and writes the results into the binary format.

```
windspeed=data;
% Calculate Cd
for i=1:672;
   cd(i)=(0.29+3.1/windspeed(i)+7.7/(windspeed(i)^2))/1000;
end

%Calculate tau
for i=1:672;
   tau(i)=1.3*cd(i)*(windspeed(i))^2;
end

%calculate taux tauy
taux=zeros(200,140,648);
tauy=zeros(200,140,648);
for i=1:200;
   for j=1:140;
      for k=1:672;
            taux(i,j,k)=tau(k)*cos(pi/4);
        tauy(i,j,k)=tau(k)*cos(pi/4);
      end
   end
```

```
end

%write taux to excel
for k=1:15;
   xlswrite('a06_taux.xlsx',taux(:,:,k),k);
end

%write tauy to excel
for k=1:15;
   xlswrite('a07_tauy.xlsx',tauy(:,:,k),k);
end

%write taux to binary
fid=fopen('a08_trenberth_taux.bin','w','b');
fwrite(fid,taux,'real*4');
fclose(fid);

%write tauy to binary
fid=fopen('a09_trenberth_tauy.bin','w','b');
fwrite(fid,tauy,'real*4');
fclose(fid);
```

A4.3 Vertical Configuration

This MATLAB script sets the vertical configuration of the study domain. The study domain is divided into ten layers, and this script calculates the thickness of each layer.

```
% Read the bathymetry data
fid=fopen('bathymetry.bin','r','b');
bathymetry=fread(fid,inf,'single');
bathymetry=reshape(bathymetry,[200 140]);
fclose(fid);

% Find out the maximu depth
hmax=-100;
for i=1:200;
   for j=1:140;
      if bathymetry(i,j)<hmax;
```

```
            hmax=bathymetry(i,j);
        end;
    end;
end;

%Calculate the ratio
syms q;
q=solve(10*(1-q^10)/(1-q)==abs(hmax));
ratio_raw=q(1);
ratio_raw=double(ratio_raw);
ratio=str2num(sprintf('%.2f',ratio_raw));

% Calculate the layer thickness for each layer
thickness=zeros(10,1);
for i=1:10;
    thickness(i)=10*ratio^(i-1);
end;
```

A4.4 Water Mask

This MATLAB script determines the water masks for the study domain. When the water mask is zero, the cell represents land, otherwise the cell denotes water.

```
% Generate maskl
maskl=zeros(200,140,10);
maskl(:,:,1)=bathymetry;
for n=2:10;
    maskl(:,:,n)=maskl(:,:,n-1)+thickness(n-1);
end
   maskl(maskl>0)=0;
%write to excel
for n=1:10
    xlswrite('maskl.xlsx',maskl(:,:,n),n);
end
%write to binary
fid=fopen('maskl.bin','w','b');
fwrite(fid,maskl,'real*4');
fclose(fid);
```